IntechOpen

New Advances in Steel Engineering

Edited by Adriana da Cunha Rocha

New Advances in Steel Engineering

Edited by Adriana da Cunha Rocha

Published in London, United Kingdom

New Advances in Steel Engineering
http://dx.doi.org/10.5772/intechopen.110914
Edited by Adriana da Cunha Rocha

Contributors
Adriana da Cunha Rocha, Ana P. Loperena, Ivana L. Lehr, Janusz Dobrzański, Joanna Furmanek, Lorena I. Brugnoni, M. Vijay Kumar, María Belén González, Nadia C. Cortes, Nidhi Nischal, Pavel Martauz, Pedro Enrique Monforte Brandão Marques, Vojtěch Václavík

First published in London, United Kingdom, 2024 by IntechOpen
IntechOpen is the global imprint of INTECHOPEN LIMITED, registered in England and Wales, registration number: 11086078, 167-169 Great Portland Street, London, W1W 5PF, United Kingdom

British Library Cataloguing-in-Publication Data
A catalogue record for this book is available from the British Library

Additional hard and PDF copies can be obtained from orders@intechopen.com

New Advances in Steel Engineering
Edited by Adriana da Cunha Rocha
p. cm.
Print ISBN 978-1-83769-832-5
Online ISBN 978-1-83769-831-8
eBook (PDF) ISBN 978-1-83769-833-2

Meet the editor

Professor Adriana da Cunha Rocha graduated from the Pontifical Catholic University of Rio de Janeiro, Brazil (PUC-Rio) with master's and doctorate degrees in Material Sciences and Metallurgical Engineering. She has a postdoc fellowship at Lawrence Berkeley National Laboratory, California, USA. Currently, she is a professor in the Department of Metallurgical Engineering and Materials, at the Federal University of Rio de Janeiro (UFRJ), Brazil, and Director of the Academic and Extension Division of the Polytechnic School of UFRJ. Her main research areas are high-temperature degradation and corrosion of materials, multi-component high-entropy alloys, crystallography, X-ray diffraction, and steel engineering. Dr. da Cunha Rocha holds two registered patents.

Contents

Preface

The development of steel can be traced back thousands of years to ancient civilizations, but it was not until the 19th century that significant advancements were made in its production. The invention of the Bessemer process in the 1850s revolutionized steelmaking by allowing for the mass production of high-quality steel at a lower cost.

Steel quickly became a crucial material for industrialization, enabling advancements in building construction, transportation, and manufacturing. The development of steel also played a key role in the construction of railways, bridges, and skyscrapers, transforming cities and shaping modern infrastructure.

Throughout the 20th century, further innovations in steelmaking processes, such as the basic oxygen furnace and electric arc furnace, continued to improve the quality and efficiency of steel production. Today, steel remains one of the most widely used materials in the world, with applications in a wide range of industries, from automotive and aerospace to construction and infrastructure.

The development of new types of steel, such as stainless steel and high-strength steel, have also expanded its uses and capabilities, making it an indispensable material in modern society. With ongoing advancements in technology and materials science, the future of steel continues to evolve, with the potential for even more efficient and sustainable production methods.

Steel is also recyclable and sustainable, making it an environmentally friendly material option. Steel recycling is the process of recovering and reusing steel materials from products or structures that are no longer in use. The steel recycling process involves collecting, sorting, processing, and melting down steel scrap to create new steel products. Recycling steel helps to conserve natural resources, reduce energy consumption, and lower greenhouse gas emissions compared to producing steel from raw materials. Additionally, steel recycling helps to reduce waste and lessen the environmental impact of mining and manufacturing steel.

Steel engineers use their expertise in materials science, structural analysis, and construction techniques to ensure that steel structures are safe, cost-effective, and able to withstand the forces and environmental conditions they will be exposed to. They may work on projects ranging from small residential buildings to large industrial complexes, and may collaborate with architects, contractors, and other professionals to ensure that steel structures meet all design specifications and regulatory requirements.

In recent years, advancements in technology and production processes have led to the development of high-strength steel alloys that offer even greater performance and design possibilities. Overall, steel continues to be a crucial material in modern society's infrastructure and development.

This book presents some works that show some advances in steel engineering nowadays. From those insights, we hope that steel engineers, and any enthusiastic reader, can relate and use some of those new techniques to promote the evolution of such a versatile material.

Adriana da Cunha Rocha
Department of Metallurgical and Materials Engineering,
Federal University of Rio de Janeiro (UFRJ),
Rio de Janeiro, R.J., Brasil

Chapter 1

Introductory Chapter: Advances in Steel Engineering

Adriana da Cunha Rocha

1. Introduction: the history of the steel

Steel fabrication has a long and rich history dating back thousands of years. The process of creating steel through the fusion of iron and carbon has been known since ancient times, with examples of early steel artifacts found in ancient Egypt and Mesopotamia. However, it was not until the nineteenth century that steel fabrication began to develop as a modern industrial process [1–4].

One significant development in the history of steel fabrication was the invention of the Bessemer process in the 1850s by Sir Henry Bessemer [5]. This process allowed for the mass production of steel by blowing air through molten iron to remove impurities and oxidize the carbon content. This led to a significant reduction in the cost of steel production, making it more accessible for various applications.

With the availability of mass-produced steel, the demand for fabricated steel increased significantly. Steel fabrication became a crucial industry in the construction sector, allowing for the fabrication of structural components such as beams, columns, and trusses. The use of steel in construction provided greater strength and durability compared to traditional materials like wood or stone.

In the twentieth century, advancements in technology and industrialization further revolutionized steel fabrication. The introduction of electric arc furnaces in the late nineteenth century allowed for more efficient steel production, while developments in welding techniques made it easier and faster to join pieces of steel together [6].

During World War II, steel fabrication played a vital role in the manufacturing of tanks, ships, and airplanes for military purposes. The mass production of steel and advancements in fabrication techniques helped meet the increased demand for these war materials [2, 6].

In recent decades, steel fabrication has continued to evolve with advancements in automation, robotics, computer-aided design technologies, and, more recently, artificial intelligence (AI). These advancements have improved precision, efficiency, and safety in the fabrication process, allowing for more complex and intricate steel structures to be created.

Today, steel fabrication is essential in various industries, including construction, infrastructure, automotive, and aerospace. It involves the cutting, shaping, and assembling of steel components to create structural elements, machinery, and equipment. The fabrication process typically involves a series of steps, including design, cutting, bending, welding, and finishing.

Overall, the history of steel fabrication showcases the continuous development of manufacturing techniques and technologies, leading to significant advancements in

the construction and manufacturing industries. Steel fabrication has played a crucial role in shaping modern infrastructure and continues to be a vital industry for various applications.

2. Impact of steel in modern society

Steel has had a significant impact on modern society in several ways. This material is widely used in the construction of buildings, bridges, roads, and other infrastructure. Its high strength-to-weight ratio and durability make it an essential material in the construction industry. Steel is crucial in the manufacturing of automobiles, ships, trains, and airplanes. It provides a strong and lightweight material for the body, chassis, and engine components, contributing to fuel efficiency and overall safety. Additionally, steel railways and bridges facilitate the transportation of goods and people, connecting distant regions and supporting economic growth.

Steel is also an integral and crucial part of our daily lives, found in various household appliances, tools, and consumer goods. Items like refrigerators, washing machines, bicycles, cutlery, and furniture often use steel components for their strength and longevity.

Although there have been many concerns on the use of steel, it must be considered that steel is a highly recyclable material, contributing to the circular economy and reducing environmental impact. Recycled steel can be used to produce new steel products, reducing the need for raw materials and energy-intensive processes. Additionally, steel's durability and strength contribute to the longevity of structures, minimizing the need for frequent replacements and reducing waste.

Overall, the impact of steel in modern society is profound, as it supports economic growth, facilitates transportation and infrastructure development, enables technological advancements, and contributes to sustainability efforts.

3. Steel engineering

Steel engineering has a vast definition because it encompasses all the applications in which this material can be used. It can comprise a variety of research areas such as the optimization of mineral processing, better practices for the use of steel, microstructure steel design to achieve ultimate properties, and so on.

Undoubtedly, steel is one of the most versatile materials in the world, and it is continuously evolving. The evolution of steel has been observed for the rising of new steel alloys over the decades. Science and industry have been working closely together to provide materials with better performances and for all sorts of new applications as well. One can only expect great developments in steel engineering for the years to come.

DOI: http://dx.doi.org/10.5772/intechopen.1004331

Author details

Adriana da Cunha Rocha
Federal University of Rio de Janeiro (UFRJ), Rio de Janeiro, RJ, Brazil

*Address all correspondence to: adrirocha@metalmat.ufrj.br

IntechOpen

References

[1] Bugayev K, Konovalov Y, Bychkov Y, Tretyakov E, Savin IV. Iron and Steel Production. New York, USA: The Minerva Group, Inc.; 2001. ISBN: 978-0-89499-109-7

[2] Ponting C. World History: A New Perspective. London: Chatto & Windus; 2000. ISBN: 0-7126-6572-2

[3] Barraclough KC. Steel before Bessemer: I Blister Steel: The Birth of an Industry. London: The Metals Society; 1984

[4] Needham J. Science and civilisation in China, Volume 5, Part 7. first ed. Cambridge, UK: Cambridge University Press; 2008. pp. 261-265. ISBN: 9780521875660

[5] Bessemer process. The Editors of Encyclopaedia Britannica. In: Gregersen E, editor. Britannica. Vol. 2. London: Encyclopædia Britannica Inc.; 2005. p. 168

[6] Gordon RB. American Iron, 1607-1900. Maryland, USA: JHU Press; 2001. p. 221. ISBN: 978-0-8018-6816-0

Chapter 2

The Use of Machine Learning to Predict Steel Properties – A Review on the Latest Works

Adriana da Cunha Rocha
and Pedro Enrique Monforte Brandão Marques

Abstract

Artificial Intelligence [AI] has been of great discussion lately and one can perceive its use in many aspects of modern life. In science, and more specifically in Materials Sciences, AI has been employed for many different applications. Machine Learning (ML) has been historically linked to Artificial Intelligence (AI) for many decades. Some basic concepts of ML can be traced from the 1930s, but it was only during the 1980s and 1990s that ML really started to be used in a stronger and well-organized fashion, due to the development of more efficient algorithms from better and more robust data processing machines. This chapter presents a review on the recent works of distinct research groups that have been using Machine Learning [ML], which is one of many different methods of AI, as a tool for predicting steel properties. A brief definition of ML is given at the beginning of the chapter, followed by some of the most relevant examples of ML use to exemplify the power of this AI method for the development of steel engineering.

Keywords: steels, machine learning, artificial intelligence, steel properties, steel engineering

1. Introduction

Machine Learning (ML) has been historically linked to Artificial Intelligence (AI) for many decades. Some basic concepts of ML can be traced from the 1930s, but it was only during the 1980s and 1990s that ML really started to be used in a stronger and well-organized fashion, due to the development of more efficient algorithms from better and more robust data processing machines. In 1995, Cortes and Vapnik [1], from Bell Laboratories, introduced the concept of ML in their work and from that point on, the development of ML has been enormous.

Another significant contribution was the development of *Artificial Neural Networks* (ANNs), which are models inspired by the functioning of the human brain. These networks, made up of multiple layers of artificial neurons, were able to learn

from large amounts of data and perform complex tasks, such as pattern recognition and image processing. With the advancement of the internet and the emergence of large data storage platforms, the field of Machine Learning has begun to use larger and larger datasets to train its models.

The advent of Machine Learning [ML] [2] has ushered in a transformative era in the industrial landscape, redefining the approach to complex technological challenges and to process optimization. With its foundation in advanced data analytics and computational algorithms, ML has become the linchpin of innovation across various sectors. In the realm of industrial research and development, ML catalyzes a paradigm shift in how industries innovate. At the intersection of advanced data analytics and computational intelligence, ML emerged as an indispensable tool, offering unprecedented capabilities to enhance decision-making, fostering a sustainable and adaptive approach to the evolving landscape of industrial research.

The integration of ML in the domain of steel studies marks a transformative leap in the ability to predict and tailor the properties of steels with unprecedented precision. By harnessing the power of advanced computational algorithms, researchers and industry professionals can delve into vast datasets, extracting intricate patterns that govern the relationships between steel compositions, processing parameters, and alloys' properties. Therefore, ML can play a powerful role in steel-related studies by enabling advanced data analysis and pattern recognition, opening avenues for predictive modeling, enabling the anticipation of key characteristics, thereby revolutionizing the design, production, and quality control processes in the steel industry [3].

For instance, these algorithms can analyze intricate relationships between input variables and production outcomes, therefore contributing to process optimization. This aids in optimizing manufacturing processes by fine-tuning parameters like temperature, pressure, and steel compositions. Through iterative learning, ML models can adapt to evolving conditions, contributing to enhanced efficiency and resource utilization. In quality control, ML-based systems are adept at detecting anomalies and defects in steel products. Image recognition algorithms, for instance, can scrutinize visual data from production lines, identifying imperfections or irregularities in real-time. This proactive approach reduces waste and ensures the production of high-quality steel. On the other hand, ML can aid in optimizing the steel supply chain by predicting demand fluctuations, identifying potential bottlenecks, and improving inventory management. This ensures a streamlined and responsive supply chain, minimizing delays and optimizing resource allocation [2, 3].

This chapter will be focused on an important application of ML in steel production: Properties Prediction. In other words, it will be explored how ML serves as a dynamic and indispensable tool for forecasting and optimizing the properties of steels for diverse applications. The basics of ML will be introduced and then, examples on how to use ML for cases of material properties will be presented.

2. The basics of machine learning

What exactly is machine learning from its inception? While its definitions may vary slightly across different fields, it can be broadly described as *"the field revolving around the creation of algorithms and computational models, enabling systems to learn patterns and make predictions or decisions without direct programming."* This entails the iterative training of models on data, enabling them to identify intricate patterns, correlations, and interdependencies [3].

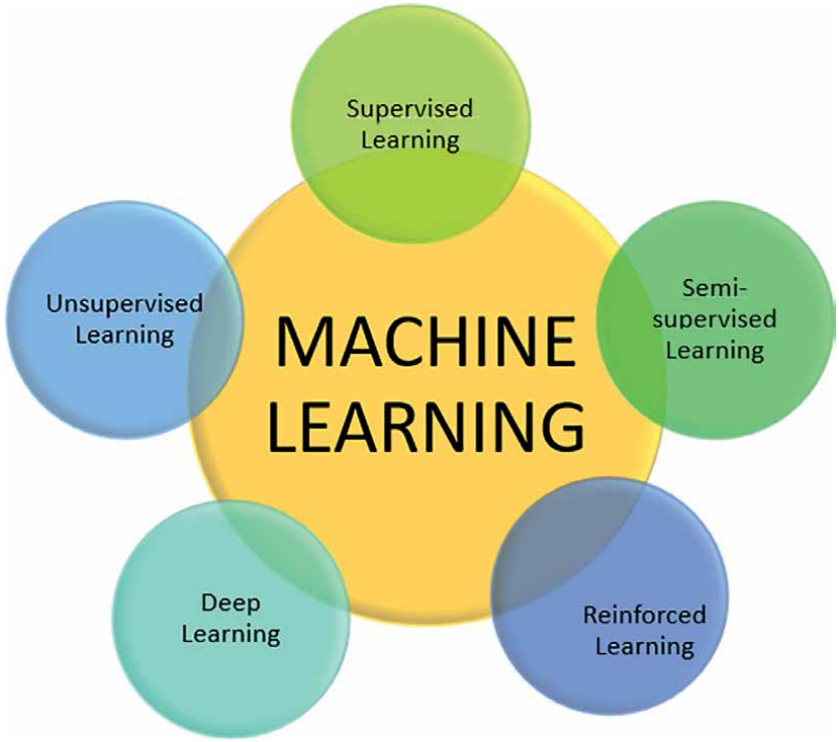

Figure 1.
Classification of machine learning methods.

Machine Learning can be classified according to the kind of learning the system is subjected to, varying from supervised to unsupervised learning, as shown in **Figure 1** [2, 4, 5].

2.1 Supervised learning

Supervised learning [5] is one of the main categories in machine learning. It involves creating models by using labeled data, also known as instances or examples, in order to learn how to make predictions or decisions. In simpler terms, the model is exposed to a set of input and output examples, where the desired output is provided or labeled for each example. Using these labeled examples, the model learns how to map new inputs to the desired outputs.

This type of algorithm is capable of creating predictive models that estimate a specific property of elements in a set, typically referred to as a target, based on a group of known parameters known as features. To define this model, a process called "training" or "fitting" is necessary. During this process, the algorithm is shown a training set consisting of a large number of examples where the properties of interest are already known. For instance, it is possible to train a model to predict the hardness gain of steels in a certain thermos-mechanical treatment by using a database containing the fractions of alloying elements and instrumental treatment parameters from a wide range of steel compositions. When the target property is a discrete random variable, the model is known as a "classification" model.

Conversely, if the target is a continuous random variable, the model is referred to as a "regression" model.

2.2 Unsupervised learning

When working with data that do not have labels, a different algorithm is required. This particular category of models is known as Unsupervised Learning [6], where the algorithm is trained using unlabeled data. The system then attempts to learn patterns, structures, or relationships within the data without any direct guidance or predefined output labels. The objective is to uncover the inherent structure or distribution of the data and uncover hidden patterns or groups. In unsupervised learning, the training dataset only contains input features, with no corresponding output labels to guide the learning process. This includes tasks, such as grouping similar data points together, reducing the complexity of high-dimensional datasets, estimating probability distributions to identify anomalies, discovering association rules, and segmenting data into meaningful groups without any prior knowledge of class labels.

2.3 Semi-supervised learning

Semi-supervised learning [5, 6] is the term used to describe the combination of labeled and unlabeled instances in the training of a learning algorithm. This approach is a middle ground between fully supervised and unsupervised learning models. By utilizing both labeled and unlabeled data, the model can benefit from the guidance provided by the labeled instances while also taking advantage of the larger pool of unlabeled data to improve its ability to generalize. This integration of labeled and unlabeled information is particularly useful in situations where obtaining labeled data is difficult or costly, allowing the model to be applied to real-world scenarios where data scarcity is a challenge. Semi-supervised learning has proven to be valuable in various domains, such as image recognition, natural language processing, and medical diagnostics, where labeled data may be limited, expensive to acquire, or require expert annotation. This makes it ideal for applications where the model's performance can be enhanced by effectively combining labeled and unlabeled instances.

2.4 Deep learning and reinforced learning

The final two machine learning models, considered to be the most intricate ones, are called Deep Learning [7, 8] and Reinforced Learning [9, 10]. Deep Learning utilizes neural networks that have multiple layers to automatically extract hierarchical representations from data, allowing for the modeling of intricate patterns and features. It has demonstrated exceptional performance in demanding tasks, such as recognizing images and speech, processing natural language, and analyzing sequential data. On the other hand, Reinforcement Learning is a framework in which an agent learns to make decisions by interacting with an environment and receiving feedback in the form of rewards or punishments. This approach is particularly suitable for problems that involve making decisions in a sequence, controlling systems, and optimizing tasks. Deep learning excels in tasks that involve vast amounts of data and complex relationships, while reinforcement learning is well suited for scenarios where an agent must learn optimal strategies through trial-and-error interactions, making it applicable in various fields such as robotics, game playing, and autonomous systems.

3. Determination of steel properties by machine learning

Steel properties (such as physical, chemical, electrical, mechanical, and so on) are mainly acquired in a range of different tests and experiments, by the collection of empirical numerical data, later to be processed and analyzed accordingly [11]. Machine Learning offers, besides other features, an important contribution in terms of data prediction and data analysis never seen before, because it anticipates features that could not be achieved simply by conventional testing. The tremendous computational capability of ML allows the optimization of more intricate steels properties analysis. This section presents a few works that have been developed in the past years, where the use of ML has proven to be an important feature for the determination of some of those steel properties. These examples present cases where distinct types of ML techniques have been used successfully.

3.1 ML on the determination of mechanical properties of steels

Nowadays, many different studies can be found in the literature related to the prediction and determination of mechanical properties of steels. Some of those works are brought here for exemplification of how strong this computational tool can be for the development of steel engineering. Three different studies are presented, depicting how ML became a powerful predictive asset for steel property prediction.

3.1.1 Enhancing manganese (Mn) medium steel's mechanical properties

Lee et al. [12] created a model dataset of 1075 values acquired from literature related to the tensile properties of manganese medium steels, aiming at the development of a new Mn medium steel with superior high strength. With the analysis of the datasets, authors could create a boosted decision tree regression [BD] model to predict ultimate tensile strength [UTS] and total elongation [TE] of medium-Mn steels. The trained BD models predicted that the Mn medium steel would have high UTS of 1957 MPa and TE of 10.7%, when austenitized at 780°C for 4 min and air-cooled. The predicted UTS and TE matched well with experimentally measured values of UTS of 1952 MPa and TE of 9.9%, indicating the efficacy of the BD models. The steel designed by the BD model exhibited high UTS [1952 MPa] experimentally, which was approximately 100 MPa higher than that of medium-Mn steel.

3.1.2 Steel microstructure modeling

Wang and Adachi [13] developed in their study an important tool based on Machine Learning algorithms, to predict microstructure models where direct analysis of property predictions and properties-to-microstructure inverse analysis was conducted. From those data, they aim to reach steel properties, such as stress–strain curves, tensile strength, and total elongation.

3.1.3 Thermo-mechanically controlled process (TMCP) for steels

Lee et al. [14] used ML to predict how thermo-mechanically controlled process [TMCP] would change some mechanical properties of steel alloys. In their study, the

authors gathered 16 attributes related to the compositional and processing information and the corresponding yield strength and ultimate tensile strength values for 5473 thermo-mechanically controlled processed [TMCP] steel alloys. From those data, they designed an ML platform that was able to predict those properties from the chosen attributes.

3.2 ML on the determination of corrosion properties of steels

It is well known that steel degradation and corrosion can generate huge economical and production losses in many industries worldwide. It can also cause catastrophic impacts not only on metallic components and equipment, but also on people's lives. Therefore, corrosion prevention is mandatory for many processes.

Machine Learning has been a tool for corrosion prevention in many studies. The work of Coelho and colleagues [15] is cited here for its interesting approach. They investigated the pitting corrosion on a 316L steel, which is one of the most utilized steels in the world, due to its good mechanical and corrosion properties. The 316L steel low carbon and high chromium contents enables this material to resist many different types of temperatures and environmental degradation. Their goal was to estimate pitting descriptors for their target steel using scanning electrochemical cell microscopy (SECCM). The methodology mainly consisted of building a hybrid rule-based machine learning approach, via linear regression and artificial neural networks. They were able to observe a trend of passive range shortening with increasing testing aggressiveness due to the delayed stabilization of the passive film, rather than early passivity breakdown.

Aghaaminiha et al. [16] studied how to measure corrosion rates of carbon steel as a function of time when corrosion inhibitors are used in different dosages and dose schedules. Supervised ML was employed and came up with the Random Forest prediction algorithm, among others, because that algorithm displayed the lower mean squared error ranging from 0.005 to 0.093, which are good values for prediction, demonstrating that the entire time trend of the corrosion rate of mild steel was quite well predicted by the trained RF model.

3.3 ML on the determination of microstructural properties of steels

The material microstructure is surely the basic feature of any material from where every property is determined. The specific steel microstructure provides important information on how that steel might behave depending on the external characteristics it might be subject to. Therefore, being able to understand and predict material microstructure is fundamental for steel engineering. Today, one can find many studies on that subject and more and more scientists are employing ML to aid their understanding of steel microstructure.

Kim et al. [17] proposed an ML method using unsupervised deep learning to estimate phase volume fraction of multiphase steel. Their results presented a mean relative error between 0.73% and 4.53%, suggesting that the estimated phase fraction values are very close to the true phase fraction of the multiphase steel.

Kusampudi and Diehl [18] developed an ML model that was able to generate dual-phase steel microstructures, based on the steel phases and crystallographic orientation aiming to build steels with desired properties. Their method consisted of training a variational autoencoder to identify the attributes from a synthetic dual-phase

microstructure, with Bayesian optimization. A Rain Forest ML was also employed to predict the microstructure-properties relationship.

3.4 ML on the determination of welding process properties

In the realm of welding research, the utilization of machine learning entails the strategic implementation of computational algorithms as a means of analyzing and optimizing various aspects of the welding process. Machine learning techniques offer the potential to forecast the quality of welds, refine welding parameters to an optimal level, and promptly identify potential flaws or irregularities as they occur.

Through the assimilation of data acquired from sensors, images, and other sources during the welding procedure, machine learning models can acquire an understanding of intricate patterns and correlations, thereby assisting in the construction of predictive models pertaining to weld strength, integrity, and overall quality. Furthermore, the incorporation of machine learning has the capacity to contribute to automated decision-making in welding, such as making real-time adjustments to parameters based on feedback, thereby bolstering efficiency and minimizing the necessity for manual intervention. The integration of machine learning within the domain of welding research holds great promise in advancing the precision, dependability, and productivity of welding processes across a wide array of applications and industries [19].

Tran et al. [20] developed an artificial intelligence-based system to predict several relationships between welding process parameters and weld bead geometries for shielded metal arc welding (SMAW), metal inert gas (MIG), and tungsten inert gas (TIG) processes. The system was built of both a regression model and the deep learning model, establishing a commendable correlation between the welding process parameters and the weld bead geometry. These research findings lay a foundation for constructing predictive systems or refining welding process parameters.

Abd Halim et al. [21] created an application tool called Q-check that utilizes an open-source and customized algorithm based on artificial neural networks to predict parameters such as welding time, current, and electrode force, in relation to tensile shear load-bearing capacity [TSLBC] and weld quality classifications [WQC]. For this purpose, a supervised learning algorithm was implemented, encompassing the standard backpropagation neural network gradient descent [GD], stochastic gradient descent [SGD], and Levenberg-Marquardt [LM] methods, based on an 80% training and 20% test set. The results showed that, for predicting TSLBC, it has achieved an 87.220% accuracy rate for GD, 92.865% for SGD, and 93.670% for LM algorithms. On the other hand, for the prediction of WQC, the accuracy rates were observed to be 62.5% for GD and 75% for both SGD and LM algorithms.

Wang et al. [22] present the design of an intelligent expert system for gas metal arc welding (GMAW) process, with the aim of allowing the user to input the initial welding information, and subsequently display suitable welding procedure parameter schemes through an output interface. The user can then select the most appropriate scheme based on the specific requirements or generate a welding procedure specification in line with the enterprise format for immediate utilization. To do this, the system incorporates database technology and the utilization of the XGBoost machine learning algorithm to further enhance its capabilities. XGBoost is short for eXtreme Gradient Boosting algorithm, which is, in practice, a binary tree based on Gradient Boosting, a supervisioned regression algorithm. By training the model on a dataset,

the system can predict the welding raw data and continuously optimize the model by accumulating more data for daily use.

4. Conclusions

This chapter presented an overview on how Machine Learning can be used to predict various steel properties. It could be seen that Machine learning models can analyze various factors, such as chemical composition, heat treatment parameters, and processing conditions, to predict the strength properties of steel, such as yield strength, ultimate tensile strength, and hardness. Machine learning algorithms can also be trained on datasets that contain information about steel composition, environmental conditions, and past instances of corrosion to develop models that can predict the corrosion resistance of different steel grades. Some steel processing features, such as weldability, can also benefit from this technique.

In general, it can be noted that for any type of ML (Supervised, Unsupervised, Semi-Supervised Deep, and Reinforced Learning), the size of the input dataset is crucial for the efficiency of the models to be used in the learning. Datasets with a great amount of data, either from literature or from testing, seem to be fundamental for creating efficient decision trees for more accurate predictions of specific features on materials. That can also aid inverse analysis learning algorithms and promote optimal attribute associations.

By leveraging machine learning techniques, engineers and material scientists can efficiently analyze complex datasets to predict and optimize steel properties for various applications, leading to better material selection and improved performance in real-world scenarios. However, it is important to address the potential challenges and ethical considerations associated with machine learning. It is essential to ensure that the deployment of machine learning technologies aligns with societal values and benefits all individuals.

Author details

Adriana da Cunha Rocha* and Pedro Enrique Monforte Brandão Marques
Federal University of Rio de Janeiro (UFRJ), Rio de Janeiro, RJ, Brasil

*Address all correspondence to: adrirocha@metalmat.ufrj.br

IntechOpen

References

[1] Cortes C, Vapnik V. Support-vector networks (PDF). Machine Learning. 1995;**20**(3):273-297

[2] Kelleher JD, Namee M, D'Arcy A. Fundamentals of Machine Learning for Predictive Data Analytics. Cambridge, MA, USA: The MIT Press; 2015

[3] Cheng Y, Wang T, Zhang G, editors. Artificial Intelligence for Materials Science., Springer Series in Materials Science. USA: Springer International Publishing; 2021

[4] James G, Witten D, Hastie T, Tibshirani R. An introduction to statistical learning. In: Springer Texts in Statistics. US: Springer; 2021

[5] Cerulli G. Fundamentals of Supervised Machine Learning – With Applications in Python, R, and Stata. Cham: Springer; 2023

[6] Zhu X, Goldberg AB. Introduction to semi-supervised learning. In: Synthesis Lectures on Artificial Intelligence and Machine Learning. USA: Springer International Publishing; 2009

[7] Goodfellow I, Bengio Y, Courville A. Deep Learning. Cambridge, MA, US: MIT Press; 2016

[8] Schmidhuber J. Deep learning in neural networks: An overview. Neural Networks. 2015;**61**:85-117. arXiv:1404.7828. DOI: 10.1016/j.neunet.2014.09.003

[9] Lee D, Seo H, Jung MW. Neural basis of reinforcement learning and decision making. Annual Review of Neuroscience. 2012;**35**(1):287-308. DOI: 10.1146/annurev-neuro-062111-150512

[10] Bishop CM. Pattern Recognition and Machine Learning. New York: Springer; 2006

[11] ASM Handbook Committee. Properties and Selection: Irons, Steels, and High-Performance Alloys. Vol. 1. USA: ASM Handbook Committee – ASM International; 1990

[12] Lee J-Y, Kim M, Lee Y-K. Design of high strength medium-Mn steel using machine learning. Materials Science & Engineering: A, Structural Materials: Properties, Microstructure and Processing. 2022;**843**:143-148

[13] Wang Z-L, Adachi Y. Property prediction and properties-to-microstructure inverse analysis of steels by a machine-learning approach. Materials Science and Engineering: A. 2019;**744**:661-670

[14] Lee JW, Park C, Do Lee B, et al. A machine-learning-based alloy design platform that enables both forward and inverse predictions for thermo-mechanically controlled processed (TMCP) steel alloys. Scientific Reports. 2021;**11**:11012. DOI: 10.1038/s41598-021-90237-z

[15] Coelho LB, Torres D, Vangrunderbeek V, et al. Estimating pitting descriptors of 316 L stainless steel by machine learning and statistical analysis. NPJ Materials Degradation. 2023;**7**:82. DOI: 10.1038/s41529-023-00403-z

[16] Aghaaminiha M, Mehrani R, Colahan M, Brown B, Singer M, Nesic S, et al. Machine learning modeling of time-dependent corrosion rates of carbon steel in presence of corrosion inhibitors.

Corrosion Science. 2021;**193**:109904. DOI: 10.1016/j.corsci.2021.109904

[17] Kim SW, Kang SH, Kim SJ, et al. Estimating the phase volume fraction of multi-phase steel via unsupervised deep learning. Scientific Reports. 2021;**11**:5902. DOI: 10.1038/s41598-021-85407-y

[18] Kusampudi N, Diehl M. Inverse design of dual-phase steel microstructures using generative machine learning model and Bayesian optimization. International Journal of Plasticity. 2023;**171**:103776. DOI: 10.1016/j.ijplas.2023.103776

[19] Gyasi EA, Handroos H, Kah P. Survey on artificial intelligence [AI] applied in welding: A future scenario of the influence of AI on technological, economic, educational and social changes. Procedia Manufacturing. 2019;**38**:702-714. DOI: 10.1016/j.promfg.2020.01.095

[20] Tran N-H, Bui V-H, Hoang V-T. Development of an artificial intelligence-based system for predicting weld bead geometry. Applied Sciences. 2023;**13**(7):4232. DOI: 10.3390/app13074232

[21] Abd Halim S, Manurung YHP, Raziq MA, et al. Quality prediction and classification of resistance spot weld using artificial neural network with open-sourced, self-executable and GUI-based application tool Q-Check. Scientific Reports. 2023;**13**:3013

[22] Wang X, Chen Q, Sun H, Wang X, Yan H. GMAW welding procedure expert system based on machine learning. Intelligence & Robotics. 2023;**3**(1):56-75. DOI: 10.20517/ir.2023.03

Chapter 3

Experimental and Industrial Experience with Steel and Air-Cooled Blast Furnace Slag Concrete

Pavel Martauz and Vojtěch Václavík

Abstract

This chapter presents experimental and industrial experience with the use of steel slag and air-cooled blast furnace slag in the production of concrete as a new sustainable and environmentally friendly building material. Steel slag and air-cooled blast furnace slag replace 100% of the natural aggregate fractions 0/32 mm. The strength characteristics of the sustainable concrete placed in laboratory and outdoor environments and its pictorial analysis are presented.

Keywords: steel slag, air-cooled blast furnace slag, concrete, structure, physical and mechanical properties

1. Introduction

Most of the production and non-production activities of today's society are accompanied by the generation of by-products and waste. The issue of their disposal or rational use is, therefore, a primary task today in terms of environmental protection and circular economy.

The various industries are looking for ways of producing with little or no by-products and waste. Where this cannot be achieved, the use of by-products and waste in other production sectors is being addressed.

Recycling and use of by-products and waste enables savings to be made in primary raw materials and energy resources, delays the depletion of natural resources and contributes to the protection of the environment, which is threatened by the accumulation of waste, its dust, water contamination and land occupation.

In the construction industry, the use of by-products and waste from the metallurgical industry, the energy and mining industries, waste produced by building materials plants and some waste from other production and collection facilities is also an option. To date, some by-products of metallurgical production, energy by-products and some components of construction and demolition waste have been processed to the greatest extent in this sector.

The production of iron and steel is always accompanied by the generation of by-products which are either returnable, reusable materials for the whole production process or material that is unusable in further production and is wasted. Reducing this wasted, non-returnable material to minimum values is currently an urgent challenge,

given the price of raw materials, the promotion of a circular economy and the sustainable development of society.

Even though by-product producers (steel slag and blast furnace slag) try to minimize the amount that is landfilled and process it as much as possible into secondary raw materials, a significant proportion is still landfilled.

Sustainable steel slag-based building materials are now known. Steel slag from electric arc furnaces fr. 0/5, 5/12 and 12/25 mm can be used as a partial substitute for natural aggregate in concrete production [1–4], similar to mechanically treated steel slag [5]. Modified steel slag is also used as a substitute for natural aggregate in asphaltic concrete [6, 7]. Modified steel slag by mechanical activation can be used as an addition in the production of concrete [8]. The results of a research that investigated the use of recycled steel slag in the production of Portland cement concrete are presented in [9].

Granulated blast furnace slag has a wide range of long-term applications in cement production. A prospective regional application of finely ground blast furnace slag is alkali-activated concrete [10–12]. Finely ground granulated blast furnace slag in combination with fly ash can be used as an addition in the production of concrete [13]. Finely ground granulated blast furnace slag can be combined with recycled concrete to produce concretes with defined properties [13]. Research results are also known which address the substitution of natural coarse aggregate in quantities of 25, 50 and 100% granulated blast furnace slag and electric arc furnace slag (EAFS) in concrete production [14].

Concrete prepared with steel and air-cooled blast furnace slag is one of the sustainable construction materials. Sustainable building materials include materials prepared based on by-products and/or wastes from industrial production. These are building materials that have the same or better mechanical and transformation properties than building materials based on natural raw materials. The purpose of using sustainable building materials is to conserve natural resources and reduce the carbon footprint.

In this chapter, we present our results and experience with steel and air-cooled blast furnace slag-based concrete. These by-products from a metallurgical plant were used as a 100% substitute for natural aggregates in concrete production [15, 16].

2. Materials and method

2.1 Steel slag and artificial aggregates

Steel slag is formed as a by-product in the treatment of pig iron in primary and secondary metallurgy [17]. Slag produced in different steel plants has different properties. The main chemical components include CaO, SiO_2, Fe_2O_3, MgO, Al_2O_3, MnO, P_2O_5. The chemical composition of steel slag varies according to the type of furnace, the quality of steel and the method of preparation. **Table 1** presents the chemical composition of steel slag from BOFS (Basic Oxygen Furnace Slag) and EAFS (Electric Arc Furnace Slag). The mineralogical composition of steel slag is variable. The proportion of crystalline phase and glass depends on the crystallization rate of the slag. The following minerals are present in steel slags: dicalcium silicate C_2S, tricalcium silicate C_3S, dicalcium ferrite C_2F, tetracalcium aluminoferrite C_4AF, acermanite, gehlenite, periclase MgO and free CaO [18, 19].

Converter steel slag of fr. 0/8 mm was used for our experimental design. The chemical composition of steel slag is presented in **Table 2**.

Oxides (%)	CaO	SiO_2	Al_2O_3	Fe_2O_3	FeO	MgO	MnO	P_2O_5
BOFS	45–60	10–15	1–5	3–9	7–20	3–13	2–6	1–4
EAFS	30–50	11–20	10–18	5–6	8–22	8–13	5–10	2–5

Table 1.
Chemical composition of steel slag [16].

Analyte	Unit	Result	Uncertainty	Analyte	Unit	Result	Uncertainty
Na_2O	weight %	0.46	±0.10	V	mg/kg	570	—
MgO	weight %	10.2	±1.2	Cr	mg/kg	3.900	—
Al_2O_3	weight %	2.43	±0.27	Ni	mg/kg	25	—
SiO_2	weight %	13.7	±1.3	Cu	mg/kg	38	—
P_2O_5	weight %	0.91	±0.09	Zn	mg/kg	63	—
SO_3	weight %	0.50	±0.06	Sr	mg/kg	130	—
K_2O	weight %	<0.003		Zr	mg/kg	140	—
CaO	weight %	38	± 2	Nb	mg/kg	67	—
TiO_2	weight %	0.29	± 0.02	Mo	mg/kg	36	—
MnO	weight %	3.02	± 0.13	Ba	mg/kg	200	—
Fe total	weight %	22		Ta	mg/kg	110	—
CaO free	weight %	2.34	± 0.24	W	mg/kg	86	—
—	—	—	—	Loss by annealing	weight %	−0.74	—

Table 2.
Chemical composition of converter steel slag (CSS) fr. 0/8 mm [16].

Chemical composition	Result	
SiO_2	35–45%	ø 39%
Al_2O_3	5–10%	ø 8%
MgO	5–15%	ø 9%
CaO	35–45%	ø 37%
CaO free	0.7–1.1%	ø 0.9%

Table 3.
Chemical composition of ACBFS [16].

Air-cooled blast furnace slag (ACBFS) is one of the basic types of artificial aggregates. It is formed as a waste product in the production of iron. It is similar to natural igneous rocks. It is included in European technical standards together with natural resources aggregates and is subject to the same normative requirements. Coarse artificial aggregate of fr. 8/16 and 16/32 mm was used for our experimental research. The chemical composition is given in **Table 3**.

Table 4 presents the average values of properties of converter steel slag (CSS) of fr. 0/4 mm and fr. 4/8 mm and air-cooled blast furnace slag (ACBFS) of fr. 8/16 mm and fr. 16/32 mm. Specific weight and absorption were determined according to EN 1097-6 [20], specific weight in tapped state and the void content were determined according to EN 1097-3 [21].

All these fractions of converter steel slag (CSS) and air-cooled blast furnace slag (ACBFS) shown in **Table 4** were subjected to a granulometric analysis according to EN 933-1 [22]. Based on the performed tests and with the help of C-Packing software, the optimal grain size curve of the combination of CSS and ACBFS fr. 0/32 mm was developed, which consists of CSS fr. 0/4 mm (32.0%), CSS fr. 4/8 mm (18.0%), ACBFS fr. 8/16 mm (20.0%) and ACBFS fr. 16/32 (30.0%). It follows from the above that the ratio of the filler CSS and ACBFS is 50:50%. Based on the results of the granulometric analysis (see **Figure 1**), the mean grain size was determined as d_{50} from individual grain size curves (see **Table 5**).

Artificial aggregate	**CSS fr. 0/4 mm**	**CSS fr. 4/8 mm**	**ACBFS fr. 8/16 mm**	**ACBFS fr. 16/32 mm**
Specific weight (kg/m^3)	3.294	3.421	2.636	2.640
Loose bulk density—unshaken state (kg/m^3)	2.047	1.700	1.479	1.529
Loose bulk density—shaken state (kg/m^3)	2.380	1.970	1.667	1.767
Voids—unshaken state (%)	37.9	50.3	43.9	42.1
Voids—shaken state (%)	27.7	42.4	36.8	33.1
Water absorption (%)	2.36	2.41	1.36	0.86

Table 4.
Properties of converter steel slag (CSS) and air-cooled blast furnace slag (ACBFS) [16].

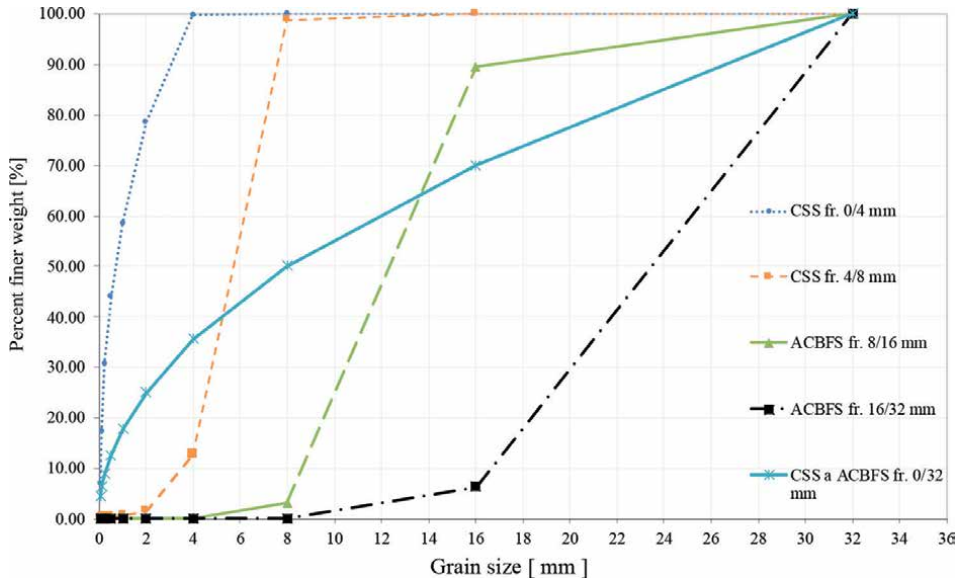

Figure 1.
Steel slag (CSS) and air-cooled blast furnace slag (ACBFS) granulometric curves [16].

Artificial aggregate	CSS fr. 0/4 mm	CSS fr. 4/8 mm	ACBFS fr. 8/16 mm	ACBFS fr. 16/32 mm	CSS + ACBFS fr. 0/32 mm
Medium grain size d_{50} (mm)	0.70	5.73	12.34	23.46	8.00

Table 5.
Medium grain size d_{50} [16].

2.2 Cement, additions, water, superplasticizer

Two types of cement have been used as a binder for the production of steel & air-cooled blast furnace slag-based concrete. These were Portland blended cement CEM II/B-S 42.5N and hybrid cement marked as H-CEMENT. Both types of cements are produced in the company Považská cementáreň, a.s. **Table 6** presents the chemical composition of the cements used and **Table 7** presents their physical and mechanical properties.

A superplasticizer based on modified polycarboxylates Sika ViscoCrete-4035 was used as an admixture for the production of a concrete mixture based on artificial aggregates.

Water from the tap water system was used as mixing water.

2.3 Concrete mix designs

In order to verify the possibility of using converter steel slag (CSS) and air-cooled blast furnace slag (ACBFS) from blast furnace slag as a 100% substitute for natural aggregates of fr. 0/32 mm, three concrete mix designs were developed marked as [16]:

- C—mix based on converter steel slag (CSS), which is represented by fr. 0/4 mm (32%) and fr. 4/8 mm (18%) and air-cooled blast furnace slag (ACBSF) fr. 8/16 mm (20%) and air-cooled blast furnace slag fr. 16/32 mm (30%). CEM

Analyte (%)	Na_2O	MgO	Al_2O_3	SiO_2	SO_3	Cl	K_2O	CaO	Fe_2O_3
H-CEMENT	2.52	1.68	16.91	46.91	3.65	0.01	3.17	17.09	6.47
CEM II/B-S 42.5N	0.34 ± 0.01	3.53 ± 0.04	5.38 ± 0.06	24.48 ± 0.10	3.23 ± 0.09	0.07 ± 0.01	0.83 ± 0.02	53.73 ± 0.30	2.14 ± 0.05

Table 6.
Chemical composition of cements [16].

Type of cement	Specific surface area (m^2/kg)	Initial and final setting time (min.)	Specific weight (kg/m^3)	Compressive strength (MPa)		Flexural strength (MPa)	
				2 days	28 days	2 days	28 days
H-Cement	696.8	230/285	2.770	14.9	39.0	4.1	7.8
CEM II/B-S 42,5N	441.0	280/310	3.030	23.2	53.7	5.4	10.0

Table 7.
Physical and mechanical properties of cements [16].

II/B-S 42.5 N (360 kg/m^3), water (181 kg/m^3) and superplasticizer in the amount of 1% of the weight of cement.

- CH—mix based on converter steel slag (CSS), which is represented by fr. 0/4 mm (32%) and fr. 4/8 mm (18%) and air-cooled blast furnace slag (ACBFS) fr. 8/16 mm (20%) and fr. 16/32 mm (30%). CEM II/B-S 42.5 N (360 kg/m^3) is used as a binder, which is replaced in 30% by the PUZZOLANIT (H-CEMENT 108 kg/m^3) addition, water (181 kg/m^3) and plasticizer in the amount 1.1% of the weight of cement.

- H—mix based on converter steel slag (CSS), which is represented by fr. 0/4 mm (32%) and fr. 4/8 mm (18%) and air-cooled blast furnace slag (ACBFS) fr. 8/16 mm (20%) and fr. 16/32 mm (30%). H-CEMENT 360 kg,m^3), water (191 kg/m^3) and plasticizer in the amount of 1.4% of the weight of cement.

2.4 Production of test specimens

The production of test specimens, according to concrete mix designs (see Chapter 2.3.), took place in two stages (stage I and II). From each design, 4 mixtures with a volume of 20 dm^3 were mixed. Within two stages of the production of concrete test specimens, 160 dm^3 of concrete mixture, 32 cubes with an edge of 150 mm and 6 prisms with dimensions of 100 × 100 × 400 mm were prepared from each concrete mix design. Thus, a total of 480 dm^3 of concrete mixture, 96 cubes and 18 prisms were produced. A forced mixer (cyclone mixer) M80 from FILAMOS, s.r.o. CZ was used for the production of the concrete mixture.

2.5 Placement of test specimens

Test specimens from stage I of the production were placed in a container in an aqueous environment with temperature control, where heating was provided by a heating cable. The water temperature in the test tank with the test specimens was 20°C ± 2.0°C during the whole process. The specimens were placed in the tank for 7, 28 and 90 days in accordance with EN 12390-2 [23]. Test specimens made in stage II were placed in an outdoor environment of the company Považská cementáreň, a.s. in August, September and October 2017. Temperature characteristics and precipitation totals for these months are given in [16].

Two methods of placing the test specimens were chosen in order to determine whether the environment in which the test specimens are placed affects the resulting properties of steel & air-cooled blast furnace slag-based concrete.

The third method of placement of test specimens (dimensions 40x40x160 mm, which were cut out from a cube with an edge of 150 mm) was chosen in sewage wastewater (in a septic tank) in the company Považská cementáreň, a.s. [16].

2.6 Methodology of concrete properties tests

The properties of the fresh concrete mixture were determined in accordance with applicable normative regulations. Determination of the specific weight of a fresh concrete mixture was performed according to EN 12350-6 [24], determination of the consistency of a fresh concrete mixture according to EN 12350-5 [25] and determination of the air content in a fresh concrete mixture according to EN 12350-7 [26]. Determination of strength characteristics of hardened concrete was performed

according to EN 12390-3 [23] and the dynamic modulus of elasticity according to CSN 731371 [27]. A Non-Destructive 3D X-Ray Computed Tomography method was used to visualize the structure and basic porosity analysis of steel & air-cooled blast furnace slag-based concrete. The analyzed specimens were scanned on a Nikon Metrology XT H 450 2D/3T X-Ray Computed Tomography.

3. Results and discussion

3.1 Rheological properties of cements

To determine the optimal amount of PUZZOLANIT (H-CEMENT) in combination with Portland blended cement CEM II/B-S 42.5N, tests of the rheological properties of the cements used were performed. The rheological properties were determined on a Viskomat NT Schleibinger. The result of the measurement is the measured torque (Nmm) over time. The comparative cement was Portland blended cement CEM II/B-S 42.5N. It was found that with a 20 and 40% replacement of CEM II/B-S 42.5N by H-CEMENT, the workability was the least affected [16]. Based on the obtained results of rheology of cements used for the production of the concrete mixture based on CSS and ACBFS, a 30% replacement of CEM II/B-S 42.5N by H-CEMENT was chosen, where H-CEMENT was used as a mineral addition II of the kind marked PUZZOLANIT. Determination of the rheology of the used cement was done according to the methodology of Považská cementáreň, a.s.

3.2 Properties of a fresh concrete mixture

Determination of the properties of the fresh concrete mixture (consistency, air content and specific weight) was performed in stages I and II of the production of test specimens. Within one stage, 4 mixtures were always made, within two stages, 8 mixtures were made, i.e. the average value of the properties of the fresh concrete mixture was calculated from 8 values. The results are presented in **Table 7**.

The results in **Table 8** show that:

a. The pouring values of the fresh concrete mixture correspond to a consistency F2 of 350–410 mm for mix C and CH and a consistency F1 ≤ 340 mm for mix H. From the above, it is clear that when using H-CEMENT as a binder in the production of concrete based on CSS and ACBFS, it is necessary to take into account the reduction of the workability value of the fresh concrete mixture if H-CEMENT dosing is in the same amount as CEM II/B-S 42.5N. When using H-CEMENT as an addition (PUZZOLANIT) in the amount of 30% in concrete, the consistency of the fresh concrete mixture will not be significantly affected.

Mix	Consistency (mm)	Air content (%)	Specific weight (kg/m^3)
C	408 (±45)	2.1 (±0.3)	2656 (±31)
CH	400 (±28)	2.0 (±0.1)	2653 (±14)
H	333 (±25)	2.2 (±0.3)	2623 (±23)

Table 8.
Properties of fresh concrete mixture [16].

b. Replacement of CEM II/B-S 42.5N cement with H-CEMENT as an addition (PUZZOLANIT) at 30% and 100% has no effect on the air content of fresh concrete mix with CSS and ACBFS. The change of the binder does not affect the air content in the fresh concrete mixture.

c. The values of the specific weight of the fresh concrete mixture demonstrate the suitability of using CSS and ACBFS as a 100% substitute for natural aggregates and various types of binder, without the specific weight of the fresh concrete mixture being significantly affected by the repeatability of the concrete mixture production.

3.3 Strength characteristics of concrete

Figure 2 shows the results of cube strengths after 7, 28 and 90 days of age of test specimens from the first stage of production of the test specimens, which were placed in a water environment.

From the above picture, it can be seen that the placement in water suits the test specimens that were prepared using CEM II/B-S 42.5N (mix C) and CEM II/B-S 42.5N in combination with H-CEMENT (mix CH). These test specimens show a gradual increase in cube strength after 7, 28 and 90 days of age of the test specimens. This is also confirmed by the value of the coefficient of determination, which is R = 0.98 (mix C) and R = 0.96 (mix CH). A very low and gradual increase in the strength of concrete of test specimens placed in a water environment was demonstrated for formula H, the coefficient of determination R = 0.55.

Figure 3 shows the results of cube strengths after 7, 28 and 90 days of age of test specimens from the second stage of production of test specimens, which were placed outdoors. An increase in cube strengths is evident in all test specimens prepared according to experimental mixes. However, when comparing the coefficient of determination of the experimental mixes, where the test specimens were placed in aqueous and outdoor environments, it is clear that the outdoor environment for placing test specimens caused the value of the coefficient of determination to decrease for mix C to R = 0.90, for mix

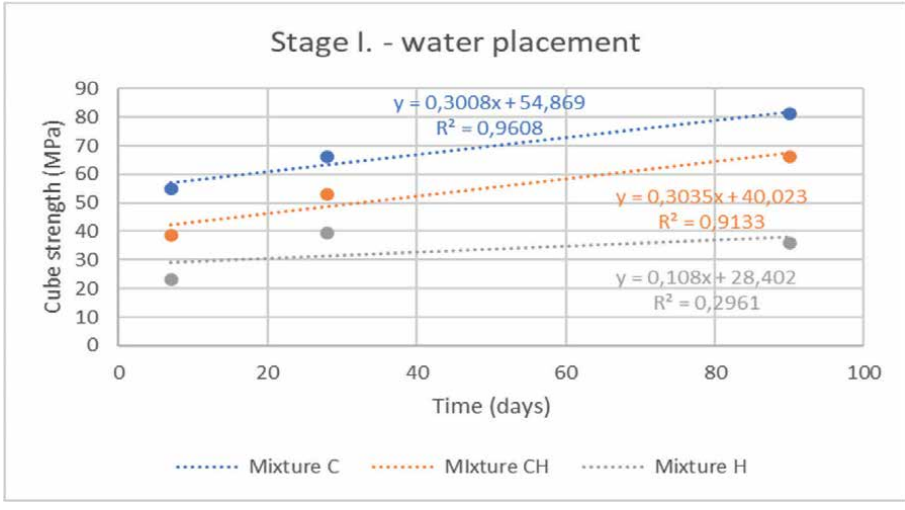

Figure 2.
Cube strength of concrete according to experimental mixes—placement in water [16].

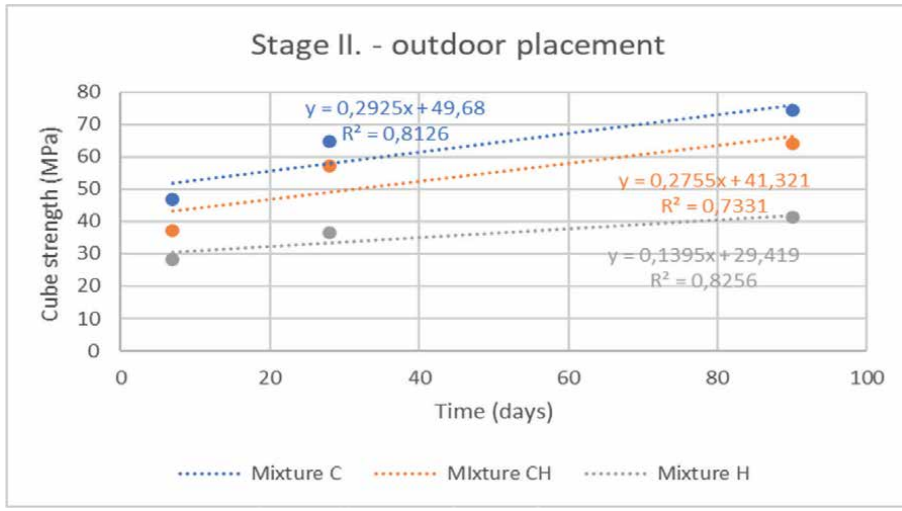

Figure 3.
Cube strength of concrete according to experimental mixes—outdoor installation [16].

CH to R = 0.86. On the contrary, an increase of the coefficient of determination was found in test specimens made from the H-CEMENT-based mix H to the value R = 0.91.

Figure 4 presents the dependence of the dynamic modulus of elasticity on the cube strength. The dynamic modulus of elasticity was determined after 28 days on prisms with the dimensions of 100 × 100 × 400 mm. The research found that the test specimens, which were placed in an aqueous environment, show a dependence where the increase in compressive strength is accompanied by an increase in the value of the dynamic modulus of elasticity with the value of the coefficient of determination R = 0.91. For the test specimens that were placed outdoors, a slight increase in the dynamic modulus of elasticity with the value of the coefficient of determination R = 0.95 is evident.

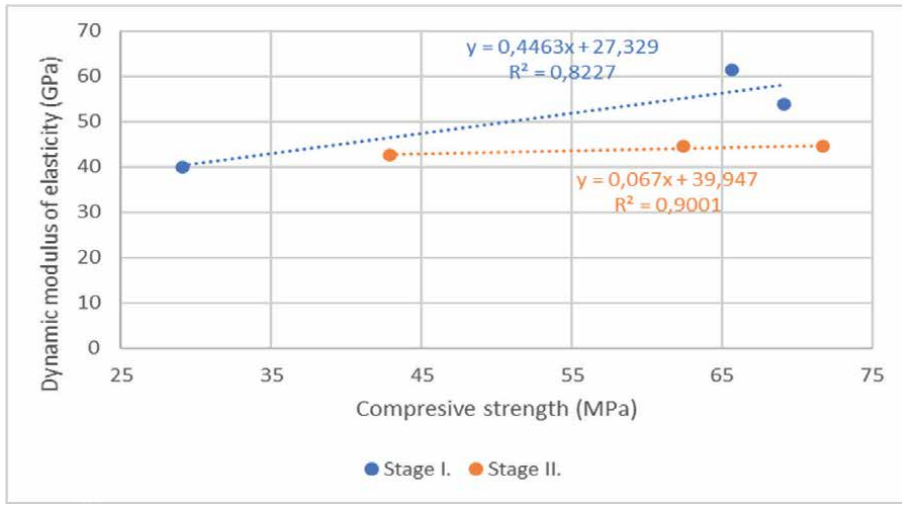

Figure 4.
Dependence of the dynamic modulus of elasticity on cube strength (water and outdoor placement).

3.4 Structure of concrete

In order to analyze the concrete structure using 3D X-Ray Computed Tomography, test bodies in the shape of a cylinder with a diameter of 43 mm and a height of 100 mm (marked as 1A, 2A, 3A and 2B) were prepared from the semi-operational verification of the production of concrete based on CSS and ACBFS (formulation H) at the concrete plant for the subsequent production of pavement in the industrial area of Považská cementáreň, a.s. (see **Figure 5**). For the CT analysis itself, only a part of the bodies in the area of the upper base of the cylinder (without specimen description) was scanned in order to achieve the most detailed CT scan of the analyzed object, i.e. the projection of the diameter of the analyzed test body onto the width of the X-ray detector. The scanned and analyzed fragment of the test body was represented by a cylinder with a height of approximately 50 mm.

3.4.1 Visualization of the internal structure of concrete specimens

After reconstructing the tomographic (CT) volumes of the individual test bodies in the "3D CT Pro" software, the individual tomographic volumes of the same concrete test body were imported into the "VGStudio MAX" software. In this software, the individual tomographic volumes and 2D CT sections were visualized. The visualization of the internal structure of the concrete was performed using 2D CT sections at 8-bit resolution, representing a range of 256 shades of gray (0—black, 256—white). Darker shades represent low density materials, lighter shades represent denser materials in the analyzed concrete specimens (see **Figure 5**). The characteristic structure of the analyzed concrete is evident from **Figures 6** and 7.

From the reconnaissance of the internal structure of the concrete under review based on the CT sections of each test body, it can be concluded (see **Figures 6** and 7) that in the analyzed concrete, its four basic components of concrete can be identified, namely:

- Cement paste (CP),
- A fraction formed by the sharp-edged grains of steel slag of fr. 0/8 mm (abbreviated to CSS), it is the densest component of concrete, represented by the lightest shades of gray,

Figure 5.
View of the CSS and ACBFS concrete pavement.

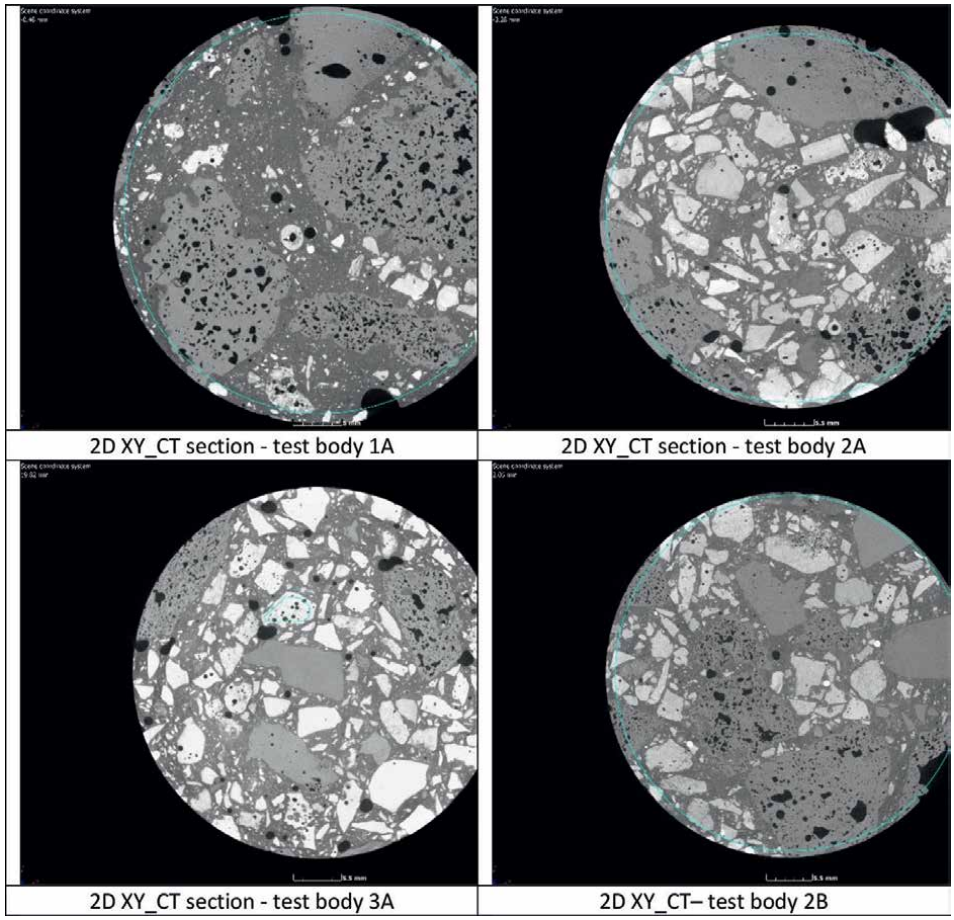

Figure 6.
Example of visualization of the internal structure of the analyzed concrete in the CT section of the XY plane.

- A concrete fraction represented mainly by sub-oval grains of air-cooled blast furnace slag (ACBFS) of fr. 8/32 mm, it is the second densest concrete component,

- The last component of the concrete consists of pores (P) represented by the darkest shades of gray (black color), identifiable as technologically mixed bubble pores, mostly pseudo-spherical to ellipsoidal in appearance and irregularly shaped pores, which are significantly represented in ACBFS grains, and to a lesser extent in OC grains.

The tomographic CT sections show concrete that does not visibly exhibit contraction-type inhomogeneities and other mechanical cracks in the cement binder at a given resolution level. The grains are well anchored in the cement paste with no visible circumferential separation cracks. Significant inhomogeneities are represented by mixed technological bubbles (pores). A high proportion of pores is also evident in the ACBFS grains. From the tomographic 2D sections, only the primary disturbances in the form of cracks localized in the grains of the different aggregate fractions (CSS and ACBFS) are visible, probably caused by their processing, for instances (see **Figures 6** and 7).

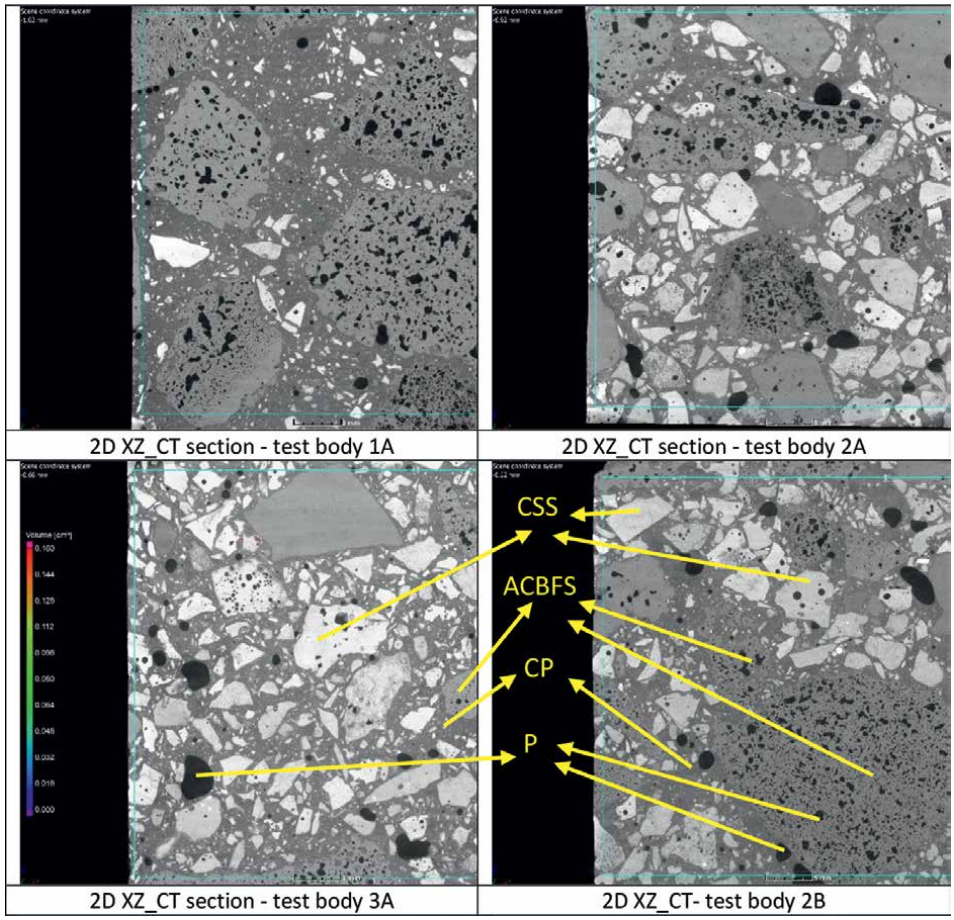

Figure 7.
Example of visualization of the internal structure of the analyzed concrete in the CT section of the XZ plane, with marking of the individual concrete components (CSS: converter steel slag; ACBFS: and air-cooled blast furnace slag, CP: cement paste, and P: pore).

3.4.2 An analysis of the pore space in the concrete under review

The porosity analysis was performed using the software "VGStudio Max 3.3.2". In the first part of the porosity analysis, a region of interest (ROIall) in the shape of a cylinder with a volume of about 55–59 cm^3 was selected in each tomographic volume of the test body. The total porosity was measured including the pores located within the grains of each fraction of the concrete under review. In all porosity analyses, the smallest pores analyzed were assumed to have a volume of approx. 0.0001 mm^3 (the lower limit of the filter setting of the software module "Defect detection").

The segmentation of the pore space was performed using a threshold value representing the gray level of individual voxels in the tomographic sections at eight-bit resolution. This threshold for the analysis of the primary pore space was determined manually using the means in the software module "Defect detection/only threshold/voids/define manualy", i.e. a region was selected from which the average value of

voxels representing the pores was determined. An average voxel value was also determined in the adjacent area of the analyzed pore matrix of concrete with aggregate, from which a value was set for the concrete material. Based on these two values, a threshold value was determined for the pore segmentation algorithm in the software module used.

Figure 8 shows an illustrative and typical example of the pore space segmentation result of concrete specimen 1A.

From the analysis performed on the concrete specimens (1A, 2A, 3A and 2B), it is clear that the analyzed concrete exhibits heterogeneity in terms of the distribution and frequency of individual pores in the volume of the test bodies (mainly influenced by the presence of ACBFS grains), as well as in terms of their size. The different pore sizes are particularly evident in the case of the technological mixed bubbles (pores), for example, in concrete specimen 2A and 3A, where the pore size reaches up to about 3–5 mm. These facts can be documented graphically in **Figure 9**, showing the porosity pattern in the direction of the longitudinal "Z" axis of the cylindrical test bodies evaluated from tomographic volumes with a thickness of 0.1 mm. The graph shows that the porosity values vary in the direction of the longitudinal axis of the test bodies within a range of approximately 2–12% (Note: The 0 mm position represents the centre of the test body region of interest in the direction of the "Z" axis).

The average porosity of the analyzed concrete determined from the results of the measurements on all four test bodies is represented by the value of 6.5 ± 1.52% (coefficient of variability of about 24%). Furthermore, the porosity in the individual fractions of the analyzed concrete was determined using irregular ROIs placed in the individual grains of the CSS and ACBFS fraction. The resulting porosity values show a high variability, which is due to the limited choice of ROI size in the individual grains. The average porosity value from the measurements on all test bodies for the CSS

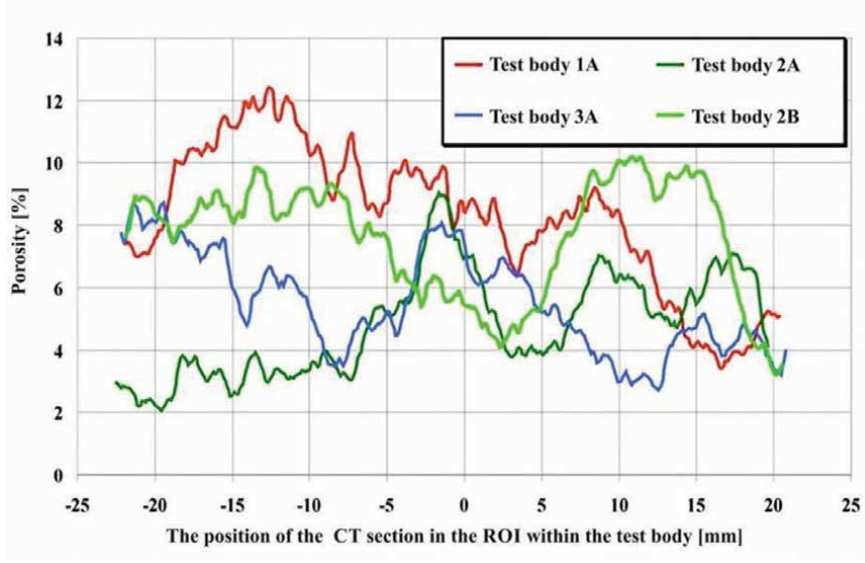

Figure 8.
An illustrative example of pore space segmentation results—Test body 1A, the cylindrical ROI is shown as the light blue line.

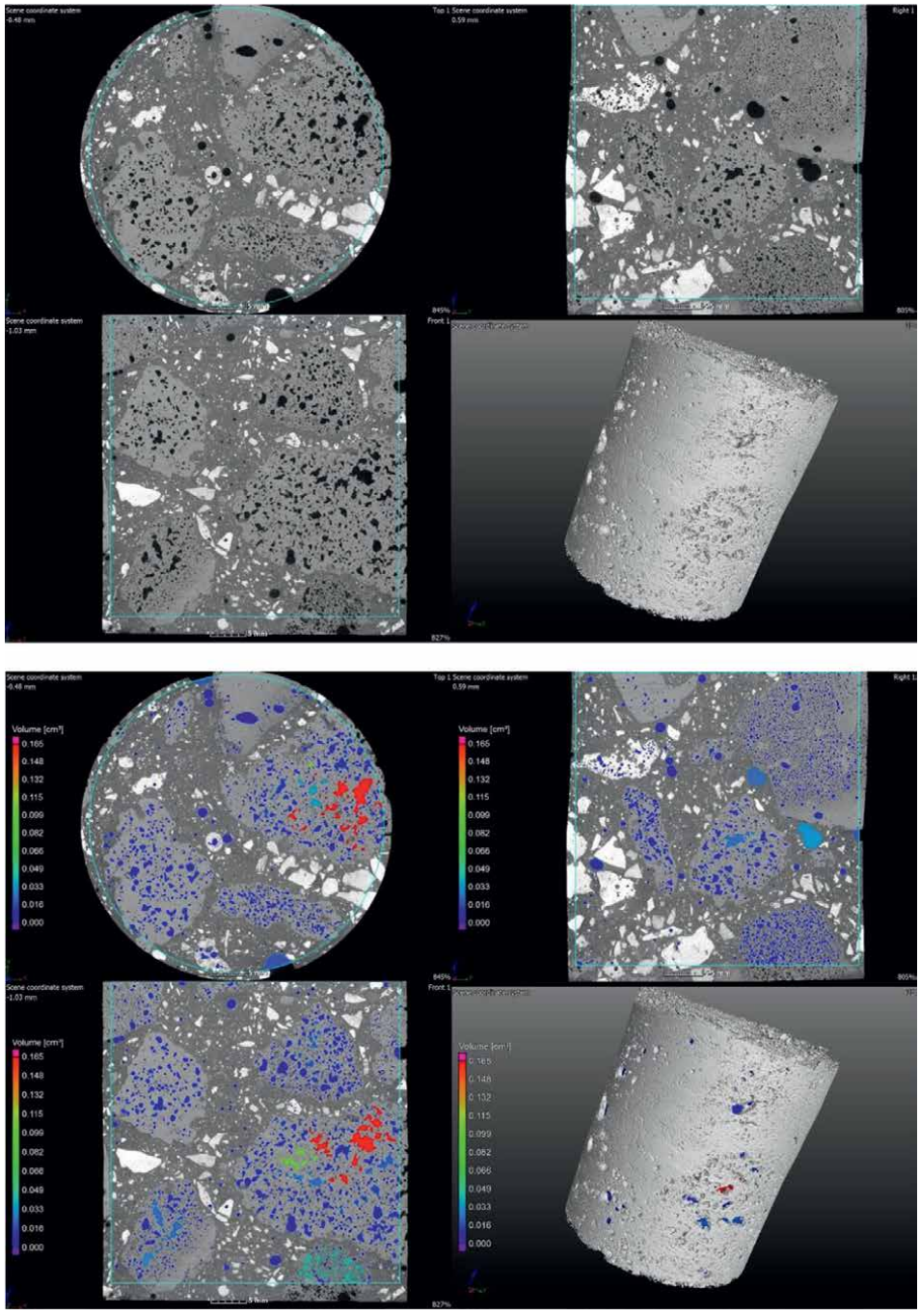

Figure 9.
Trend in porosity values in the concrete test bodies along the Z-axis (CT sections in the XY plane with a thickness of 0.1 mm).

fraction is 5.5 ± 3.38% (coefficient of variability of about 62%), whilst for the ACBFS fraction, the average porosity value is 16 ± 9.53% (coefficient of variability of about 62%).

3.4.3 Determination of the volume and visualization of the individual components of the analyzed concrete in 3D view

In the analyzed concrete, four basic components can be identified:

- Cement paste (CP),
- A fraction formed by the sharp-edged grains of steel slag steel (CSS),
- A concrete fraction represented mainly by sub-oval grains of artificial dense aggregate (ACBFS),
- A component of the concrete consisting of pores (P) represented by the darkest shades of gray (black color).

These concrete components also correspond to the distribution of the values of the individual voxels in the tomographic volume, which are also (not only visually) well distinguishable (identifiable) in the histogram of the values of the individual gray shades. The histograms were developed based on the filtered tomographic data. The filtering was performed to eliminate the influence of noise in the tomographic data on the distribution of values in the CT volumes of the test bodies. By filtering the CT data, a more significant interface between the different components of the tested concrete was achieved. **Figure 10** then shows the way of segmenting the different concrete components for their 2D and 3D representation and determining their volumetric representation in the test body volume. **Figure 11** shows the visualization of the individual components by coloring the intervals of gray values corresponding to the identifiable concrete components.

The volume of the individual components in the test bodies of the analyzed concrete specimen is shown in **Table 9**. This volume corresponds to the volume of all voxels belonging to a given segmentation interval. It is important to note that, for all solid components (CSS and ACBFS), this volume corresponds only to the volume of their material ("skeleton") without including the volume of their pores. The volume of all pores is included in the P component.

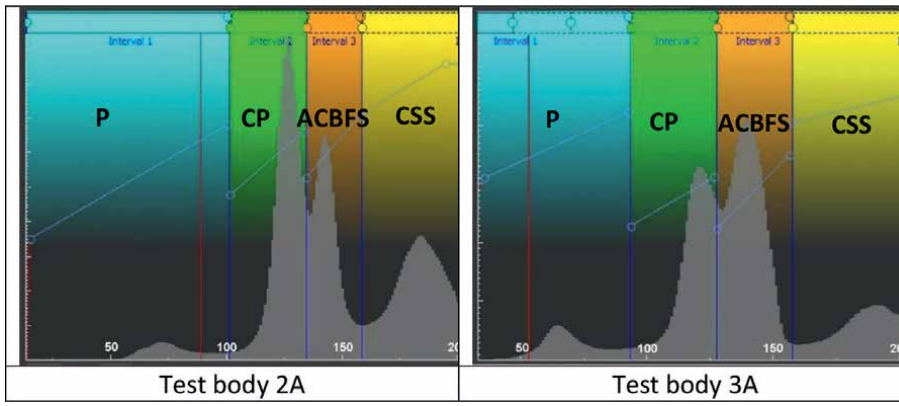

Figure 10.
An illustrative example of the distribution of gray level values in a CT volume of analyzed concrete, segmentation of individual concrete components using the coloring method (CSS: converter steel slag; ACBFS: and air-cooled blast furnace slag, CP: cement paste, and P: pore).

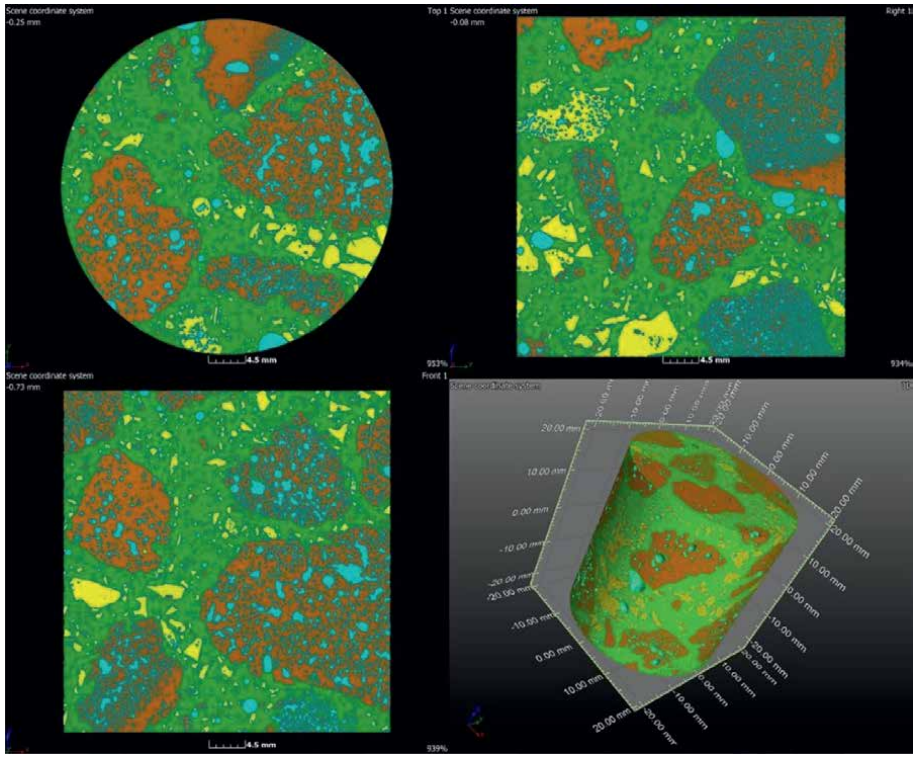

Figure 11.
Visualization of the segmentation of the individual components of the analyzed concrete test body 1A.

Specimen	1A	2A	3A	2B	Average	Standard deviation	Coeff. var.
	Total volume of component (cm^3)	Total volume of component (cm^3)	Total volume of component (cm^3)	Total volume of component (cm^3)			
CSS_without pores	4.427	18.455	14.517	11.672	—	—	—
P	4.496	2.482	3.074	4.300	—	—	—
CP_without pores	22.889	20.177	21.401	16.573	—	—	—
ACBFS _without pores	23.374	14.521	17.085	26.407	—	—	—
Total analysis volume (cm^3)	55.186	55.635	56.077	58.952	56.5	1.47	2.6
Share of CSS (%)	8.02	33.17	25.89	19.80	21.7	9.22	42.4
Share of P (%)	8.15	4.50	5.57	7.79	6.5	1.52	23.4
Share of CP (%)	41.48	36.56	38.78	30.03	36.7	4.23	11.5
Share of ACBFS (%)	42.35	26.31	30.96	47.85	36.9	8.62	23.4

Table 9.
Volume of the individual components in the test bodies of the tested concrete.

In the volumetric analysis of the individual components of concrete on the four test bodies (see **Table 9**), cement paste is represented by about 36.7%. This material shows the least variability in all the test bodies of concrete, i.e. about 11.5%. A similar volumetric representation of 36.9% is also attributed to the ACBFS fraction but with about twice the coefficient of variability, i.e. 23%. The porosity value shows an identical variability with a pore volume representation of 6.5% in concrete. The CSS fraction accounts on average for 21.7% of the concrete volume, but, in this case, the highest variability in the occurrence of this fraction in the analyzed bodies was found. The value of the coefficient of variability for the CSS fraction was approximately 42%. The values of the volume representation of the individual fractions ACBFS, CP and CSS correspond only to the volume of their material ("skeleton") without including the volume of their pores. The volume of all pores in the concrete is included in the P component.

4. Conclusion

Our chapter presents experiences and results from research on the use of by-products from metallurgical production in concrete production. On the basis of industrial experience, we can draw the following conclusion:

- The combination of converter steel slag (CSS) of fr. 0/8 mm and air-cooled blast furnace slag (ACBFS) of fr. 8/32 mm can be used as a 100% substitute for natural aggregate in concrete production.

- Converter steel slag (CSS) of fr. 0/8 mm and air-cooled blast furnace slag (ACBFS) of fr. 8/32 mm does not affect the air content of fresh concrete. For the proposed formulations (C, CH and H), the air content ranged from 2.0 to 2.2%.

- In the production of fresh concrete with CSS and ACBFS of fr. 8/32 mm, the repeatability of fresh concrete production was demonstrated without a significant change in fresh concrete specific weight values. The fresh concrete specific weight was in the range of 2620–2660 kg/m^3.

- The consistency of fresh concrete based on CSS fr. 0/8 mm and ACBFS fr. 8/32 mm can be adjusted to the desired value with the help of a plasticizing admixture, whilst maintaining the value of the water coefficient.

- On the basis of our designed formulations for concrete based on CSS fr. 0/8 mm and ACBFS fr. 8/32 mm (see Chapter 2.3), we can prepare concrete with a cube strength of 40–80 MPa after 90 days and a flexural strength of 5–8 MPa after 28 days.

- It has been shown that the placement of test bodies in a water and outdoor environment has a significant effect on the strength characteristics of concrete based on converter steel slag (CSS) fr. 0/8 mm and air-cooled blast furnace slag (ACBFS) fr. 8/32 mm). Outdoor placement of the test bodies will cause a reduction in strength compared to the aqueous environment. This applies to the cube strengths determined after 90 days for formulations C (an 8% reduction) and CH (a 3% reduction).

- The use of H-CEMENT (see formulation H, Chapter 2.3) has proven to be successful for test bodies that have been stored in an outdoor environment. There was a 14% increase in cube strength after 90 days and a 37% increase in flexural strength after 28 days compared to the cube strength and flexural strength of the test bodies stored in an aqueous environment.

- 3D X-Ray Computed Tomography can be used to analyze the structure of concrete based on by-products of industrial production by identifying the grains of converter steel slag (CSS), air-cooled blast furnace slag (ACBFS), cement paste and the contact zone between the aggregate grain and cement paste.

- The results of 3D X-ray computed tomography of concrete show that:

- Concrete does not exhibit contraction-type inhomogeneities and other mechanical cracks in the cement paste.

- Steel and air-cooled blast furnace slag grains are well anchored in the cement paste. The contact zone between the aggregate grains and the cement paste is not disturbed.

- Significant inhomogeneities in the structure are represented by technological bubbles (air pores).

- Air-cooled blast furnace slag has a high proportion of pores, average porosity value of 16 ± 9.53%.

- Steel slag shows a porosity value of 5.5 ± 3.38%.

- The average porosity value of concrete prepared on the basis of converter steel slag (CSS) fr. 0/8 mm and air-cooled blast furnace slag (ACBFS) fr. 8/32 mm) accounts for 6.5 ± 1.52%.

- In the production of concretes based on converter steel slag (CSS) fr. 0/8 mm and air-cooled blast furnace slag (ACBFS) fr. 8/32 mm), it is advisable to use alkali-activated H-CEMENT as a binder, which will increase the strength of concrete placed outdoors and also help to reduce CO_2 emissions compared to CEM II/B-S 42,5N.

- The use of a potentially expansive converter steel slag with air-cooled blast furnace slag and a potential combination of binders did not produce the frequently published volumetric changes in concrete with the formation of destructive cracks.

- The potential uses of concrete with steel and air-cooled blast furnace slag may be as follows:

- Production of precast concrete elements e.g. road panels, concrete fences, protective concrete elements against terrorist attacks by vehicles in areas where large numbers of people are present;

- Manufacture of concrete weights;
- Concrete pavements;
- Industrial environments.

Acknowledgements

This article has been written in collaboration with the laboratory of Považská cementáreň, a.s., ul. Janka Kráľa, 018 63 Ladce, Slovakia, thanks to Ing. Katarína Martauzová and Mrs. Helena Habánková.

Author details

Pavel Martauz[1] and Vojtěch Václavík[2*]

1 Cement Plant—Považská Cementáreň, a.s., Ladce, Slovakia

2 Faculty of Mining and Geology, Department of Environmental Engineering, VSB-Technical University of Ostrava, Czech Republic

*Address all correspondence to: vojtech.vaclavik@vsb.cz

References

[1] Faleschini F, Alejandro Fernández-Ruíz M, Zanini MA, Brunelli K, Pellegrino C, Hernández-Montes E. High performance concrete with electric arc furnace slag as aggregate: Mechanical and durability properties. Construction and Building Materials. 2015;**101**:113-121. DOI: 10.1016/j.conbuildmat.2015.10.022

[2] Pellegrino C, Gaddo V. Mechanical and durability characteristics of concrete containing EAF slag as aggregate. Cement and Concrete Composites. 2009;**31**:663-671. DOI: 10.1016/j.cemconcomp.2009.05.006

[3] Abu-Eishah SI, El-Dieb AS, Bedir MS. Performance of concrete mixtures made with electric arc furnace (EAF) steel slag aggregate produced in the Arabian gulf region. Construction and Building Materials. 2012;**34**:249-256. DOI: 10.1016/j.conbuildmat.2012.02.012

[4] San-José JT, Vegas I, Arribas I, Marcos I. The performance of steel-making slag concretes in the hardened state. Materials & Design. 2014;**60**:612-619. DOI: 10.1016/j.matdes.2014.04.030

[5] Yi H, Xu G, Cheng H, Wang J, Wan Y, Chen H. An overview of utilization of steel slag. Procedia Environmental Sciences. 2012;**16**:791-801. DOI: 10.1016/j.proenv.2012.10.108

[6] Kourounis S, Tsivilis S, Tsakiridis PE, Papadimitriou GD, Tsibouki Z. Properties and hydration of blended cements with steelmaking slag. Cement and Concrete Research. 2007;**37**:815-822. DOI: 10.1016/j.cemconres.2007.03.008

[7] Zhang T, Yu Q, Wei J, Li J, Zhang P. Preparation of high performance blended cements and reclamation of iron concentrate from basic oxygen furnace steel slag. Resources, Conservation and Recycling. 2011;**56**:48-55. DOI: 10.1016/j.resconrec.2011.09.003

[8] Kriskova L, Pontikes Y, Cizer Ö, Mertens G, Veulemans W, Geysen D, et al. Effect of mechanical activation on the hydraulic properties of stainless steel slags. Cement and Concrete Research. 2012;**42**:778-788. DOI: 10.1016/j.cemconres.2012.02.016

[9] Dong Q, Wang G, Chen X, Tan J, Gu X. Recycling of steel slag aggregate in Portland cement concrete: An overview. Journal of Cleaner Production. 2021;**282**:124447. DOI: 10.1016/j.jclepro.2020.124447

[10] Mengasini L, Mavroulidou M, Gunn MJ. Alkali-activated concrete mixes with ground granulated blast furnace slag and paper sludge ash in seawater environments. Sustainable Chemistry and Pharmacy. 2021;**20**:100380. DOI: 10.1016/j.scp.2021.100380

[11] Wei X, Li D, Ming F, Yang C, Chen L, Liu Y. Influence of low-temperature curing on the mechanical strength, hydration process, and microstructure of alkali-activated fly ash and ground granulated blast furnace slag mortar. Construction and Building Materials. 2021;**269**:121811. DOI: 10.1016/j.conbuildmat.2020.121811

[12] Kranthi Vijaya S, Jagadeeswari K, Lal Mohiddin S, Srinivas K. Stiffness determination of alkali activated ground granulated blast furnace slag based geo-polymer concrete. Materials Today: Proceedings. 2020. DOI: 10.1016/j.matpr.2020.10.775

[13] Gholampour A, Zheng J, Ozbakkaloglu T. Development of

waste-based concretes containing foundry sand, recycled fine aggregate, ground granulated blast furnace slag and fly ash. Construction and Building Materials. 2021;**267**:121004. DOI: 10.1016/j.conbuildmat.2020.121004

[14] Etxeberria M, Pacheco C, Meneses JM, Berridi I. Properties of concrete using metallurgical industrial by-products as aggregates. Construction and Building Materials. 2010;**24**:1594-1600. DOI: 10.1016/j.conbuildmat.2010.02.034

[15] Martauz P, Vaclavik V, Cvopa B. The use of steel slag in concrete. IOP Conference Series: Earth Environmental Science. 2017;**92**:012041. DOI: 10.1088/1755-1315/92/1/012041

[16] Martauz P, Václavík V, Cvopa B. The influence of the environment on the properties of hybrid cement-based concrete with steel and air-cooled slags. Crystals. 2021;**11**:1087. DOI: 10.3390/cryst11091087

[17] Shi C. Steel slag—Its production, processing, characteristics, and cementitious properties. Journal of Materials in Civil Engineering. 2004;**16**:230-236. DOI: 10.1061/(ASCE)0899-1561(2004)16:3(230)

[18] Abhishek P, Ramachandra P, Niranjan PS. Use of recycled concrete aggregate and granulated blast furnace slag in self-compacting concrete. Materials Today: Proceedings. 2020. DOI: 10.1016/j.matpr.2020.10.239

[19] Marinković S, Radonjanin V, Malešev M, Ignjatović I. Comparative environmental assessment of natural and recycled aggregate concrete. Waste Management. 2010;**30**:2255-2264. DOI: 10.1016/j.wasman.2010.04.012

[20] EN 1097-6. Tests for mechanical and physical properties of aggregates—Part 6: Determination of particle density and water absorption; 2014

[21] EN 1097-3. Tests for mechanical and physical properties of aggregates—Part 3: Determination of loose bulk density and voids; 1999

[22] EN 933-1. Tests for geometrical properties of aggregates—Part 1: Determination of particle size distribution—Sieving method; 2012

[23] EN 12390-2. Testing hardened concrete—Part 2: Making and curing specimens for strength tests; 2020

[24] TEN 12350-6. Testing fresh concrete—Part 6: Density; 2020

[25] EN 12350-5. Testing fresh concrete—Part 5: Flow table test; 2020

[26] EN 12350-7. Testing fresh concrete—Part 7: Air content—Pressure methods; 2020

[27] CSN 731371. Non-destructive testing of concrete—Method of ultrasonic pulse testing of concrete; 2011

Chapter 4

Service Life of Steam Turbine Rotor Material Made of Low-Alloy Cr-Mo-V Steels after Long-Term Use outside the Design Operating Time of Power Unit

Joanna Furmanek and Janusz Dobrzański

Abstract

The purpose of the study was to assess the state and degree of exhaustion of turbine rotor materials made of low-alloy Cr-Mo-V steels after long-term operation. The tests were carried out for selected structure states defined on the basis of images of the structure observed using a scanning electron microscope, and the degree of development of precipitation processes based on the X-ray analysis of the phase composition of electrolytically isolated carbide deposits. For materials with such defined structure states and degree of development of precipitation processes, the following were determined: mechanical properties at room and elevated temperatures, residual life and available residual life on the basis of short-term creep tests, and creep rate from creep curves for temperature and stress parameters corresponding to operational parameters. Based on the results of short-term creep tests conducted at a temperature higher than the operational temperature and with a stress corresponding to the operational life, residual and available residual life were determined and the degree of exhaustion was estimated.

Keywords: Cr-Mo-V steel, microstructure, mechanical properties, short-term creep tests, creep rate, residual life, diagram of microstructure change

1. Introduction

Łukasiewicz Research Network — Upper Silesian Institute of Technology (formerly Łukasiewicz Research Network — Institute for Ferrous Metallurgy) has been carrying out research for several decades, aimed at creating diagnostic rules, developing methods and methodology for assessing the service life of critical components of the pressure part of power units, i.e. those operating in the most difficult temperature and stress conditions in a time significantly exceeding the design time [1–10]. These works cover various issues, including the development of a methodology to assess the condition of these components and forecast their

further safe operation. The tools for assessing materials include a database in the field of properties and structure after use of materials applied in these components. For the proper assessment of the material condition, it is necessary to classify the condition of the structure in relation to the degree of exhaustion, which prove the condition of the assessed material and its suitability for further operation. Critical components operating above the limit temperature, i.e. in conditions where creep is the main or significant destruction process that determines changes in the material during operation, include components of the pressure part of the boiler and turbine, which include rotor shafts. It is also important to determine the type of carbides and their impact on the performance properties of rotor steels [11–13]. The paper covers the issues of assessing the suitability of the rotor material for operation after exceeding the design operating time, assessing their microstructural state and the set of functional properties corresponding to this structure. It is a response to the needs of the professional power industry in terms of conducting a reliable assessment of the condition and a reliable forecast of further safe operation in the conditions expected and defined by the owners of such facilities, especially for components whose actual service life exceeded the design time.

2. Test samples

The material for the tests consisted of sections of the medium-pressure SP and high-pressure HP parts of the TK200 and 18 K360 steam turbine rotors of power units with a nominal power of 200 and 360 MW after long-term operation significantly exceeding the unit's design operating time of 100,000 hours, made of low-alloy ternary Cr-Mo-V steel (21HMF).

To obtain representative material for testing, it was assumed that it should be characterised by a structure from one that did not differ from that characteristic of the initial state to a structure that was quite degraded. The choice of locations for testing was determined by design parameters for individual areas, as well as preliminary structure tests. Detailed locations from which the material for destructive testing was taken and their operational parameters are shown in **Figure 1** (material No. 1–5).

The results of the control analysis of the chemical composition of the materials under test and the required chemical composition of the tested Cr-Mo-V (21HMF) steel intended for forged rods and turbine shaft forgings according to the PN-75/H-84024 standard are summarised in **Table 1**.

The method of collecting samples for carrying out particular types of destructive material tests is shown graphically in **Figure 2** on the example of the material of the HP high-pressure part of the 18 K360 turbine rotor, No. 4 (**Figure 2a**), and the material of the HP high-pressure part of the TK 200 turbine rotor, No. 2b.

3. Methodology of assessing the condition of the structure depending on the degree of exhaustion

An objective assessment of the durability of a material operating in creep conditions is possible only on the basis of a set of materials science methods and research

DOI: http://dx.doi.org/10.5772/intechopen.111892

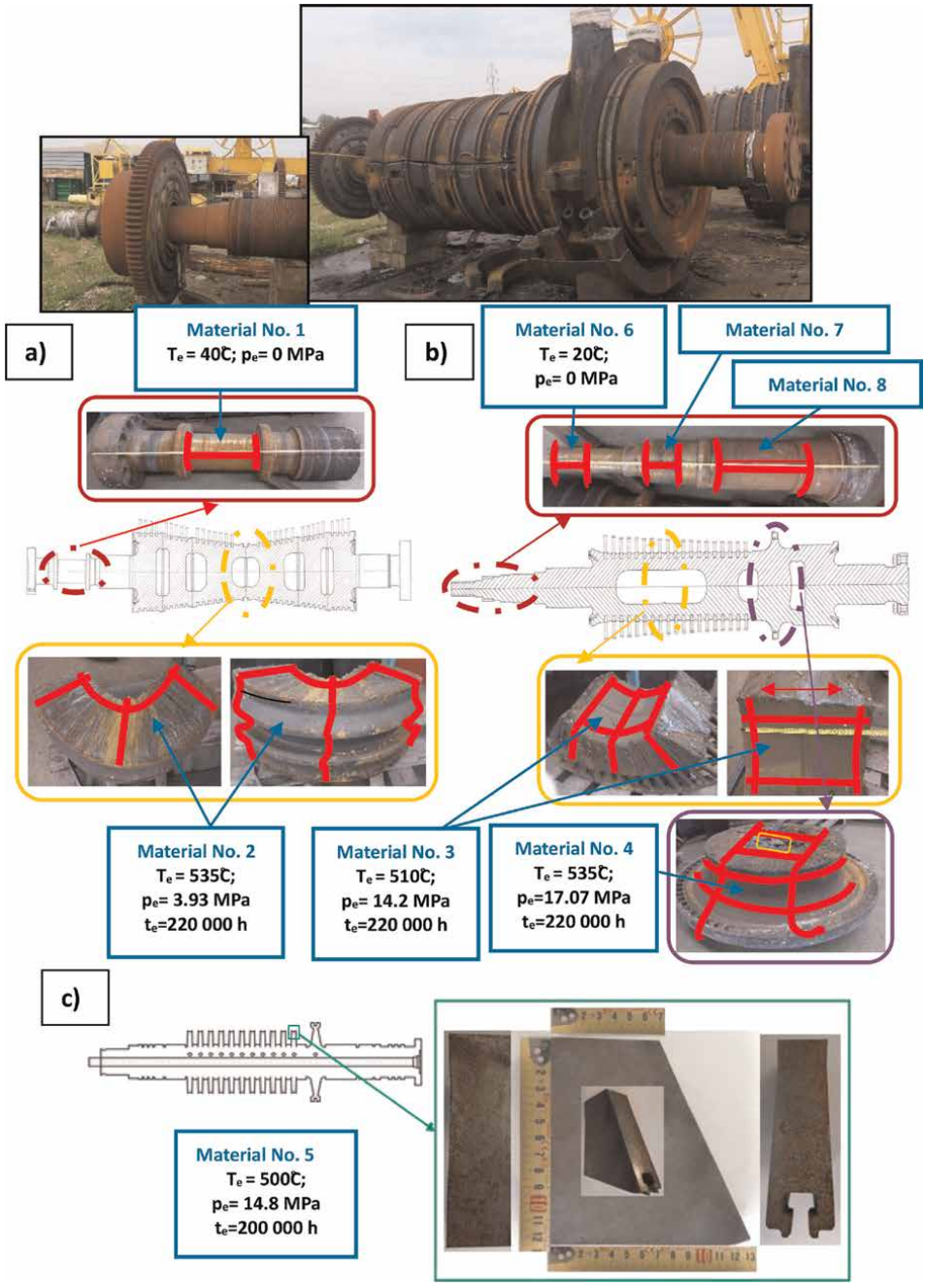

Figure 1.
Method and location of sampling from steam turbine rotors made of Cr-Mo-V steel (21HMF) after long-term operation, significantly beyond the unit's design operating time.

techniques, including results of microstructure examination, examination of mechanical properties and calculation methods.

The material of the components of the pressure part of the boiler, pipelines and turbine operating in creep conditions or with a significant percentage of creep is

Steel grade	Item ID	Element content, [%]								
		C	Mn	Si	P max.	S max.	Cr	Ni max.	Mo	V
Cr-Mo-V (21HMF)	Material 1	0.22	0.35	0.33	0.007	<0.003	1.40	0.55	1.08	0.32
	Material 2	0.22	0.37	0.34	0.011	< 0.003	1.41	0.58	0.97	0.30
	Material 3	0.21	0.49	0.23	0.009	0.012	1.24	0.55	0.80	0.27
	Material 4	0.20	0.48	0.23	0.007	0.010	1.22	0.55	0,80	0.27
	Material 5	0.23	0.46	0.33	0.009	0.012	1.28	0.51	1.08	0.29
	PN-75/H-84024 1975	**0.17 ÷ 0.25**	**0.30 ÷ 0.50**	**0.30 ÷ 0.60**	**0.035**	**0.035**	**1.20 ÷ 1.50**	**0.60**	**1.0 ÷ 1.2**	**0.25 ÷ 0.35**

Table 1.
Control analysis of the chemical composition of the tested materials of steam turbine rotors after long-term operation and requirements for low-alloy ternary Cr-Mo-V steel (21HMF).

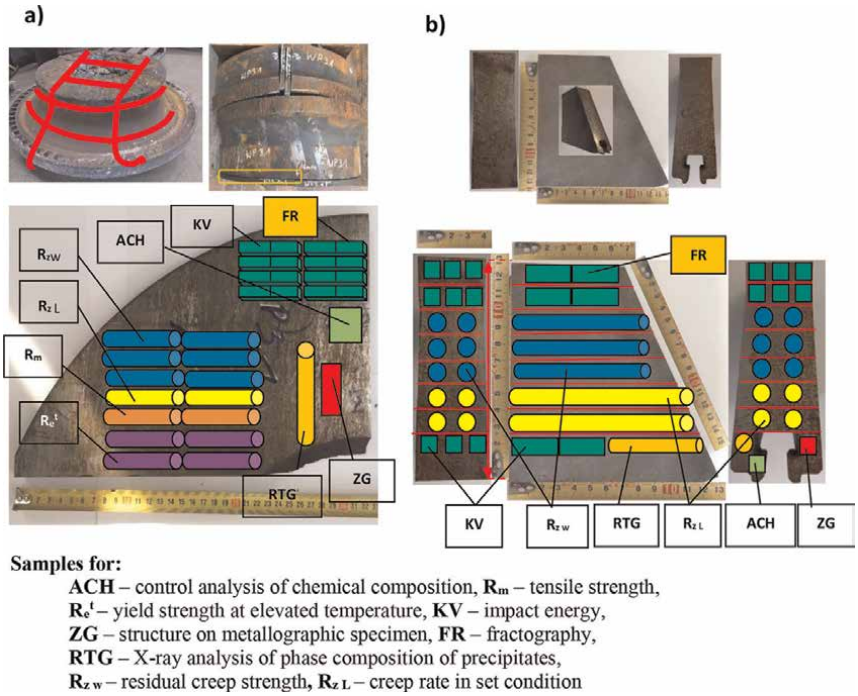

Figure 2.
Type and location of sampling for destructive testing of the material of steam turbine rotors after long-term operation significantly beyond the unit's design operating time, on the example of: (a) material of the HP high-pressure part of the 18 K360 turbine rotor, No. 4, (b) material of the HP high-pressure part of the TK 200 turbine rotor, No. 5.

assessed using non-destructive and destructive methods. The selection of diagnostic methods for assessing the condition of the material is made each time depending on the type of component, its operating time in relation to the assumed design time and the nature of its operation. Regardless of the service life, an assessment of the material microstructure is required. Its purpose is to determine the class of microstructure

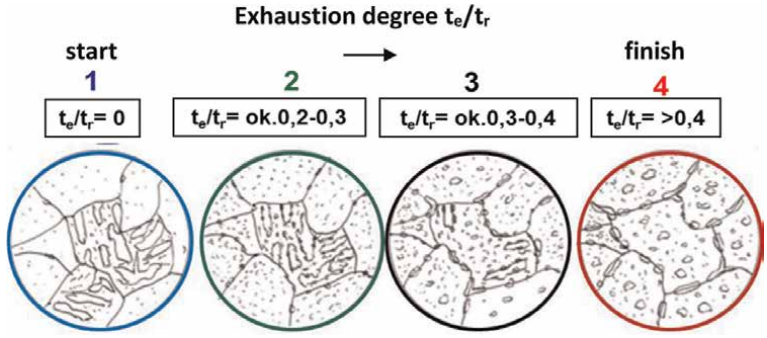

Figure 3.
Model for microstructural evolution in ferritic-pearlitic steels [3].

based on observations using a scanning electron microscope and to estimate the degree of material exhaustion. They determine its ability to carry operating loads. In addition, they allow to determine the working time until the next inspection, which is a safe time for further operation.

Based on the results of many years of own research, patterns of structure were developed, illustrating the successive stages of its changes defined in the prepared classifications, including for the tested steel [1–10]. The structure change model related to the degree of exhaustion defined as the ratio of service life t_e to expected time to failure t_r for low-alloy ternary ferritic-bainite steels is shown in **Figure 3**. This model is also applicable to the low-alloy Cr-Mo-V (21HMF) steel, being the subject of this study.

The methodology for assessing the condition of low-alloy Cr-Mo and Cr-Mo-V steels operating in creep conditions based on changes in the microstructure based on constituent processes, in relation to the degree of exhaustion, is shown graphically in **Figure 4**. In the case of this group of steels, the constituent processes determining changes in the structure as a result of exploitation include pearlite/bainite disintegration, development of precipitation processes and internal damage processes as a result of creep. The dynamics of their changes depending on the degree of exhaustion are shown in **Figure 4a**. On the other hand, **Figure 4b** shows the classes of constituent processes and the corresponding main class of structure related to the creep stage and the degree of exhaustion.

The developed classification consists of two parts. The first part of the classification includes tested steels after use without internal damage. The second part of the classification consists of changes, developed for materials with internal damage due to creep, in the structure depending on the degree of exhaustion [1, 3]. This publication is limited only to the assessment of material conditions without internal damage caused by creep.

4. Structure examination

4.1 Structure observed using scanning electron microscope

Microstructure examination was carried out on etched metallographic specimens taken from fragments of sections of material of steam turbine rotors. The

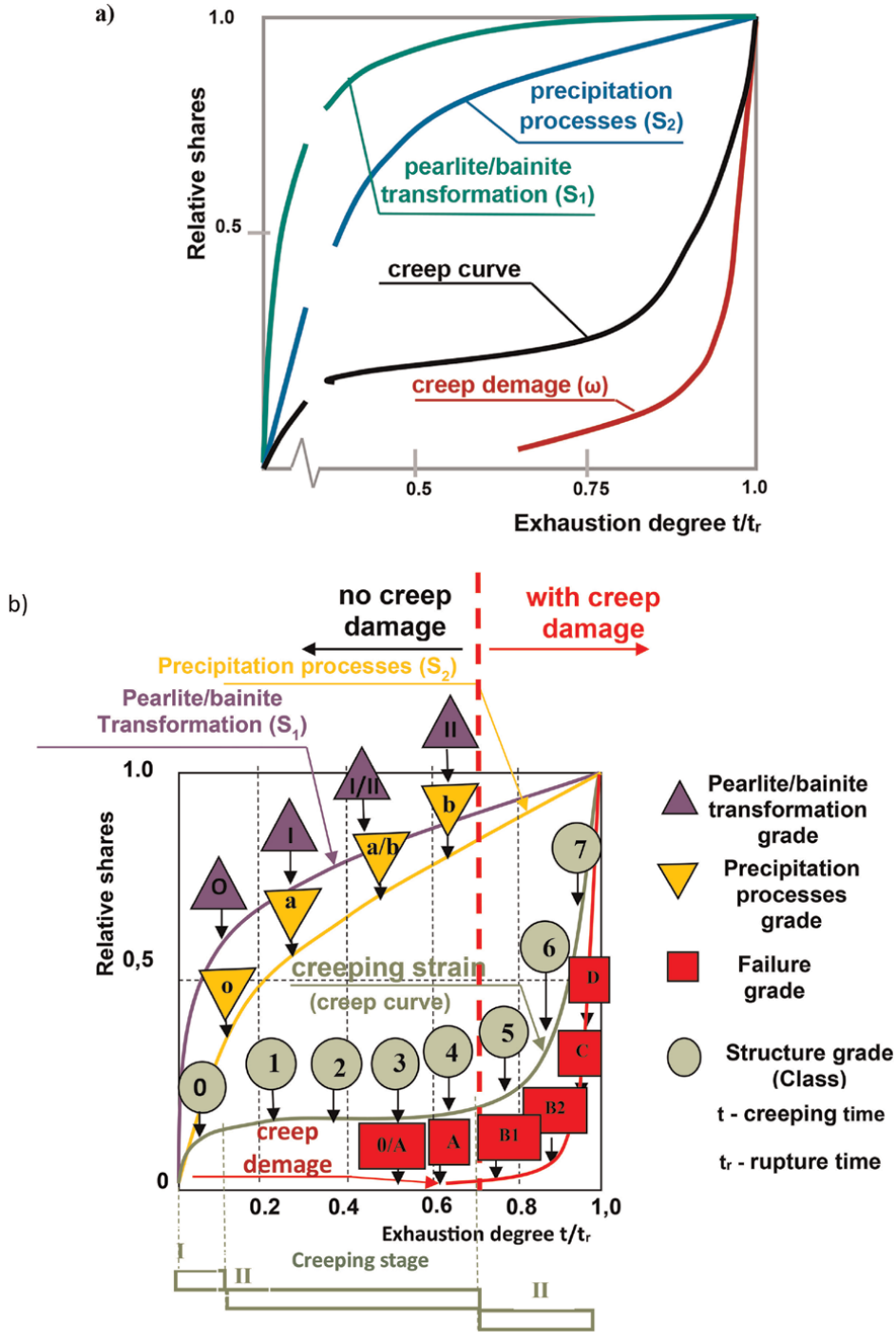

Figure 4.
Classification method of material condition on the basis of changes in the structure based on constituent processes in relation to the degree of exhaustion for ferritic-pearlitic steels used under creep conditions [3].

structure was observed using a scanning electron microscope. They included the assessment of the state of the basic phase components, assessment of the state of development of precipitation processes and the state of development of internal damage resulting from the effects of long-term operation load. The assessment of the structural condition was performed in accordance with Łukasiewicz-GIT's (Łukasiewicz Research Network – Upper Silesian Institute of Technology) own classification in the form of a structure class and the corresponding degree of exhaustion determined on the basis of the state of bainitic areas for the revealed ferritic-bainitic structure and the degree of development of precipitation processes and the state of internal damage. In the assessment of the degree of development of precipitation processes, tables of chemical composition from selected micro-areas, including precipitates, were also used, as well as maps of distribution and concentration of selected elements (the map of precipitates for material No. 5 is shown in **Figure 5**). Representative images illustrating the state of structural components are shown in **Figure 6**. A description of the state of the structure and the assessment result obtained are presented in **Table 2**.

Material No. 1 from the SP part of the rotor, where the operating temperature is close to room temperature and is about 40°C, is characterised by bainite with quite numerous precipitates. The image of the microstructure corresponds to the typical microstructure of the initial state of the rotor material from the tested steel (**Figure 6a**). The results of analyses of the chemical composition of micro-areas including precipitates, as well as the X-ray analysis of precipitates collected electrolytically showed the presence of iron-rich M_3C cementite as the main carbide phase, chromium-rich M_7C_3 carbides and small MC precipitates rich in vanadium in a large amount and a small amount of M_2C carbides rich in molybdenum (**Figure 7a**). In addition, the image of the structure and the state of development of the precipitation processes correlate with the hardness of about 235 HV10 — a level corresponding to the initial state of the rotor material from the tested steel. The material was assigned in accordance with the methodology described in point 3 of the study to class O and the degree of exhaustion $t_r/t_e = 0$.

Material No. 2 from the SP part of the rotor, where the operating temperature was 535°C, is characterised by bainite with quite numerous precipitates on the boundaries of the plates and inside them (**Figure 6b**). Partially preserved bainite plates can be observed in the material of the studied area. Precipitates, probably of chromium-rich M_7C_3 carbide, forming chains, were observed on the boundaries of the bainite plates. Also, within these areas, a significant number of fine precipitates were revealed, which, based on their morphological features, can be identified as vanadium-rich MC precipitates, significant M_3C cementite precipitates and small elongated molybdenum-rich M_2C precipitates. The image of the structure corresponds to the level of hardness, which does not differ from that characteristic for the initial state and amounts to approx. 236 HV10. The material was assigned in accordance with the methodology described in point 3 of the study to class 1 and the degree of exhaustion $t_r/t_e = \sim 0.2$.

Material No. 3 from the HP part of the rotor, where the operating temperature was 510°C, is characterised by bainite with numerous precipitates on the boundaries of the plates and inside them (**Figure 6c**). Partial disappearance of bainite plates can be observed in the material of the examined area. Precipitates, probably of chromium-rich M_7C_3 carbide, forming chains, were observed on the boundaries of bainite plates. Also, within these areas, a significant number of precipitates were revealed, which by

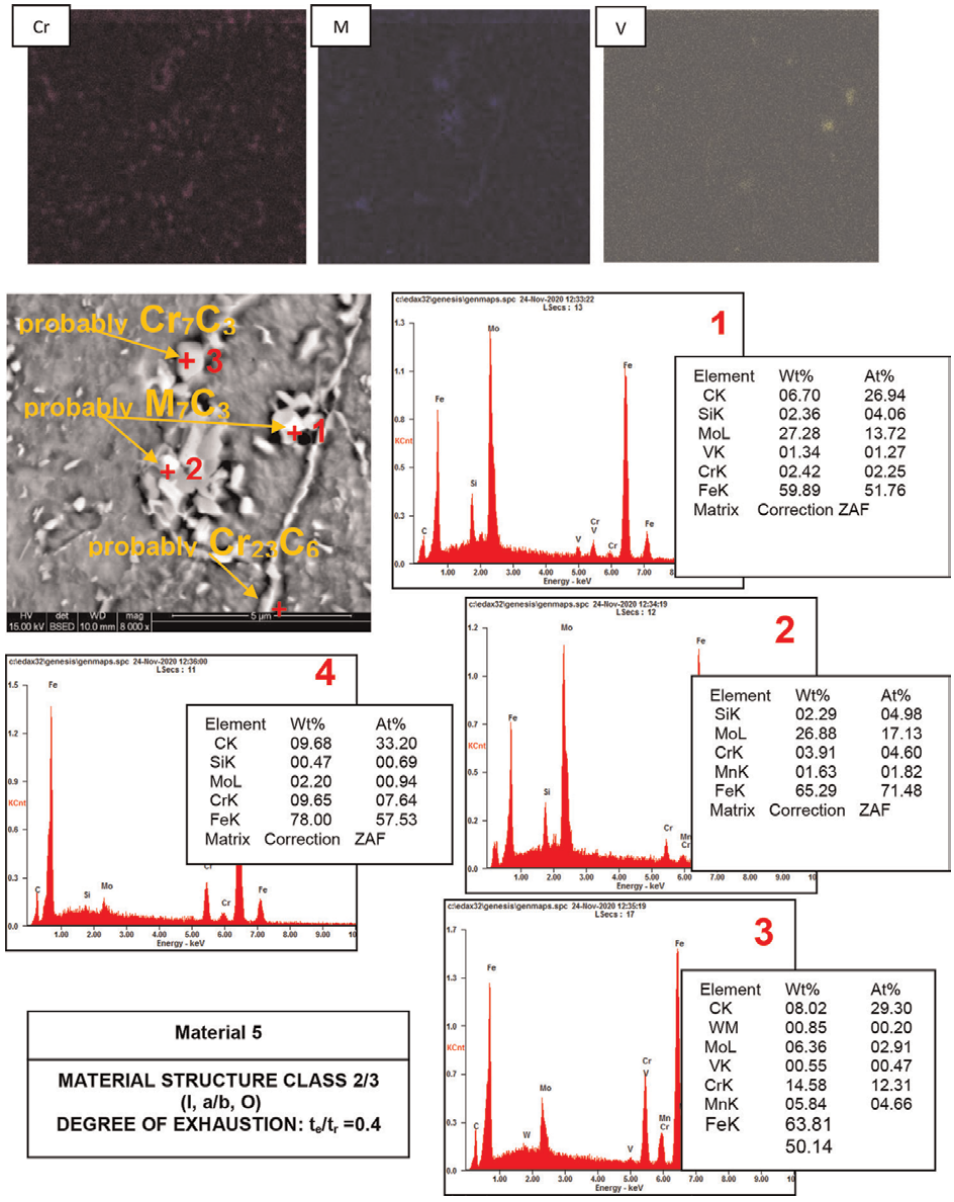

Figure 5.
Example of assessment of the probability of occurrence of particular types of carbide precipitates on the basis of maps of occurrence and intensity of selected carbide-forming elements, chemical composition of micro-areas and morphological features in the material of a steam turbine rotor made of Cr-Mo-V (21HMF) steel after long-term operation.

their characteristics can be identified as vanadium-rich MC precipitates, numerous M_3C cementite precipitates and small elongated molybdenum-rich M_2C precipitates. The partial disappearance of bainite plates was also confirmed by the lower hardness. The material was assigned in accordance with the methodology described in point 3 of the study to class 2 and the degree of exhaustion t_r/t_e = ~ 0.3.

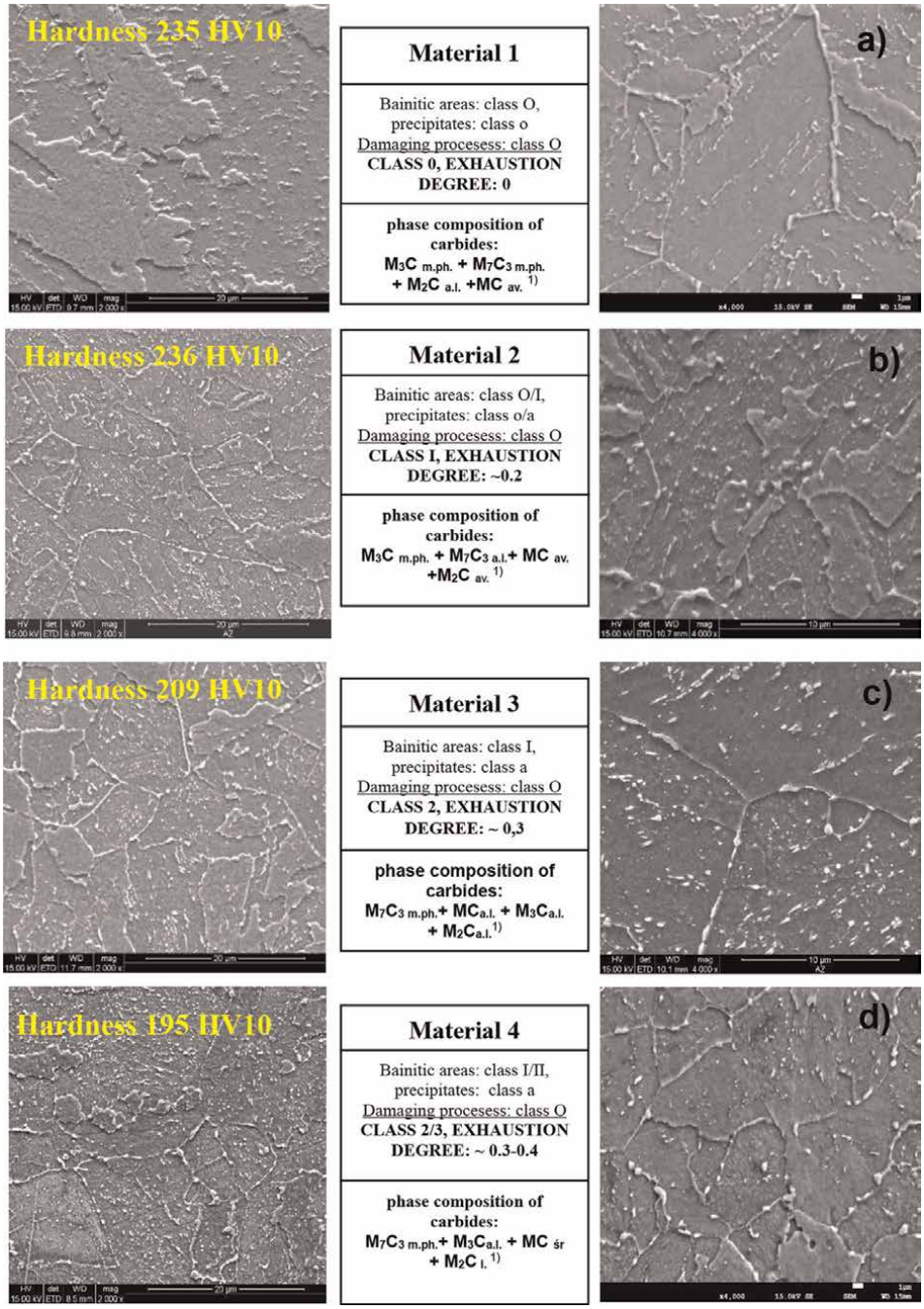

Figure 6.
Determined classes of structure, classes of development of precipitation processes and degree of exhaustion of turbine rotor materials made of Cr-Mo-V steel (21HMF) after long-term operation in relation to the initial state.

Material No. 4 from the HP part of the rotor, where the operating temperature was 535°C, is characterised by bainite with numerous precipitates on the boundaries of the plates and inside them (**Figure 6d**). A significant disappearance of the bainite plates can

Material Figure	**Operating parameters T_r, °C σ_r, MPa**	**Description of microstructure**	**Structural class degree of exhaustion**	**HV hardness**
1	2	4	5	6
Material 1 **Figure 5a**	40 0	Bainitic-ferritic structure. Bainite with numerous, mostly fine, precipitates. The image of the microstructure is similar to the typical microstructure of the initial state of the rotor material from the tested steel. The initiation of internal damage processes is not disclosed. No discontinuities or microcracks were observed in the structure.	(O, o, O) [1)] class 0 t_e/t_r = 0	235
Material 2 **Figure 5b**	535 3.93	Bainitic structure with few ferrite grains. The material is characterised by bainite plates with precipitates at the borders of the plates and a small amount inside them. A significant number of fine precipitates were observed within these areas, which can be identified by their morphological features: finely dispersed as VC precipitates and small elongated Mo_2C. In addition, M_3C cementite in the form of larger precipitates was observed. The initiation of internal damage processes is not disclosed. No discontinuities or microcracks were observed in the structure.	(O/I, o/a, O) [1)] class 1 t_e/t_r = ~0.2	236
Material 3 **Figure 5c**	510 14.2	Bainitic-ferritic structure. The material is characterised by a partial disappearance of the plates and numerous precipitates on the borders of the plates and inside them. Precipitates, probably of M_7C_3 carbide forming chains, were observed on the boundaries of bainite plates. Also, within these areas, a significant number of precipitates were observed, which, based on their morphological features, can be identified as VC and Mo_2C precipitates. The partial disappearance of bainite plates is confirmed by the lower hardness. No initiation of internal damage processes was observed. No discontinuities or microcracks were observed in the structure.	(I, a, O) [1)] class 2 t_e/t_r = ~0.3	209
Material 4 **Figure 5d**	535 17.1	Bainite with few areas of ferrite. Bainite areas with significant loss of bainite plates are characterised by an advanced precipitation process, which is evidenced by numerous precipitates within these areas. Based on their morphological features, it can be assumed that they are fine spheroidal precipitates of vanadium-rich MC carbide and elongated precipitates of molybdenum-rich M_2C carbide. The numerous chain-forming precipitates occurring on the borders of these areas are probably precipitates of $M_{23}C_6$ carbide rich in chromium. No initiation of internal damage processes was observed. No discontinuities or microcracks were observed in the structure.	(I/II, a, O) [1)] class 2/3 t_e/t_r = ~0.3–0.4	195

Material Figure	Operating parameters T_r, °C σ_r, MPa	Description of microstructure	Structural class degree of exhaustion	HV hardness
Material 5	500 14.80	Bainitic-ferritic structure. Bainite with few areas of ferrite. Partial or significant disappearance of bainite areas with a simultaneous significantly advanced precipitation process. Numerous precipitates within bainite areas and on grain boundaries forming chains. No initiation of internal damage processes was observed. No discontinuities or microcracks were observed in the structure.	(I, a/b, O)[1)] class 2/3 t_e/t_r = ~0.4	211

Notes: 1) I – class of bainite disintegration degree, a – class of carbide precipitation processes development, O – class of internal damage processes development.

Table 2.
Results of microstructure examination on etched metallographic specimens of tested materials of steam turbine rotors made of Cr-Mo-V steel (21HMF) after operation outside the design working time of the unit, determined class of structure, corresponding degree of exhaustion and hardness.

be observed in the material of the examined area. Precipitates, probably of M_7C_3 carbide with a significant chromium content, forming chains, were observed on the boundaries of bainite plates. Also, within these areas, a significant number of precipitates were revealed, which, based on their morphological features, can be identified as coagulated M_3C cementite precipitates, fine vanadium-rich MC precipitates and a few molybdenum-rich M_2C precipitates. The number and size of precipitates confirm a significant degree of changes in this area as a result of long-term operation, and their type and share were confirmed by the results of the X-ray phase analysis of precipitate deposits (**Table 3**). The material was assigned in accordance with the methodology described in point 3 of the study to class 2/3 and the degree of exhaustion tr/te = ~ 0.3–0.4.

Material No. 5 from the HP part of the rotor, where the operating temperature was 535°C, is characterised by bainite with few areas of ferrite. Partial or significant disappearance of the bainite plates with a simultaneous significantly advanced precipitation process can be observed in the material of the examined area. Numerous precipitates, quite evenly distributed within the bainite areas, and chain-forming precipitates were observed on grain boundaries. In addition to the types of precipitates revealed in the other tested materials, the presence of $M_{23}C_6$ and M_6C carbides on grain boundaries was observed inside the grains, which confirms the degree of advancement of the precipitating processes in this material. The disclosed state of the structure was also confirmed by the level of hardness. The material was assigned in accordance with the methodology described in point 3 of the study to class 2/3 and the degree of exhaustion t_r/t_e = ~ 0.4.

4.2 X-ray phase analysis of precipitates

The type and amount of precipitates were plotted on an electrolytically isolated deposit of precipitates from the tested materials. The obtained results in the form of X-ray diffraction patterns of precipitates electrolytically isolated for the above materials are shown in **Figure 7**, while **Table 3** shows the phase composition and the share of precipitates based on the identification of the obtained X-ray diffraction patterns.

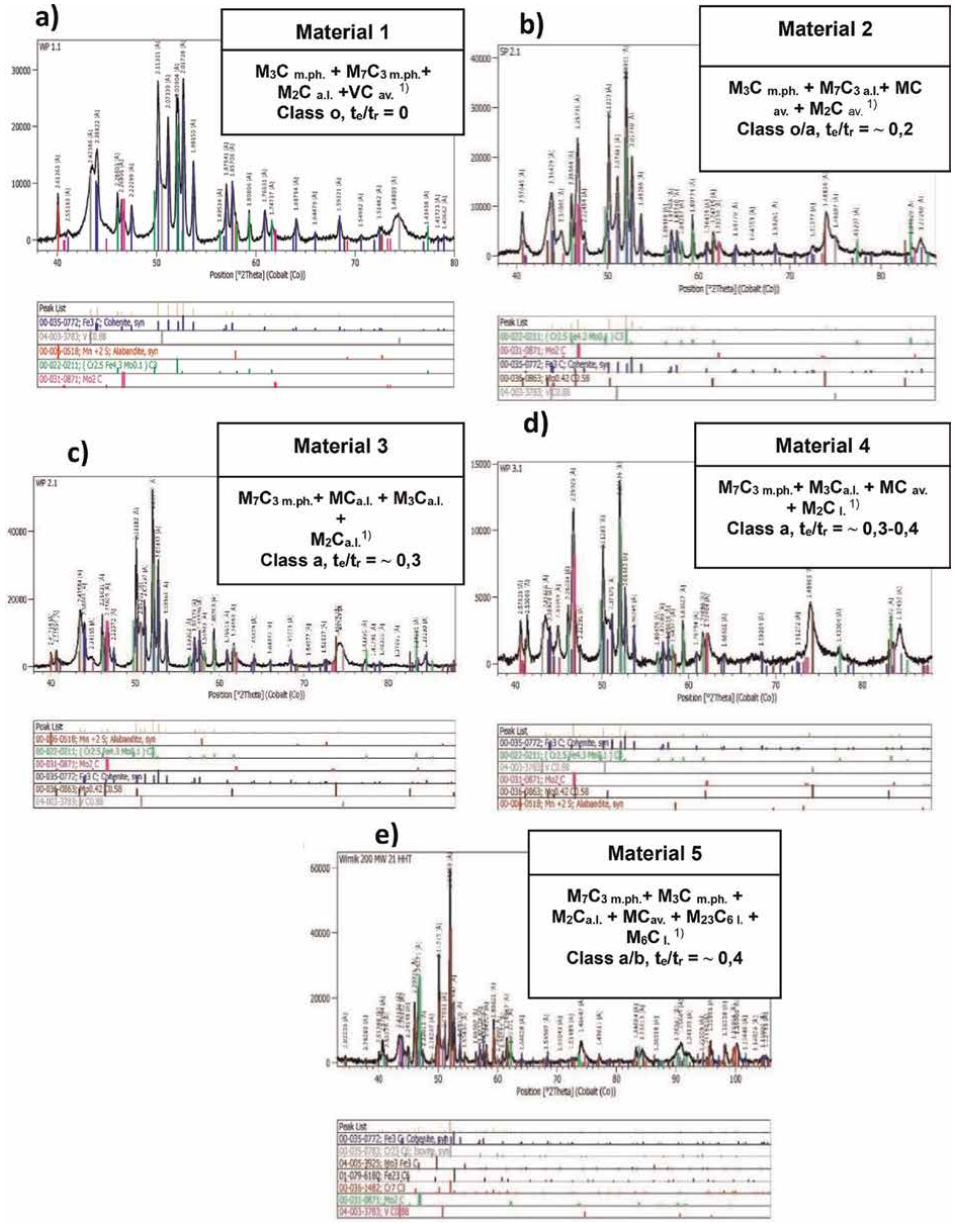

Figure 7.
X-ray diffractograms of material precipitate isolates of tested material sections from steam turbine rotors with the phase composition of precipitates and the estimated class of development of carbide precipitation processes in low-alloy Cr-Mo-V steel (21HMF) after long-term operation above the limit temperature, significantly beyond the design working time. Comments: [1)] M.ph.-main phase, l.-little, a.l.-a lot, v.l.-very little, av.-at an average.

On this basis, the class of the degree of development of the precipitation processes for the tested materials from the turbine shafts after long-term operation, and the corresponding degree of exhaustion were determined in accordance with Łukasiewicz-GIT (Łukasiewicz Research Network – Upper Silesian Institute of Technology) own classification, which is summarised in **Table 3**.

Tested material	Identified phase components and their relative content	Class of the degree of development of precipitates Exhaustion degree te/tr
1	2	3
Material 1	**M_3C– main phase** **M_7C_3 – main phase** M_2C – a lot VC– average	Class: o 0
Material 2	**M_3C– main phase** **M_7C_3 – main phase** M_2C – average MC – average	Class: o/a approx. 0.2
Material 3	**M_7C_3 – main phase** M_3C – a lot M_2C – a lot MC – a lot	Class: a approx. 0.3
Material 4	**M_7C_3 – main phase** M_3C – a lot MC – average M_2C – little	Class: a approx. 0.3–0.4
Material 5	**M_7C_3 – main phase** **M_3C – main phase** M_2C – a lot MC – average $M_{23}C_6$ – little M_6C – little	Class: a/b approx. 0.4

Table 3.
Results of X-ray phase analysis of deposits of electrolytically isolated precipitates of tested materials of steam turbine rotors made of low-alloy Cr-Mo-V (21HMF) steel after operation significantly beyond the unit's design operating time.

The class of development of carbide precipitation processes corresponds to their sequence revealed in X-ray examinations of isolated precipitates. The state of development of precipitation processes corresponds to:

- material No. 1 class o and degree of exhaustion $t_e/t_r = \sim 0$,
- material No. 2 class o/a and degree of exhaustion $t_e/t_r = \sim 0.2$,
- material No. 3 class a and degree of exhaustion $t_e/t_r = \sim 0.3$,
- material No. 4 class a and degree of exhaustion $t_e/t_r = \sim 0.3–0.4$,
- material No. 5 class a/b and degree of exhaustion $t_e/t_r = \sim 0.4$,

which confirms the existence of a diverse structure with varying degrees of exhaustion.

The predicted sequence of precipitates as a result of the creep process of the tested low-alloy Cr-Mo-V (21HMF) steels based on previous test results is [10]:

$M_3C_{\text{m.ph.}} + VC_{\text{av.}} + M_2C_{\text{av.}} \rightarrow M_{23}C_{6\ \text{m.ph.}} + M_2C + M_3C + VC \rightarrow M_6C_{\text{m.ph.}} + M_7C_{3\ \text{av.}} + M_{23}C_{6\ \text{av.}} + M_2C + VC \rightarrow M_6C_{\text{m.ph.}} + M_{23}C_6 + M_2C + VC.$

In assessing the degree of development of precipitation processes, the results of chemical composition tests from selected micro-areas, including precipitates, and maps of distribution and concentration of selected components were also used. A map of precipitates together with the results of the X-ray analysis of the chemical composition of micro-areas and an image of the microstructure obtained using a scanning electron microscope for material No. 5 is shown in **Figure 5**.

5. Examination of mechanical properties

The examination of strength properties, that is, tensile strength Rm, yield strength Re at room temperature, yield strength Ret at three temperature levels, that is. 300, 450 and 500°C, and elongation A_5 and reduction of area Z were carried out at room temperature RT and at elevated temperature as above. The obtained results of examining the materials of the sections of the high-pressure and medium-pressure parts of the turbine shaft are shown in **Figures 8** and **9**.

The obtained results show that with an increase in the degree of structure degradation measured by its class and an increase in the corresponding degree of exhaustion, the strength properties decrease. Tensile strength and yield strength at room temperature are higher than the minimum required values for turbine rotor shaft forgings made of the tested low-alloy Cr-Mo-V steel (21HMF) for a material with a structure characteristic of the initial state and a material with a low degree of exhaustion (t_e/t_r = ~ 0.2). For the tested materials with a higher class of structure and a higher degree of exhaustion (t_e/t_r = > 0.2 to 0.4), these properties are clearly reduced, and the actual values of yield strength at an elevated temperature are lower than the minimum required for the initial state (**Figure 8**). The elongation values obtained in the tensile test carried out at room temperature, regardless of the structure class and the corresponding exhaustion degree (t_e/t_r = 0–0.4), meet the minimum requirements at room temperature for turbine shaft forgings made of the tested steel in the initial state. Elongation at elevated temperature and reduction of area at room and elevated temperature, regardless of the structure class and degree of exhaustion, are at a sufficiently high level.

To determine impact energy at room temperature, impact tests were performed on samples with a V notch. The results of these tests for the tested materials made of low-alloy Cr-Mo-V (21HMF) steel after long-term operation with different structure class and corresponding degree of exhaustion (materials No. 2–4) regarding the typical structure of the initial state (material No. 1) is presented graphically in **Figure 10**.

The results of impact tests at room temperature of material No. 1 with a structure characteristic of the initial state (t_e/t_r = 0) and material No. 2 with minor changes in structure (t_e/t_r = ~ 0.2) meet the requirements for the initial state as and the expected minimum impact energy of 27 J. With an increase in the structure class and an increase in the degree of exhaustion (materials No. 3–5), the value of impact energy decreases and the tested materials do not meet the minimum requirements for the initial state at room temperature and are below the minimum expected value of 27 J. Also, the determined fracture appearance transition temperature ($FATT_{50}$) for the tested materials increases with the level of structure degradation measured by the structure class and the corresponding degree of exhaustion. Only for the material corresponding to the initial state (material No. 1) is the brittle transition temperature negative (−15°C). For the remaining materials it is positive, which is an unfavourable feature of the tested materials and increases from +5°C for material No. 2 (t_e/t_r = ~ 0.2) to +70°C for material No. 5 (t_e/t_r = ~0.4).

6. Fractographic examination

The fractography of fractures obtained on fractured impact samples for selected test temperature levels observed using a scanning electron microscope for a selected representative example, that is, material No. 5 with structure class 2/3, exhaustion degree t_e/

DOI: http://dx.doi.org/10.5772/intechopen.111892

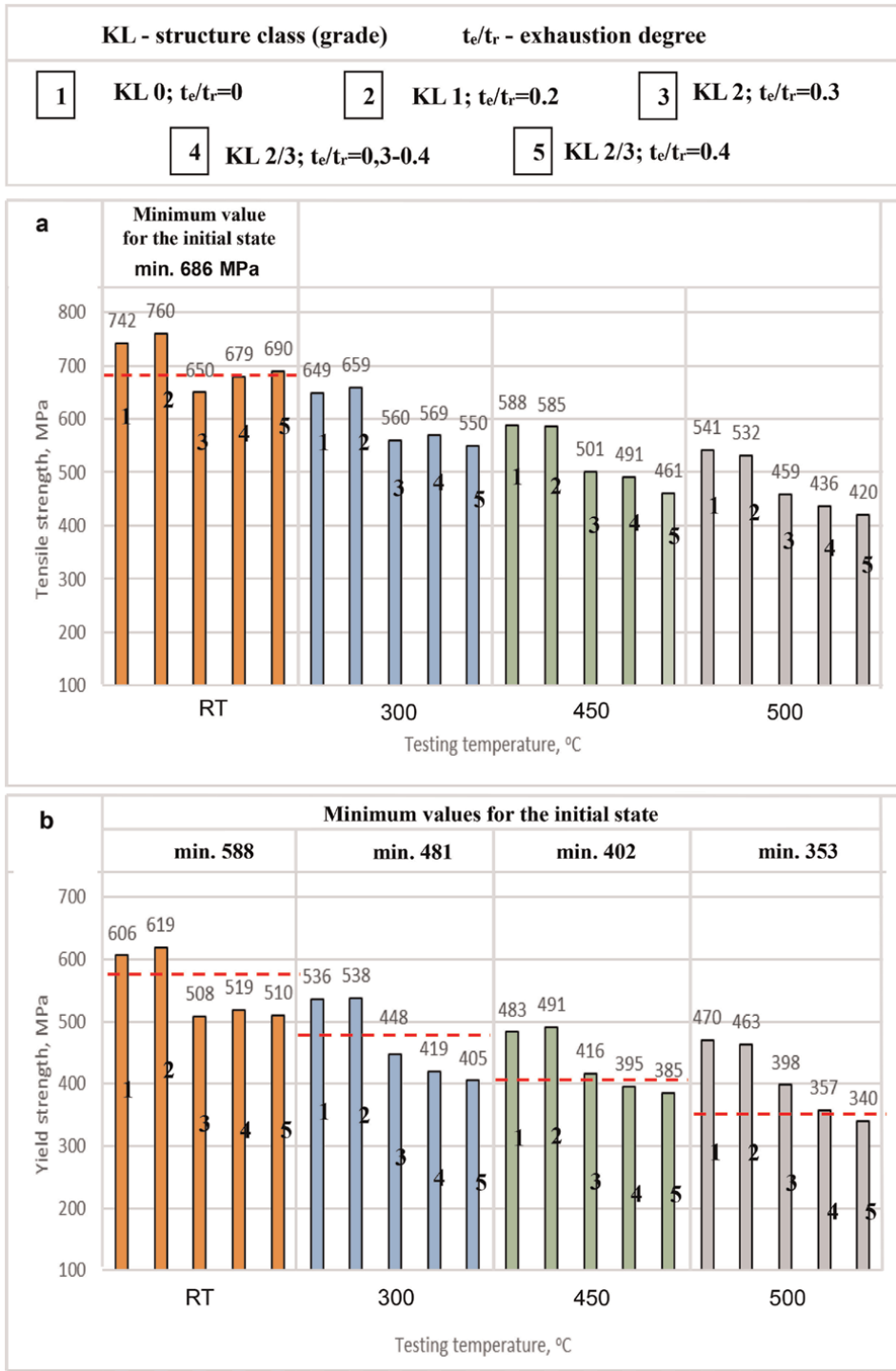

Figure 8.
Tensile strength (a) and yield strength (b) at room and elevated temperatures of turbine rotor materials after long-term operation of various structure classes and the corresponding degree of exhaustion in relation to the initial state.

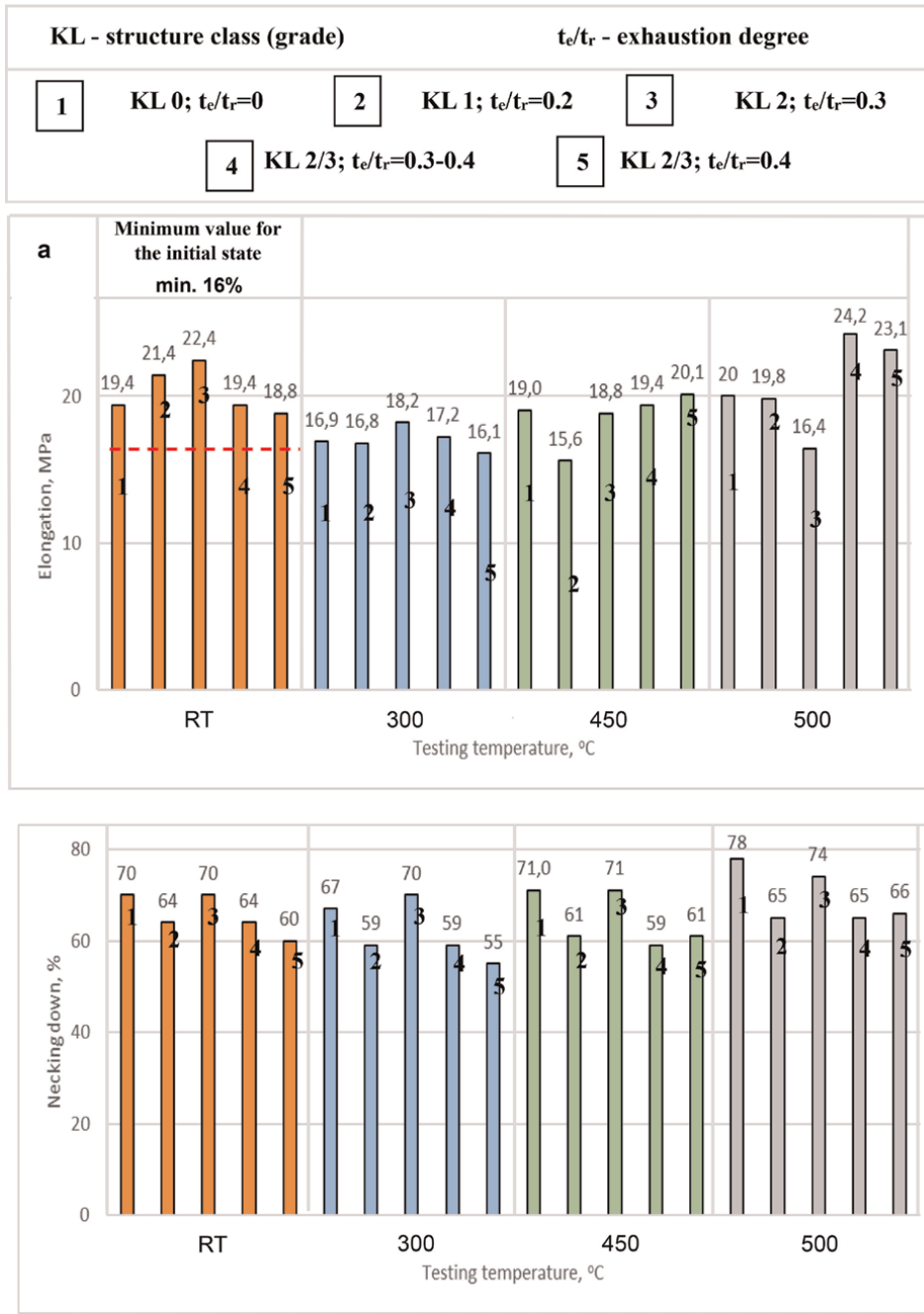

Figure 9.
Elongation (a) and reduction of area (b) in a tensile test at room and elevated temperatures of turbine rotor materials after long-term operation of various structure classes and the corresponding degree of exhaustion in relation to the initial state.

t_r = ~ 0.4) and fracture appearance transition temperature $FATT_{50}$ = ~ +70°C, are shown in **Figure 11**. **Figure 11a** shows the images of the fracture of the impact sample fractured at room temperature (RT) with the obtained value of impact energy of 9 J. **Figure 11b**

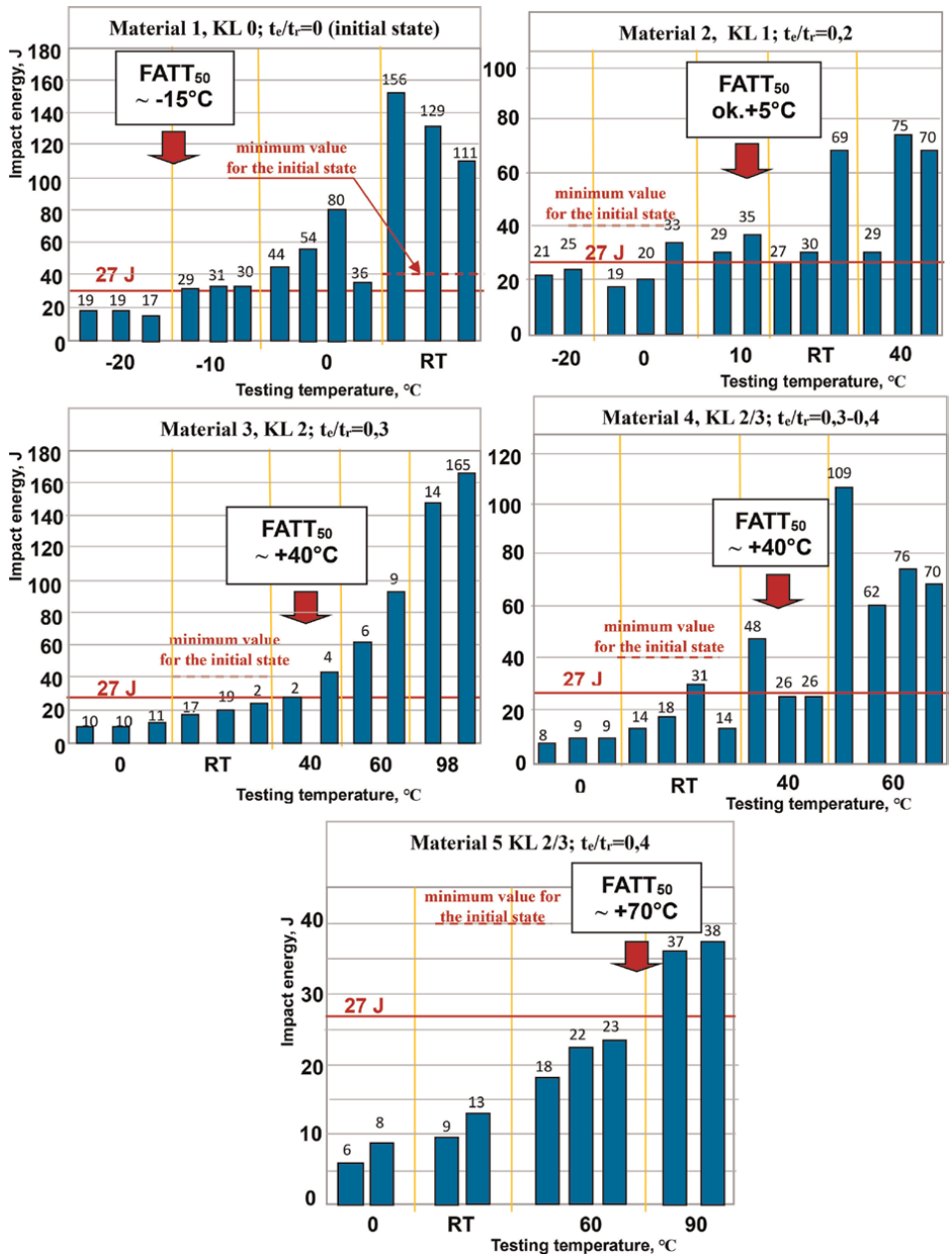

Figure 10.
Impact energy depends on the test temperature and fracture appearance transition temperature ($FATT_{50}$) of steam turbine rotor materials made of Cr-Mo-V (21HMF) steel after long-term operation with different structure class and corresponding degree of exhaustion in relation to the initial state.

shows the images of the fracture of the impact sample obtained at the temperature of +90°C with the impact energy value of 38 J. At room temperature, a brittle fracture with small enclaves of a ductile fracture was obtained, while at the temperature of +90°C a mixed fracture with a predominance of a brittle fracture was obtained.

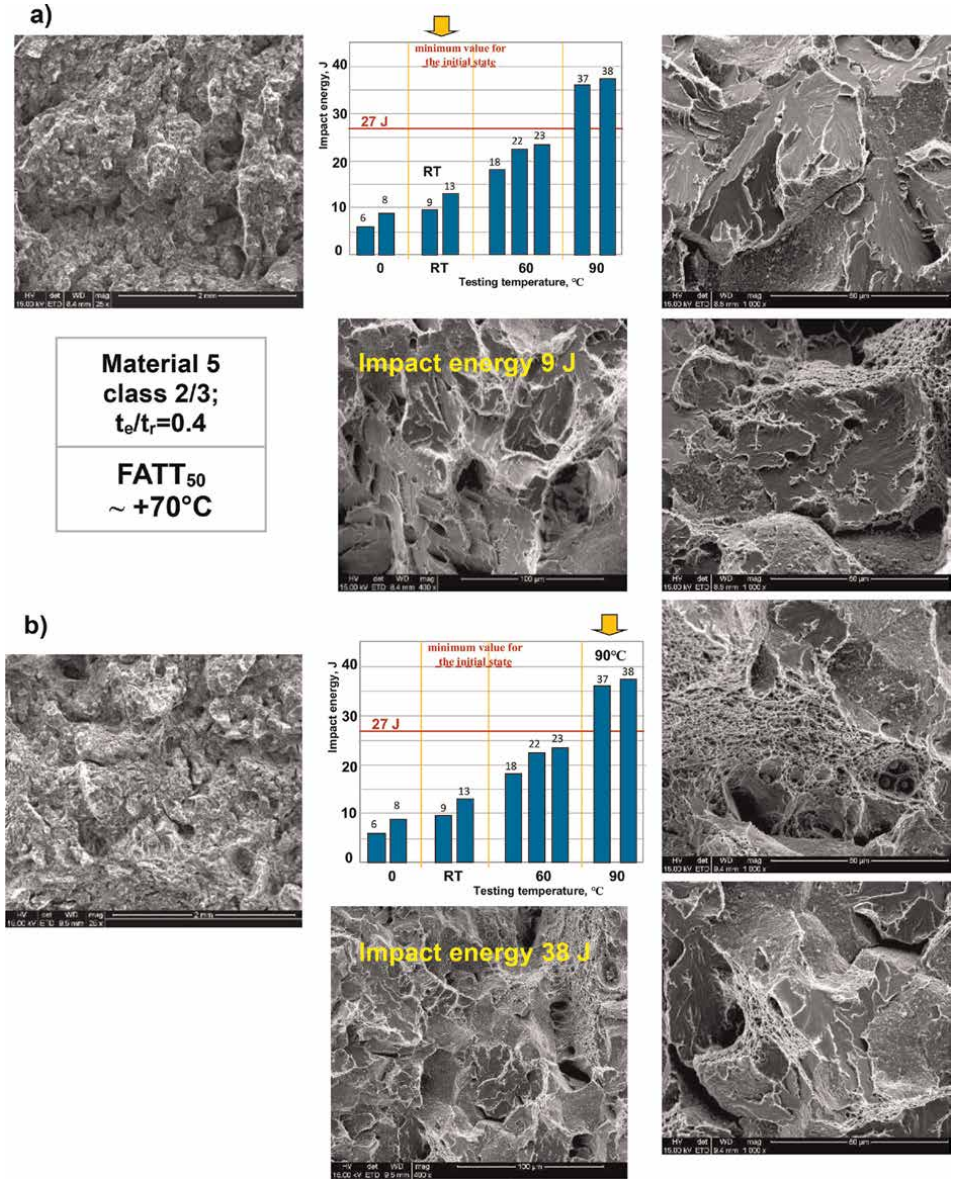

Figure 11.
Fractographic images of impact samples of the steam turbine rotor material made of Cr-Mo-V (21HMF) steel after long-term operation: a) fractured at room temperature, b) fractured at +90°C.

7. Creep strength

7.1 Short-term creep tests

Short-term creep tests in accordance with the developed own procedure [1, 3] were used to determine the residual life and available residual life. Residual life ter is the time to destruction as a result of material creep after operation for the assumed parameters of further operation. On the other hand, available residual life is a part of

residual life and the time up to the end of the second stage of creep teb, which is also a safe time for further operation for defined temperature and stress parameters.

The applied method of shortening the duration of the creep tests until fracture consists in accelerating the creep process by increasing the test temperature T_b significantly above the values appropriate for operation, but carried out at a constant test stress corresponding to the operational stress $\sigma_b = \sigma_e$ = constant. Short-term creep tests were performed at constant test stress σb corresponding to operational stress σe, ($\sigma_b = \sigma_{be}$ = constant) and at a constant test temperature Tb for each test, but with different values. For each of the materials with a different degree of structure degradation, tests were carried out at several test temperature levels. They were carried out at a constant stress level σ_{b1} = 60 MPa and σ_{b2} = 70 MPa and at several levels of test temperature Tb in the range from 600 to 700°C.

The test results are presented in **Figure 12** in the form of the dependence of the time to rupture ter on the test temperature T_b at a constant stress level corresponding to operational stress $\sigma_b = \sigma_e$ [log $t_r = f(T_b)$ at σ_b = constant]. This enabled drawing a line inclined to the time axis until the destruction of ter. Residual life ter was determined by extrapolating the obtained straight line toward the lower temperature corresponding to operational temperature T_e. The figures show the determined residual life ter and the residual available life teb. The available residual life was determined in accordance with the procedure in accordance with [1, 3].

Residual life and residual available life decrease with the increase of the structure class and the corresponding exhaustion degree. For example, residual life ter for a material with a structure characteristic of the initial state (class 0) and at the stress level $\sigma_b = \sigma_e$ = 60 MPa for the operating temperature Ter = 530°C is 650,0000 h, for a material after operation with a structure corresponding to class 2 and the degree of exhaustion t_e/t_r = 0.3 is 480,000 h and the material after use with a structure corresponding to class 2/3 and the degree of exhaustion t_e/t_r = 0.3–0.4 is 380,000 h.

Residual life for these operating parameters decreases respectively from 390,000 h for the material with the initial state structure through 288,000 h for the material with structure class 2 and t_e/t_r = 0.3 to 228,000 h for material with structure class 2/3 and t_e/t_r = 0.3–0.4.

7.2 Creep rate

Creep tests with measurement of elongation during the test were carried out at a constant test temperature T_b and for test stress level σb with a constant value and duration over 2000 hours. The fragments of the creep curves obtained in these tests with a sufficiently long section of these curves in the steady state, that is. in the second creep period in the form of the dependence of the permanent deformation ε on the creep time t, allowed to determine the steady-state creep rate $\dot{\varepsilon}_s$. Using the obtained creep curve in the form of the dependence of the value of permanent deformation A_f on the creep time [$(A_f = f(t)$] at constant test temperature T_b and test stress σb corresponding to the operational stress ($T_b = T_e$, $\sigma_b = \sigma_e$), the set creep rate $\dot{\varepsilon}_s$ was determined, and from it the maximum time of safe operation teb for the assumed permissible value of permanent deformation as a result of creep. A comparison of creep curves in the form of relationship $A_f = f(t)$ w at a constant temperature T_b and constant stress σb corresponding to the operational material of turbine rotors made of Cr-Mo-V (21HMF) steel with a different, previously defined class of structure and the corresponding degree of exhaustion after operation is shown in **Figure 13**.

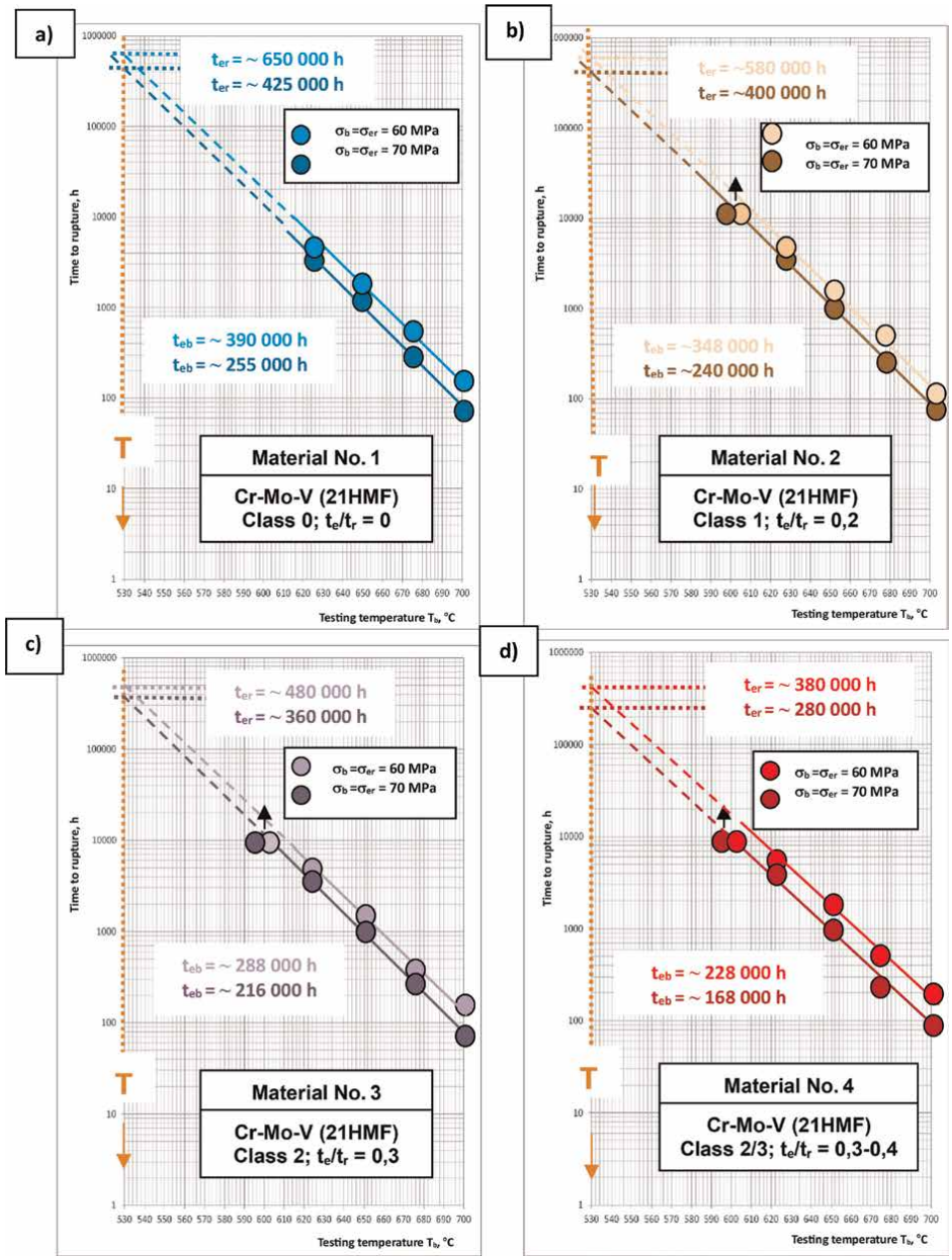

Figure 12.
Results of short-term creep tests in the form of log $t_r = f(T_b)$ at σ_b = constant at test temperature T_b higher than the operating temperature T_e ($T_b > T_e$) and the determined residual life ter for the operating temperature of the material of the turbine rotor components made of low-alloy steel Cr-Mo-V (21HMF) depending on the structure class and the corresponding exhaustion degree.

Determined in this way, available residual life teb at Tb = 530°C and at the stress σb = 60 MPa for the material with a structure corresponding to the initial state and class 0; (material No. 1) is 600,000 h, for material with structure class 1 (material No. 2) it is 288,000 h and for material with structure class 2/3 (material No. 4) it is 228,000 h. An increase in the structure class and the corresponding exhaustion degree

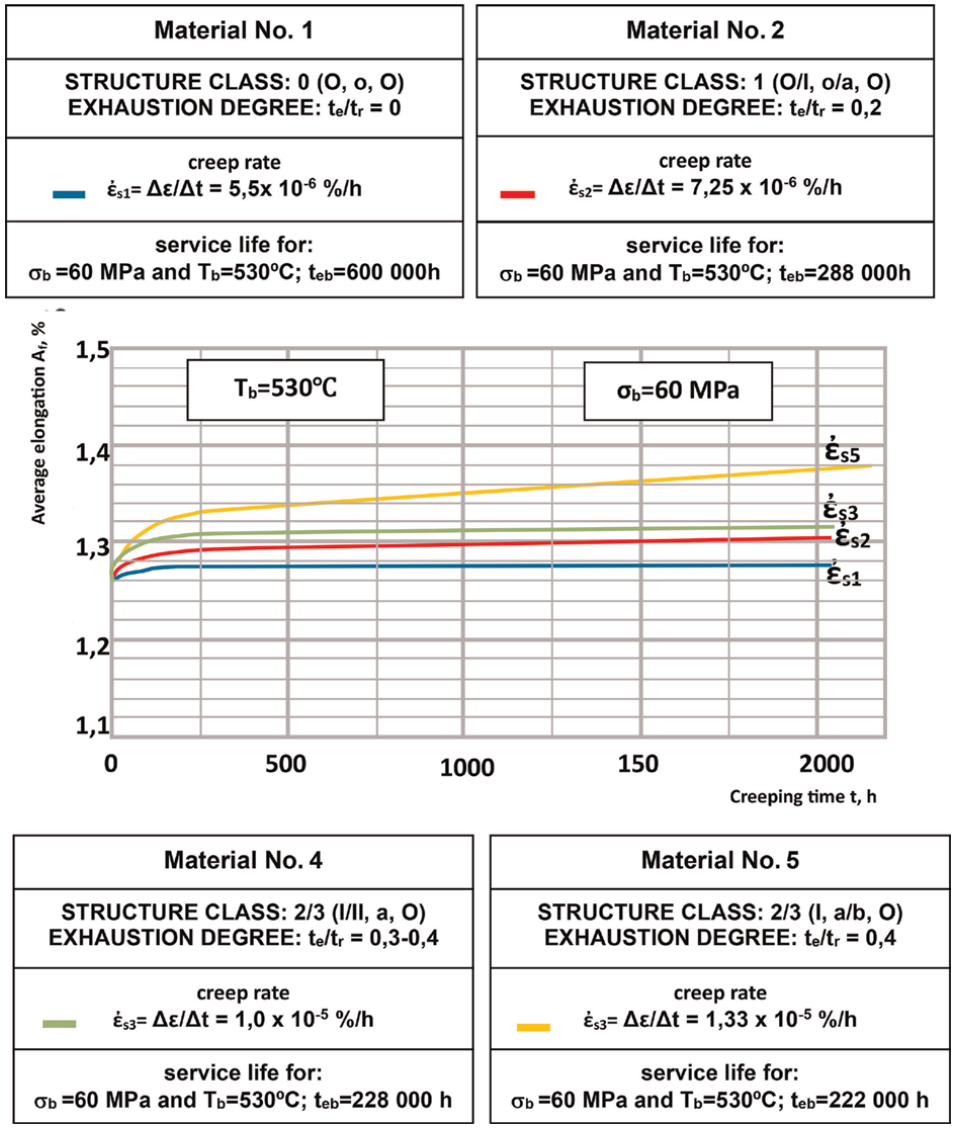

Figure 13.
Comparison of creep curves in the form of dependence $A_f = f(t)$ at a constant temperature T_b and constant stress σ_b corresponding to the operating material of turbine rotors made of low-alloy Cr-Mo-V (21HMF) steel with different structure class and corresponding exhaustion degree.

for the same temperature and stress parameters results in a higher creep rate ės, resulting in shortening of residual available life teb.

8. Conclusions

1. Changes in the structure of the tested low-alloy Cr-Mo-V steel caused by long-term operation in creep conditions are the result of, on the one hand, the 'decomposition' of bainite, and on the other hand, the result of the development of precipitation processes related to the reduction or even disappearance of

some, the formation of other precipitates, their coagulation and coalescence, often associated with other less favourable sites.

2. Differences in the microstructure of materials after long-term operation in relation to the microstructure of the typical initial state of the tested low-alloy ternary Cr-Mo-V steel are bainite degradation and development of the precipitation process inside its areas and development of precipitation processes on the borders and inside ferrite grains, without discontinuities and microcracks and without initiating internal creep failure processes. Their assessment was made based on the prepared classification of the state of the structure in relation to the estimated degree of exhaustion based on the above-mentioned components of its degradation processes.

3. The observed carbide sequences of the tested materials, based on X-ray diffraction analysis of electrolytically isolated carbide deposits, confirm the state of the microstructure estimated based on the analysis of its images observed using a scanning electron microscope.

4. Changes in the structure and its state defined by the class and the corresponding degree of exhaustion results in a decrease in hardness and strength properties, as well as in the impact energy to values lower than the minimum required for the initial state and shifting the fracture appearance transition temperature to a positive temperature, which reduces the ability of the tested materials to carry the required operating loads.

5. Creep strength measured by residual life and available residual life, which is service life and the time of further safe operation, for temperature and stress parameters of further operation based on short-term tests, decreases as the structure class and the corresponding estimated degree of exhaustion increase.

6. Creep strength measured by the residual available life, which is the service life and the time of further safe operation, for the temperature and stress parameters of further operation based on creep tests with the measurement of elongation during the test, decreases with the increase of the structure class and the corresponding estimated degree of exhaustion.

7. The significantly lower values of residual available life obtained on the basis of creep tests with measurement of elongation than those obtained on the basis of short-term tests result from the assumed limit value of permanent deformation as a result of creep, which does not correspond to the end of the second creep period as determined on the basis of short-term creep tests and is reached much before the end of the second stage of creep.

8. The developed characteristics of turbine rotor materials made of low-alloy ternary Cr-Mo-V steel after operation enable the assessment of the condition and estimation of the time of further safe operation using the non-destructive method of matrix and extraction replicas collected directly on the item and are used in industrial practice.

9. The tests carried out do not exhaust the area of necessary characteristics of the material of turbine rotors made of the tested low-alloy ternary Cr-Mo-V steel in

the assessment of the condition after long-term operation. In the case of the tested materials, it is necessary to test the impact of shutdowns and start-ups on reducing the residual life on the basis of fatigue tests and cyclic creep tests and to assess the state of development of precipitation processes by revealing the places of occurrence of individual types of carbides in the microstructure based on TEM tests. These studies are in progress and their results will be presented in later publications.

Author details

Joanna Furmanek* and Janusz Dobrzański
Łukasiewicz Research Network — Upper Silesian Institute of Technology, Gliwice, Poland

*Address all correspondence to: joanna.furmanek@git.lukasiewicz.gov.pl

References

[1] Dobrzański J. Materials science interpretation of the life of steels for power plants. Open Access Library. 2011;**3**:1-8

[2] Hernas A, Dobrzański J. Life-Time and Damage of boiler's and turbine's Components. Gliwice: The Silesian Technical University publishing house; 2003

[3] Dobrzański J. Durability of Pressure Components of Power Units. Gliwice: The Institute for Ferrous Metalurgy publishing house; 2019

[4] Dobrzański J. The procedure for determining the time of safe service beyond the design service time based on creep testing. Chapter 5. In: Creep Characteristics of Engineering Materials. London UK: Intech Open; 2019. pp. 49-68

[5] Dobrzański J, Hernas A, Moskal G. Microstructural degradation in power plant steels, chapter No. 9. In: Oakey JE, editor. Power Plant Life Management and Performance Improvement. Sawston, UK: Woodhead Publishing Series in Energy: Number 23; Oxford Cambridge, Philadelphia, New Delhi: Woodhead Publishing Limited; 2011

[6] Dobrzański J, Purzyńska H, Matusik M. Material tests in the assessment of condition and forecasting about further safe service of steam turbine rotors beyond the design service life. Energy. 2015;**11**:761-764

[7] Dobrzański J, Zieliński A. Material diagnostics of components in the pressure part of steam boilers and pipelines operating under creep conditions much beyond the designed service life. Energy. 2016;**4**:229-233

[8] Dobrzański J, Purzyńska H. Method to assess the condition of material of power units turbine rotors after a long operation in creep conditions beyond the design service life. Energy. 2019;**11**: 745-750

[9] Zieliński A. Service Life of Creep-Resistant Steels with Ferritic Matrix under Long-Term Temperature Influence (in Polish). Gliwice: Institute for Ferrous Metalurgy publishing house; 2016

[10] Furmanek J, Dobrzański J. Structure and mechanical properties of 21HMF steel steam turbine rotor materials after long-term operation for a time significantly exceeding the disign time. Journal of Metallic Materials. 2021;**73**(2): 40-55

[11] Joarder A, Sarma DS, Cheruvu NS. Effect of long-term service exposure on microstructure and mechanical properties of a CrMoV steam turbine rotor steel. Metallurgical and Materials Transactions A: Physical Metallurgy and Materials Science. 1991;**22**:1811-1820. DOI: 10.1007/BF02646505

[12] Dong J, He Y, Song G, Jung J, Shin K. Evolution of carbide morphology and composition in Cr–Mo–V steel after service exposure. Materials Technology. 2012;**27**(1):70-72. DOI: 10.1179/175355511X13240279340048

[13] Sun Q, Li X, Li K, Cai Z, Han C, Li S, et al. Effects of long-term service on microstructure and impact toughness of theWeld metal and heat-affected zone in CrMoV steel joints. Metals. 2022;**12**:278. DOI: 10.3390/met12020278

Chapter 5

Corrosion Protection of 316L SS by Cerium-Based Coatings: Effect of the Incorporation of Additives

Nadia C. Cortes, Ana P. Loperena, Lorena I. Brugnoni, María Belén González and Ivana L. Lehr

Abstract

Interest in cerium-based coatings has increased in recent years due to their low toxicity, biocompatibility, and improved corrosion protection performance. The formation of a coating from a solution containing cerium nitrate ($Ce(NO_3)_3$) has been investigated as a good surface modification strategy for the production of protective coatings on 316L SS. The effect of various additives in the treatment solution (sodium molybdate, sodium salicylate, and ascorbic acid) on the corrosion protection properties of the coatings was evaluated. The protection performance of the coated samples in a physiological simulated fluid (Ringer solution) was examined by electrochemical methods. The composition and morphology of all coatings were analyzed by scanning electron microscopy (SEM) and energy dispersive spectroscopy (EDX).

Keywords: 316L stainless steel, corrosion protection, cerium, molybdate, salicylate, ascorbic acid

1. Introduction

In recent years, 316L stainless steel (316L SS) has been widely used for different applications in various fields because of its good corrosion resistance. Its biocompatibility, high corrosion resistance, and mechanical properties make it an excellent alternative for biomedical applications [1, 2]. Nevertheless, this material suffers pitting corrosion in aqueous solutions, which limits its potential applications [1, 2].

The release of unwanted ions in the surroundings of the 316L SS implant causes problems that are usually difficult to treat, leading to an early implant failure and inducing a risk for the living tissues [3, 4]. In addition, stainless steel is susceptible to bacterial growth under physiological conditions, which is another severe cause of implant failure [5]. In order to avoid this type of degradation, the use of protective coatings is a promising alternative. Several electrochemical methods were employed for the formation of protective coatings. Among these, the conversion treatment is distinguish for its cost-effective use and easy operation [3]. These coatings act as a barrier between the substrate and the corrosive environment [4].

In order to enhance the corrosion resistance of stainless steel in chloride containing media, cerium-based coatings have been investigated [6]. Cerium oxides have been extensively studied for biomedical applications due to their low toxicity, corrosion inhibition, and self-healing properties [7, 8]. The improvement in the corrosion resistance is attributed to the role of Ce^{+4} and Ce^{+3} ions within the film, which have the ability to supply oxygen and promote the formation of the passive layer on the SS surface. In addition, self-healing ability of cerium films is activated when the local pH is sufficiently high [9]. Cerium oxides and hydroxides are deposited on the substrate surface as a result of local pH increase, thereby preventing the spread of corrosion [9].

Salicylates have been reported to have important biological and pharmacological beneficial properties for human health. They are one of the oldest and most widely used anti-inflammatory drugs and also exhibit various recognized pharmacological roles such as anticancer, neuroprotective, antipyretic, skin antiaging, and antidiabetic effects [10]. It was reported that the presence of sodium salicylate in a polypyrrole coating improves the corrosion protection of 316L SS, promoting the formation of the passive layer on the surface of substrate [11, 12]. Moreover, it has been informed a favorable *in vivo* vascular compatibility of a salicylate-based polymer coating employed as a drug-eluting for metallic stents [13].

On the other hand, molybdate anion has many advantages, such as low toxicity and high stability in aqueous media [14, 15]. Particularly, molybdate was also used extensively as a corrosion inhibitor of iron and stainless steels over a wide-ranging temperature and pH [16, 17]. The anion positively affects the passivity breakdown and pitting initiation of 316L SS. Moreover, it has been reported that the use of molybdate as dopant in the polypyrrole electrodeposition on 316L SS results in the formation of coatings with good anticorrosive properties [18]. The improvement in the corrosion resistance is associated with the presence of molybdenum species in the obtained film.

Ascorbic acid (HAsc) has been extensively studied for steel in acid and neutral media due to its inhibitor character [19–21]. The formation of an oxide film with protective properties on steel is attributed to the deposition of insoluble chelates on the substrate surface that occurs at an optimal concentration of 10^{-3} M [21]. Nevertheless, the authors also reported that concentrations higher than 5×10^{-3} M lead to the formation of soluble chelates that promotes Fe dissolution. In addition, the HAsc showed a dual behavior. Depending on the conditions, it can behave as a corrosion inhibitor or it can promote the corrosion of stainless-steel (SS)X4Cr13 in HCl solutions [22].

The presence of cerium-based coatings on steel surfaces has been previously demonstrated as a major advance in the engineering field. Recently, Hayajneh et al. have presented the results of improving the corrosion behavior of 316L SS by developing a thin cerium oxide gelatin nanolaminate coating. The results confirmed the formation of homogeneous and crack-free coatings without any apparent defects. The prepared films significantly improved the corrosion resistance of 316L SS in a simulated marine environment [6]. Pitting corrosion of 304 SS in an alkaline 3.5% NaCl solution was significantly improved by a chemical cerium conversion coating. The results showed that both the Ecorr and Epit values of 304 SS could be greatly increased by the coating [23]. In addition, some recent work related to biomedical engineering can be mentioned. Abdulaah et al. applied a cerium tricalcium phosphate (CTP) coating on the surface of 316L SS using the high-frequency sputtering technique. They investigated the corrosion protection performance in a simulated body fluid, and the experimental results showed that the CTP coating improved the corrosion resistance in a simulated body fluid with a protective efficiency of 91% [24].

Critical issues in implant surgery are bacterial infections. In order to prevent infections, the implant surfaces could be an effective alternative to avoid the adhesion and growth of bacteria [25]. Hence, the development of coatings with antibacterial activity has recently attracted significant attention. Silver nanoparticles (AgNps) are well-known as a wide-spectrum antibacterial agents. Stable and long-term antibacterial activity shows the AgNps without affected by drug resistance [26]. The antibacterial mechanism of Ag is not fully understood; however, it is known that silver ions are the ones that interact with bacteria cell walls, resulting in bacterial death [27].

The aim of this study is the formation of a biocompatible, anticorrosive, and antibacterial film on 316L SS in order to functionalize the substrate for stent applications. Thus, the coatings were formed in a solution containing cerium nitrate and hydrogen peroxide on 316L SS by a potentiostatic technique. The influence of the presence of additives as sodium salicylate, sodium molybdate, and ascorbic acid in the treatment solution and employed technique on the properties of the coatings was evaluated. Films were characterized using electrochemical techniques and SEM/EDX. In order to compare, the corrosive behavior was also evaluated for the different films and the bare 316L SS.

2. Corrosion inhibition study of 316L SS in presence of additives

The working electrodes used for *all measurements presented in this chapter* were prepared from 316L SS sheets (wt. % is 17.47 Cr, 10.32 Ni, 1.88 Mn, 1.90 Mo, 0.39 Si, 0.025 C, and Fe balance). For studies of the corrosion performance and morphological and compositional characterization, the exposed surface area was of 0.07 cm^2, while for antibacterial evaluation, the sections were 0.25 cm^2. Before each experiment, SiC paper grit 1200 was employed to prepare the 316L SS electrode surface; then, it was degreased with acetone and washed with triply distilled water. The electrochemical experiments were done in a 20 cm^3 Metrohm cell using a conventional three-electrode system. The reference electrode was a commercially available Ag/AgCl/3M KCl electrode (Metrohm), and a Pt sheet was employed as the counter electrode.

To increase the anticorrosive performance of the cerium-based film formed in combination with H_2O_2, the addition of different compounds was studied. The procedure used to evaluate the effect of the additives in the cerium treatment was similar to that reported by us for AZ91D Mg alloy [28].

Thereby, the inhibition effect of sodium salicylate (NaSa), sodium molybdate (Na_2MoO_4), and ascorbic acid (HAsc) on the electrochemical behavior of bare 316L SS in Ringer solution was evaluated. In order to establish the most favorable conditions for cerium-based coating generation, different concentrations of each additive were analyzed. Polarization curves of 316L SS in Ringer solutions containing different additive concentrations are presented in **Figures 1**–**3**. It can be observed that the corrosion rate of 316L SS is delayed by the presence of the NaSa for all concentrations evaluated (**Figure 1**). The best inhibition effect was obtained for 5 mM NaSa (**Figure 1**, curve c). In order to analyze the effect of presence of Na_2MoO_4 and ascorbic acid (HAsc), a similar procedure was carried out (**Figures 2** and **3**, respectively). The highest corrosion inhibition effect of Na_2MoO_4 was obtained for 15 mM (**Figure 2**, curve d), while for HAsc, the optimal concentration was 1 mM (**Figure 3**, curve b).

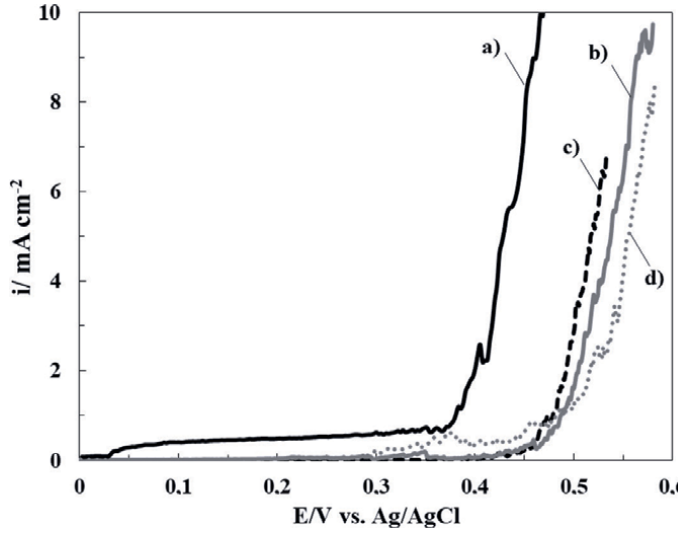

Figure 1.
Polarization curves obtained at scan rate of 0.001 Vs^{-1} for bare 316L SS alloy in ringer solution containing different NaSa concentrations: (a) 0 mM, (b) 1 mM, (c) 5 mM, and (d) 15 mM.

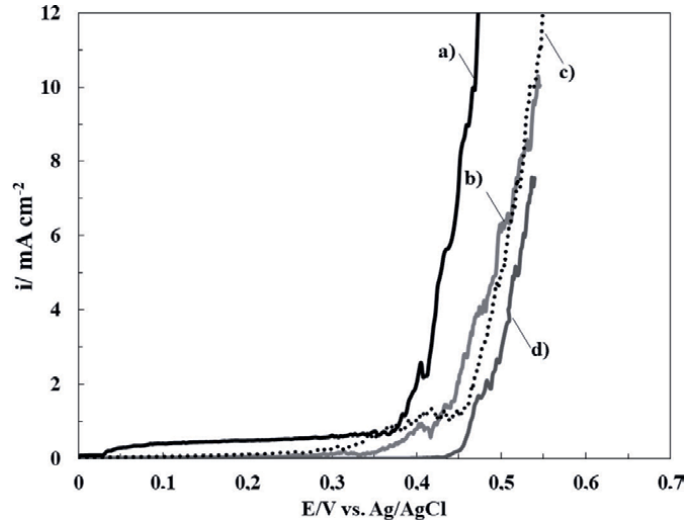

Figure 2.
Polarization curves obtained at scan rate of 0.001 Vs^{-1} for bare 316L SS alloy in ringer solution containing different Na_2MoO4 concentrations: (a) 0 mM, (b) 1 mM, (c) 5 mM, and (d) 15 mM.

It was reported that the NaSa is predominantly an anodic inhibitor [29]. In the case of molybdate was also used extensively as a corrosion inhibitor of iron and stainless steels over a wide-ranging temperature and pH range [11, 13]. The anion positively affects the passivity breakdown and pitting initiation of 316L SS.

It has been published that in acid and neutral media, the deposition of an insoluble chelate occurs at an optimal concentration of 10^{-3} M HAsc, allowing the formation of

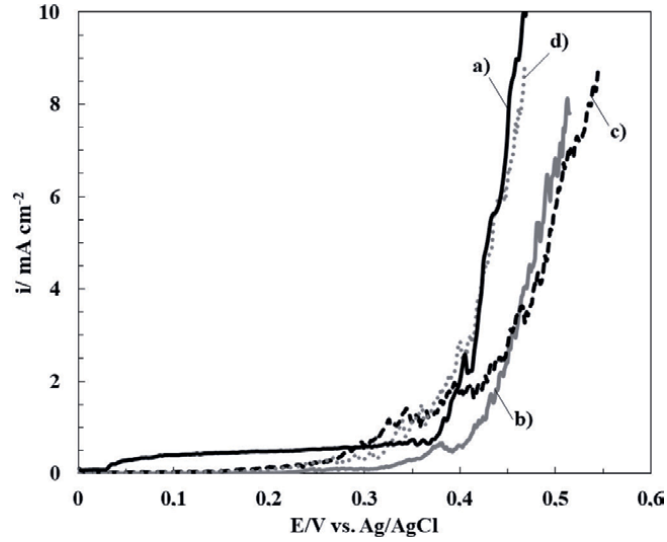

Figure 3.
Polarization curves obtained at scan rate of 0.001 Vs^{-1} for bare 316L SS alloy in ringer solution containing different HAsc concentrations: (a) 0 mM, (b) 1 mM, (c) 5 mM, and (d) 15 mM.

a protective oxide film on the steel surface [19–21]. According to our results, Fe dissolution is promoted at concentrations above 5×10^{-3} M. In addition, several works reported a dual role of HAsc; it can increase the dissolution rate of substrates or act as a corrosion inhibitor depending on the circumstances [22, 30].

As previously reported, the improved inhibition performance of RCeNaSa is due to a synergistic effect of this compound in which both components, which are inhibitors of 316L SS by themselves, are simultaneously incorporated into a surface coating, as shown by the above results. This is because the organic component (NaSa) is predominantly an anodic inhibitor [29], while the cerium (under these circumstances) proves to be predominantly a cathodic inhibitor [31].

For all the coatings studied, optimal conversion parameters such as additive concentrations, applied potential, and temperature were determined in order to obtain protective cerium coatings on 316L SS. Thus, the corrosion efficiency was evaluated for the electrodes treated in different cerium-based solutions by the potentiodynamic polarization tests in Ringer solution at 37°C. Firstly, cerium-based coating was formed onto the 316L SS. More protective film was electrosynthetized from an electrolyte solution containing 30 mM $Ce(NO_3)_3{\cdot}6H_2O$ and 25 mM H_2O_2 in a purified nitrogen gas saturated atmosphere. The applied potential applied was of - 0.7 V, and the temperature employed was 50°C. For simplicity purposes, this coating will be called RCe. The presence of hydrogen peroxide favors the oxidation of Ce^{3+} to Ce^{4+}, incorporating the cerium (IV) species in the film [32]. It has been reported that the presence of cerium (IV) results in a yellow-colored film [33], whereas the presence of cerium (III) is responsible for the white color [28, 30]. This film obtained will be identified in the text as RCe.

The optimal concentration of each additive for coating formation was established from the corrosion inhibition results shown above (**Figures 1–3**). Thus, the cerium-based coatings were formed in a solution containing 30 mM $Ce(NO_3)_3$, 25 mM H_2O_2, and:

- 5 mM NaSa at - 0.70. This film will be identified as RCeNaSa.
- 15 mM Na_2MoO_4 at - 1.00 V. This film will be called RCeMo.
- 1 mM HAsc at - 0.80 V. This film will be called RCeHAsc.

After 30 min of the conversion treatment at 50°C, a golden yellow-colored was observed with the naked eyes when the substrate for all coatings was obtained.

3. Morphological and compositional characterization of cerium-based coatings

Figures 4–6 show the SEM micrographs of RCeNaSa, RCeMo, and RCeHAsc films, respectively. For all coatings, the electrode surface is characterized by cracked-mud structure. A similar morphology was reported for cerium-based coatings [34]. The cracked morphology is associated with different causes: the generation of gas bubbles on the electrode surface during the coating formation, the dehydration process during coating drying, or the shearing stresses between the substrate surface and the coating [35].

The presence of Ce and Fe in the coatings was confirmed by EDX analysis. Also, the signal of additives incorporated in the coating as Mo and Na was distinguished in the EDX examination.

4. Evaluation of anticorrosive performance of the cerium-based films

Various experiments were performed to test the corrosion performance of the coatings. The OCP change with time was measured over 4 days (**Figure 7**). At first, the OCP value for bare steel sample stabilizes after the second day of immersion at a value around - 0.15 V. The samples covered with the different coatings show slightly more positive values than the uncoated substrate, suggesting a protective effect of

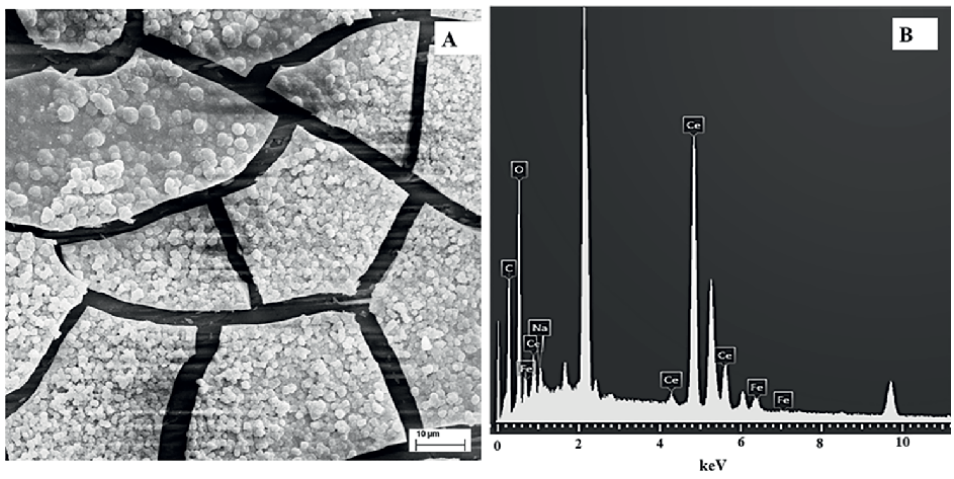

Figure 4.
SEM image (A) and EDX examination (B) of the 316L SS covered with RCeNaSa coating.

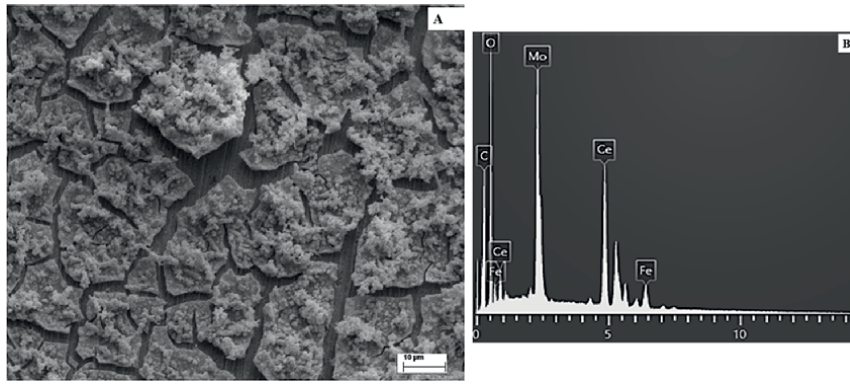

Figure 5.
SEM image (A) and EDX examination (B) of the 316L SS covered with RCeMo coating.

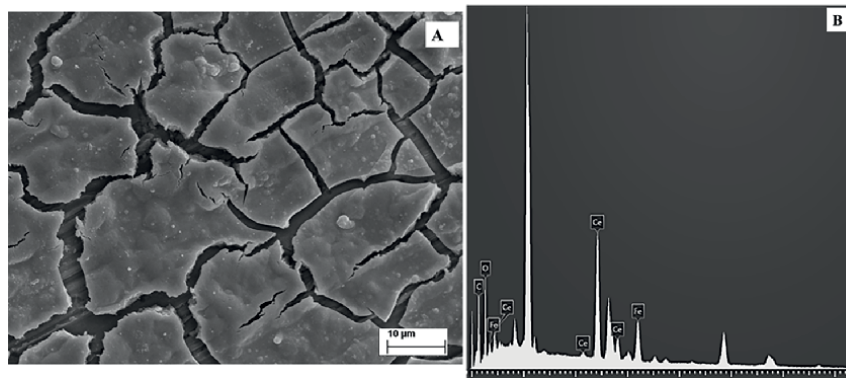

Figure 6.
SEM image (A) and EDX examination (B) of the 316L SS covered with RCeHAs coating.

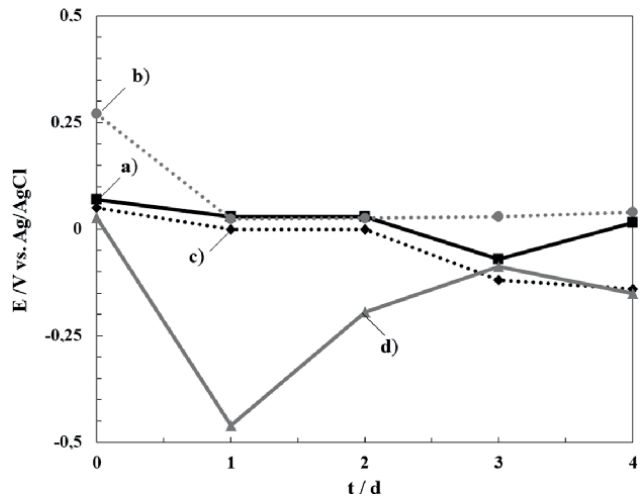

Figure 7.
Time dependence of OCP in ringer solution of 316L SS electrode covered by: (a) RCeNaSa coating, (b) RCeMo coating, and (c) RCeHAsc. The variation of bare steel electrode is also included (d).

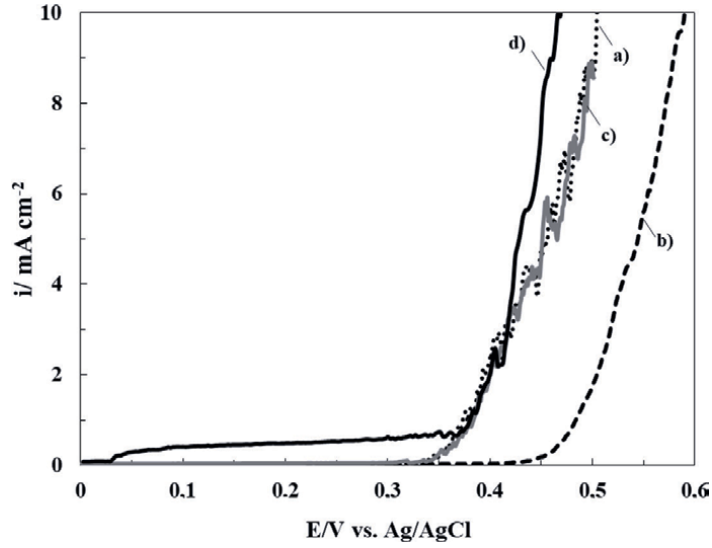

Figure 8.
Polarization behavior in ringer solution of 316L SS electrode covered with: (a) RCeNaSa coating, (b) RCeMo coating, and (c) RCeHAsc coating. The scan rate was 0.001 Vs^{-1}. The data of bare steel electrode is also included (d).

the coatings. These preliminary results show that all coatings improve the corrosion protection of the bare steel.

The improved corrosion resistance can also be evaluated by comparing the polarization curves in Ringer solution (**Figure 8**). The potentiodynamic curve for bare 316L SS (curve d) shows a passive region followed by an increase in current density at 0.35 V versus Ag/AgCl, indicating the breakdown of passivity and the onset of pitting corrosion [36]. In the case of the substrate coated with RCeNaSa and RCeHAsc, no change in the pitting corrosion potential is observed due to the presence of films. This result can be explained by the open structure of the formed coatings observed by SEM microscopy, which allows aggressive ions to easily reach the substrate and causes pitting at the studied potentials. In contrast, the RCeMo film causes a slight shift of the corrosion potential to more positive values, suggesting a low barrier effect against a corrosive species.

To evaluate the anticorrosion properties of 316L SS covered with the different coatings, Tafel polarization curves for the uncoated and coated substrates are presented in **Figure 9**. **Table 1** lists the parameters obtained from extrapolation of the curves. As can be seen from **Figure 9**, none of the cerium coatings reduce the rate of corrosion the corrosion rate of the substrate in Ringer's solution, but they shift the corrosion potential to more anodic values. On the other hand, the data in **Table 1** show that for RCeNaSa coated sample, the E_{corr} value increases by 280 mV compared to bare 316L SS. According to the above results, it can be suggested that RCeNaSa sample coating presents the best corrosion resistance in Ringer solution. The anticorrosive properties are associated as previously reported; the improved inhibition performance of RCeNaSa is due to a synergistic effect of this compound in which both components, which are inhibitors of 316L SS by themselves, are simultaneously incorporated into a surface coating, as shown by the above results. This is because the organic component (NaSa) is predominantly an anodic inhibitor [29], while the cerium (under these circumstances) proves to be predominantly a cathodic inhibition [31].

Sample	E_{corr} (V)	i_{corr} (mA cm^{-2})
RCeNaSa	0.100 ± 0.018	$5.0 \times 10^{-4} \pm 2.35 \times 10^{-6}$
RCeMo	−0.016 ± 0.017	$4.5 \times 10^{-5} \pm 1.56 \times 10^{-6}$
RCeHAsc	0.016 ± 0.015	$4.0 \times 10^{-6} \pm 1.70 \times 10^{-7}$
316L SS	−0.180 ± 0.013	$5.0 \times 10^{-4} \pm 3.55 \times 10^{-6}$

Table 1.
Tafel parameters for a 316L SS electrode uncovered and covered with the different coatings.

Considering the obtained results, it was decided to continue the studies with the 316L SS electrode covered with RCeNaSa coating. In a further step and with the aim of obtaining antibacterial properties, the 316L SS electrode covered with RCeNaSa coating was modified with silver nanoparticles. The incorporation of AgNps on the cerium-salicylate based film from a solution containing 0.01 M $AgNO_3$ and 0.1 M KNO_3, was carried out using a double-pulse technique. When RCeNaSa is modified with AgNps, the surface becomes silvery. Now, RCeNaSaAg also showed the morphology of mud cracks, but in this case, it was completely covered with AgNps with spherical morphology (**Figure 10A**). The size of the nanospheres is estimated by SEM to be between 50 and 150 nm. This type of silver nanospheres morphology was previously studied by Wang and Zheng, who electrodeposited silver nanoparticles on

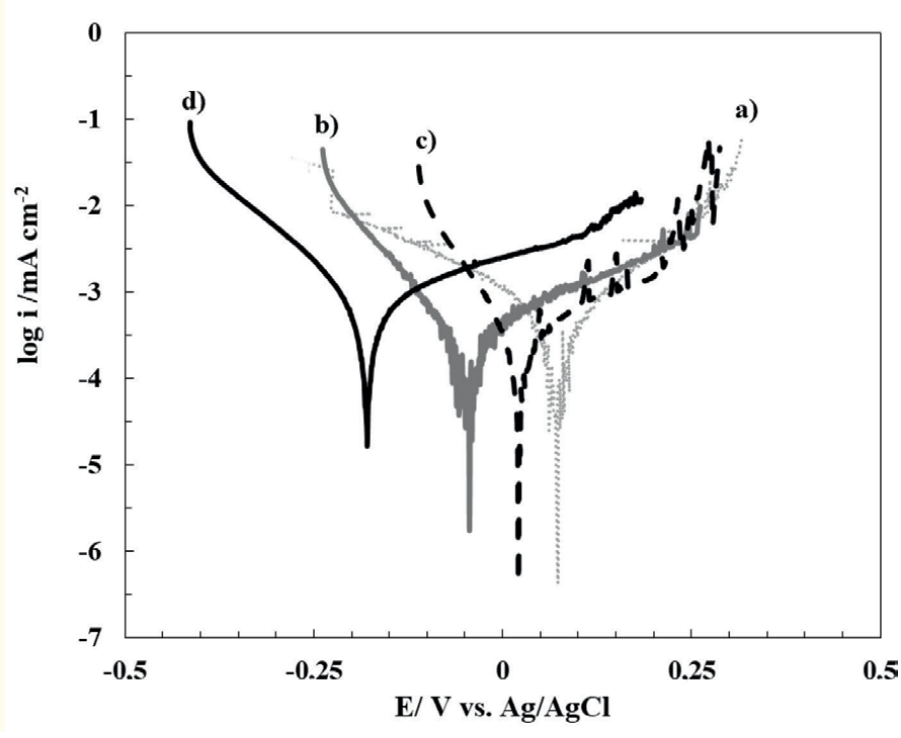

Figure 9.
Tafel curves obtained in ringer solution of 316L SS electrode covered with: (a) RCeNaSa coating, (b) RCeMo coating, and (c) RCeHAsc film. Tafel polarization plot of the uncoated steel is also included (d). The scan rate was 0.001 Vs^{-1}.

a zinc oxide layer [37]. As expected, the EDX spectrum of RCeNaSaAg showed the signal of Ag, confirming the presence of silver nanoparticles.

5. Antibacterial activity of RCeNaSa coating

The next step was evaluating the antibacterial activity of RCeNaSa film modified with AgNps against the Gram-negative bacterium *E. coli* by determining the width of the zone of inhibition around the sample. The antimicrobial activities of the covered electrodes are shown in **Figure 11**. As expected, the unmodified RCeNaSa coating does not possess antibacterial properties. On the other hand, the coatings with AgNps showed a remarkable inhibition zone with a measured diameter of 14 mm. Considering that in the agar diffusion method, the diameter of the inhibition zones on the agar plates is measured with a ruler of 1 mm resolution, the possibility of measurement errors must be taken into account. However, this method can be used to demonstrate the potential antibacterial activity of the samples against *E. coli*. In the agar diffusion technique, the DIZ surrounding a sample serves as an indicator of the sensitivity of the microorganisms to the composite.

In latest years, several interrelated studies have aimed to improve the use of AgNps for bacterial inhibition. However, the debate on the bactericidal mechanism of action of AgNps continues. It has been shown that the antibacterial properties of AgNps are mainly due to a two-step mechanism. First, Ag^+ ions are released from

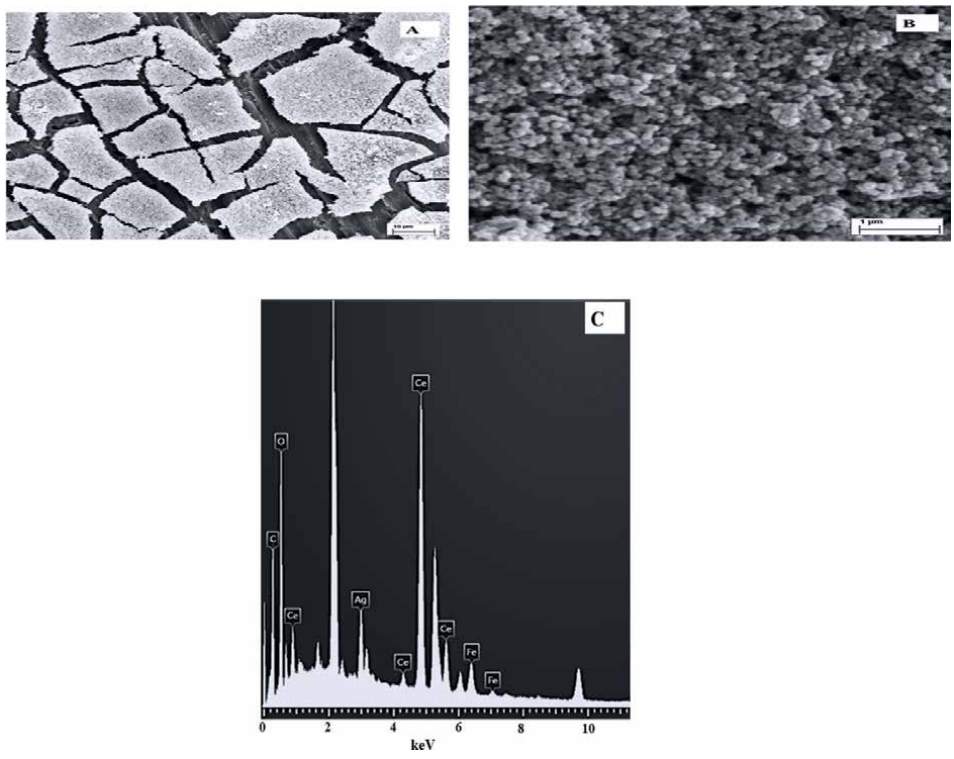

Figure 10.
(A) SEM image of the 316L SS covered with RCeNaSaAg coating, (B) magnified area of (A), and (C) EDX examination.

the nanoparticles. Then, the Ag^+ ions take interaction with cellular targets, leading to their antibacterial effect [27]. Another proposed mechanism is cellular uptake of AgNps, which is related to physical interaction and takes place when the Nps are small enough to cross the cell membrane [38]. Mukha et al. reported that AgNps smaller than 10 nm present antibacterial activity due to both membrane damage and their ability to penetrate into the cell [39]. In general, bacterial cells have micron-scale size, while their outer cell membranes have nanometer-scale pores (< 50 nm). As the AgNps synthesized in this study have larger size than the outer cell membrane pores, it can be assumed that they cannot penetrate the cell membrane.

6. Conclusion

Anticorrosive, adherent, and morphologically homogeneous cerium-based films were obtained on 316L SS in solutions containing cerium nitrate, hydrogen peroxide, and three different additives (NaSa, Na_2MoO_4, and HAsc). The corrosion resistance of all RCe films electrogenerated in the presence of additives is superior to RCe coating in simulated body fluid solution. The RCeNaSa-coated 316L SS showed *improved anticorrosive performance* in Ringer solution. The addition of AgNps on the RCeNaSa layer contributes to a remarkable antibacterial effect without losing the anticorrosive efficiency. The improvement of the anticorrosive behavior is related to the deposition of insoluble cerium compounds and the properties of each additive.

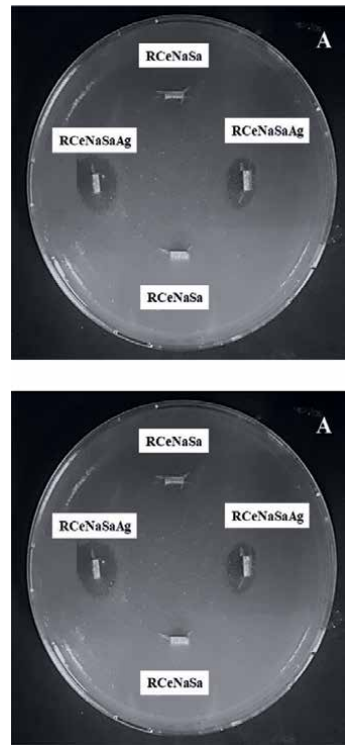

Figure 11.
Photograph of the inhibition zone diameter against E. coli for 316L SS sheet covered with RCeNaSaAg. The information of the unmodified coating is also presented.

Acknowledgements

CONICET, ANPCYT and Universidad Nacional del Sur, Bahía Blanca, Argentina are acknowledged for financial support.

Conflict of interest

The authors declare no conflict of interest.

Nomenclature

AgNps	Silver nanoparticles
EDX	Energy Dispersive X-Ray Spectroscopy
HAsc	Ascorbic acid
NaSa	Sodium salycilate
Na_2MoO_4	Sodium molybdate
RCe	Cerium-based coating obtained at - 0.70 V in 30 mM $Ce(NO_3)_3$, 25 mM H_2O_2 solution
RCeNaSa	Cerium-based coating obtained at - 0.70 V in 30 mM $Ce(NO_3)_3$, 25 mM H_2O_2, and 5 mM NaSa solution
RCeNaSaAg	Cerium-based coating obtained at - 0.70 V in 30 mM $Ce(NO_3)_3$, 25 mM H_2O_2, and 5 mM NaSa solution. The AgNps were synthesized from a solution containing 0.01 M $AgNO_3$ and 0.1 M KNO_3, was carried out using a double-pulse technique.
RCeMo	Cerium-based coating obtained at - 1.00 V in 30 mM $Ce(NO_3)_3$, 25 mM H_2O_2, and 15 mM Na_2MoO_4 solution
RCeHAsc	Cerium-based coating obtained at - 0.80 V in 50 mM $Ce(NO_3)_3$, 25 mM H_2O_2, and 1 mM HAsc solution
SEM	*Scanning Electron Microscopy*
316L SS	316L stainless steel

DOI: http://dx.doi.org/10.5772/intechopen.1003027

Author details

Nadia C. Cortes[1], Ana P. Loperena[1], Lorena I. Brugnoni[2,3], María Belén González[1] and Ivana L. Lehr[1*]

1 Chemical Engineering Department, Institute of Electrochemical and Corrosion Engineering, National University of the South, Bahía Blanca, Argentina

2 Department of Biology, Biochemistry and Pharmacy, National University of the South, Bahía Blanca, Argentina

3 Institute of Biological and Biomedical Sciences, Bahia Blanca, Argentina

*Address all correspondence to: ilehr@uns.edu.ar

IntechOpen

References

[1] Katta PPK, Nalliyan R. Corrosion resistance with self-healing behavior and biocompatibility of Ce incorporated niobium oxide coated 316L SS for orthopedic applications. Surface and Coatings Technology. 2019;**375**:715-726. DOI: 10.1016/j.surfcoat.2019.07.042

[2] Pandey AK, Kumar A, Kumar R, Gautam RK, Behera CK. Tribological performance of SS 316L, commercially pure titanium, and Ti6Al4V in different solutions for biomedical applications. Materials Today Proceedings. 2023;**78**:A1-A8. DOI: 10.1016/j.matpr.2023.03.736

[3] Wu G, Zhang S, Wang Y, Sun M, Qli Z, Kovalenko V, et al. Porous ceramic coating formed on 316L by laser cladding combined plasma electrolytic oxidation for biomedical application. Transactions of the Nonferrous Metals Society of China. 2022;**32**:2993-3004. DOI: 10.1016/S1003-6326(22)65998-3

[4] Say Y, Aslan N, Alla AMA, Özmen H. Influence of chemical etchings on surface properties, in-vitro degradation and ion releases of 316L stainless steel alloy for biomedical applications. Materials Chemistry and Physics 2023; 295: 127139-127153 DOI:10.1016/j.matchemphys.2022.127139.

[5] Zhuang Y, Zhang S, Yang K, Ren L, Dai K. Antibacterial activity of copper-bearing 316L stainless steel for the prevention of implant-related infection. Journal of Biomedical Materials Research Part B: Applied Biomaterials. 2020;**108**:484-495. DOI: 10.1002/jbm.b.34405

[6] Hayajneh MT, Almomani M, Al-Daraghmeh M. Development and evaluation of a thin cerium oxide-gelatin nanolaminate coating for corrosion protection of AISI 316L stainless steel. Manufacturing Technology. 2021;**21**:330-339. DOI: 10.21062/mft.2021.036

[7] Rajeshkumar S, Naik P. Synthesis and biomedical applications of cerium oxide nanoparticles – A review. Biotechnology Reports. 2018;**17**:1-5. DOI: 10.1016/j.btre.2017.11.008

[8] Yang S, Sun R, Chen K. Self-healing performance and corrosion resistance of phytic acid/cerium composite coating on microarc-oxidized magnesium alloy. Chemical Engineering Journal. 2022;**428**:131198-131210. DOI: 10.1016/j.cej.2021.131198

[9] Calado LM, Taryba MG, Morozov Y, Carmezim MJ, Montemor MF. Novel smart and self-healing cerium phosphate-based corrosion inhibitor for AZ31 magnesium alloy. Corrosion Science. 2020;**170**:108648-108660. DOI: 10.1016/j.corsci.2020.108648

[10] Yeasmin F, Choi HW. Natural salicylates and their roles in human health. International Journal of Molecular Sciences. 2020;**21**:1-16. DOI: 10.3390/ijms21239049

[11] Hamdaoui S, Lambert A, Khireddine H, Agniel R, Cousture A, Coulon R, et al. An efficient and inexpensive method for functionalizing metallic biomaterials used in orthopedic applications. Colloids and Interface Science Communication. 2020;**37**:100282-100291. DOI: 10.1016/j.colcom.2020.100282

[12] Ananth KP, Nathanael AJ, Jose SP, Oh TH, Mangalaraj D. A novel silica nanotube reinforced ionic incorporated hydroxyapatite composite coating on polypyrrole coated 316L SS for implant application. Materials Science and Engineering: C. 2016;**59**:1110-1124. DOI: 10.1016/j.msec.2015.10.045

[13] Jabara R, Chronds N, Robinson K. Novel bioabsorbable salicylate-based polymer as a drug-eluting stent coating. Catheterization and Cardiovascular Interventions. 2008;**72**:186-194. DOI: 10.1002/ccd.21607

[14] Li X, Deng S, Fu H. Sodium molybdate as a corrosion inhibitor for aluminium in H_3PO_4 solution. Corrosion Science. 2011;**53**:2748-2753. DOI: 10.1016/j.corsci.2011.05.002

[15] Kapp RWJr. Molybdenum In: Wexler P (Editor–in-Chief), Encyclopedia of Toxicology, third ed., Elsevier, London. 2014 p. 383-388. ISBN-13: 978-0123864543; ISBN-10: 0123864542

[16] Mu S, Du J, Jiang H, Li W. Composition analysis and corrosion performance of a Mo–Ce conversion coating on AZ91 magnesium alloy. Surface and Coating Technology. 2014;**254**:364-370. DOI: 10.1016/j.surfcoat.2014.06.044

[17] Hu J, Li Q, Zhong X, Zhang L, Chen B. Composite anticorrosion coatings for AZ91D magnesium alloy with molybdate conversion coating and silicon sol–gel coatings. Progress in Organic Coating. 2009;**66**:199-205. DOI: 10.1016/j.porgcoat.2009.07.003

[18] González MB, Saidman SB. Electrodeposition of Polypyrrole on 316 stainless steels for corrosion prevention. Corrosion Science. 2011;**53**:276-282. DOI: 10.1016/j.corsci.2010.09.021

[19] Ferrerira ES, Giacomellu C, Spinelli A. Evaluation of the inhibitor effect of L-ascorbic acid on the corrosion of mild steel. Materials Chemistry and Physics. 2004;**83**:129-134. DOI: 10.1016/j.matchemphys.2003.09.020

[20] Akrout H, Bousselmi L, Triki E, Maximovitch S, Dalard F. Effect of non-toxic corrosion inhibitors on steel in chloride solution. Journal of Materials Science. 2004;**39**:7341-7350. DOI: 10.1023/B:JMSC.0000048749.31437.b9

[21] Valek L, Martinez S, Mikulic D, Brnardic I. The inhibition activity of ascorbic acid towards corrosion of steel in alkaline media containing chloride ions. Corrosion Science. 2008;**50**:2705-2709. DOI: 10.1016/j.corsci.2008.06.018

[22] Fuchs-Godex R, Pavlovic M, Tomic M. The inhibitive effect of vitamin-C on the corrosive performance of steel in HCl solutions. International Journal of Electrochemical Science. 2013;**8**:1511-1519

[23] Xin S, Xu R, Yan H, Shen P, Li M. Electrochemical corrosion behaviour of cerium chemical conversion coatings on 304 stainless steel in alkaline solutions containing chloride ions. International Journal of Electrochemical Science. 2019;**14**:11012-11018. DOI: 10.20964/2019.12.84

[24] Abdulaah HA, Ghaban AA, Anaee RA, Khadom AA, Kadhim MM. Cerium-tricalcium phosphate coating for 316L stainless steel in simulated human fluid: Experimental, biological, theoretical, and electrochemical investigations. Journal of Electrochemical Science and Engineering. 2023;**13**:115-126. DOI: 10.5599/jese.1257

[25] Alias R, Mahmoodian R, Abd Shukor MH. Development and characterization of a multilayer silver/silver-tantalum oxide thin film coating on stainless steel for biomedical applications. International Journal of Adhesion and Adhesives. 2019;**92**:89-98. DOI: 10.1016/j.ijadhadh.2019.04.010

[26] Wang H, Xu X, Wang X, Qu W, Qing Y, Li S, et al. Performance optimization of biomimetic ant-nest silver nanoparticle coatings for

antibacterial and osseointegration of implant surfaces. Biomaterials Advances. 2023;**149**:213394. DOI: 10.1016/j.bioadv.2023.213394

[27] Sotiriou GA, Meye A, Knijnenburg JT, Panke S, Pratsinis SE. Quantifying the origin of released Ag+ ions from nanosilver. Langmuir. 2012;**28**:15929-15936. DOI: 10.1021/la303370d

[28] Loperena AP, Lehr IL, Saidman SB. Cerium oxides for corrosion protection of AZ91D Mg alloy. In: Khan SB, Akhtar K, editors. Cerium Oxide—Applications and Attributes. London: IntechOpen; 2019. pp. 23-41. DOI: 10.5772/intechopen.79329

[29] González MB, Saidman SB. Corrosion protection properties of polypyrrole electropolymerized onto steel in the presence of salicylate. Progress in Organic Coating. 2012;**75**(3):178-183. DOI: 10.1016/j.porgcoat.2012.04.015

[30] Loperena AP, Lehr IL, Saidman SB. Formation of a cerium conversion coating on magnesium alloy using ascorbic acid as additive. Characterisation and anticorrosive properties of the formed films. Journal of Magnesium and Alloys. 2016;**4**(4):278-285. DOI: 10.1016/j.jma.2016.10.002

[31] Breslin C, Chen C, Mansfeld F. The electrochemical behaviour of stainless steels following surface modification in cerium containing solutions. Corrosion Science. 1997;**39**(6):1061-1073. DOI: 10.1016/S0010-938X(97)00007-3

[32] Chen S, Zhang S, Ren X, Xu S, Yin L. Cerium-based chemical conversion coating on aluminum alloy to inhibits corrosion in chloride solution. International Journal of Electrochemical Science. 2015;**10**:9073-9088

[33] Wang C, Zhu S, Jiang F, Wang F. Cerium conversion coatings for AZ91D magnesium alloy in ethanol solution and its corrosion resistance. Corrosion Science. 2009;**51**:2916-2923. DOI: 10.1016/j.corsci.2009.08.003

[34] Lehr IL, Saidman SB. Corrosion protection of AZ91D magnesium alloy by a cerium-molybdenum coating-the effect of citric acid as an additive. Journal of Magnesium and Alloys. 2018;**6**:356-365. DOI: 10.1016/j.jma.2018.10.002

[35] Hamlaoui Y, Pedraza F, Remazeilles C, Cohendoz S, Rébéré C, Tifouti L, et al. Cathodic electrodeposition of cerium-based oxides on carbon steel from concentrated cerium nitrate solutions: Part I, electrochemical and analytical characterization. Materials Chemistry and Physics. 2009;**113**:650-657. DOI: 10.1016/j.matchemphys.2008.08.027

[36] Sudesh TL, Wijesinghe L, Blackwood DJ. Real time pit initiation studies on stainless steels: The effect of sulphide inclusions. Corrosion Science. 2007;**49**:1755-1764. DOI: 10.1016/j.corsci.2006.10.025

[37] Wang Q, Zheng J. Electrodeposition of silver nanoparticles on a zinc oxide film: Improvement of amperometric sensing sensitivity and stability for hydrogen peroxide determination. Microchimica Acta. 2010;**169**:361-365. DOI: 10.1007/s00604-010-0356-7

[38] McQuillan JS, Shaw AM. Differential gene regulation in the Ag nanoparticle and Ag(+)-induced silver stress response in Escherichia coli: A full transcriptomic profile. Nanotoxicology. 2014;**8**(Suppl. 1):177-184. DOI: 10.1021/la303370d

[39] Mukha IP, Eremenko AM, Smirnova NP, Mikhienkova AI, Korchak GI, Gorchev VF, et al. Antimicrobial activity of stable silver nanoparticles of a certain size. Applied Biochemistry and Microbiology. 2013;**49**:199-206. DOI: 10.1134/S0003683813020117

Chapter 6

Perspective Chapter: Forging the Future – An Economic and Geographical Odyssey of World Steel Production and Its Path Ahead

Nidhi Nischal and M. Vijay Kumar

Abstract

Steel manufacture is a carbon and energy intensive process that, globally, on average, emits 1.9 tonnes of carbon-dioxide (CO_2) and uses 5.17 MWh of primary energy per ton produced, accounting for 9% of 11 human CO_2 emissions. The structure of the world's steel production must fundamentally change if the Paris Agreement's objectives of keeping global temperature increase below 1.5°C from preindustrial levels are to be met. There are a number of technological avenues leading to a lower carbon intensity for steelmaking, which bring with them a paradigm shifts decoupling CO_2 emissions from crude steel production by moving away from traditional methods of steel production using fossil coal and fossil methane and toward those based on reasonably priced renewable electricity and green hydrogen. The effects of fully defossilized steelmaking have not yet been thoroughly studied with regard to the energy system. A Gross Domestic Product (GDP)—based demand model for global steel demands, which forecasts an increase in steel demand from 1.6 Gt in 2020 to 2.4 Gt in 2100, is used in this study to investigate the energy system requirements of a global defossilized power-to-steel sector.

Keywords: steel production, trends in steel, advances of steel, future steel demand, steel industry

1. Introduction

Iron is created by removing oxygen and other impurities from iron ore. Iron is combined with carbon, recycled steel, and small amounts of other elements to form steel. Steel is the most significant material utilized in engineering and construction globally. It is utilized in every aspect of our lives, including automobiles, construction materials, washing machines, cargo ships, and surgical scalpels [1].

In the yearly World Steel in Figures book, which is released in early June, world steel updates the list of nations that produce steel. The Steel Statistical Yearbook, which is published in November/December, may make additional changes to the

ranking. Via the Steel Data Viewer, world steel publishes monthly statistics on country steel output for both the current and prior year [1].

The yearly World Steel in Figures book from world steel includes an updated list of significant steel-producing firms. Below 913°C (1,675°F) and between 1395°C (2,543°F) and its melting point of 1539°C (2,802°F), iron has a bcc allotropy. Iron in its bcc structure is referred to as ferrite, but it is also known as alpha iron at low temperatures and delta iron at high temperatures. Iron is in its fcc order between 913 and 1395°C, also known as austenite or gamma iron. With very few exceptions, steel retains iron's allotropic characteristic even when the alloy contains sizable amounts of other elements (Britannica Technology).

For many years, steel's usage in recent years has significantly expanded. For instance, between 1950 and 2018, the yearly global production of crude steel (CS) climbed from 201 megatons (Mt) to 1805 MtCS [1]. Despite a 60% drop in energy intensity over the past 50 years, one tonne of steel still requires an average of 5.18 MWhth of primary energy to create.

One of austenitic stainless steel's most significant qualities is its good weldability. These steels have more broad applications now than other stainless steels do as a result. The main industries for these applications are petrochemical, high pressure storage, and chemical storage tanks. The chemical composition, mechanical properties, and especially toughness of the welds in austenitic stainless steels are often comparable to those of the base metals. These steels do not break easily in the cold. These steels typically do not require pre-heating or post-weld heating because of the stable structure of austenite.

2. History/evolution of steel

Cast iron (1.8–4.4% carbon) is created when iron starts to absorb carbon at extremely high temperatures, lowering the MP of the metal. Iron production grew with the development of blast furnaces, which were originally employed by the Chinese in the 6th century – B.C. but were utilized in Europe during the Middle Ages. Liquid iron that has been cooled in the main chamber is known as pig iron. The enormous central ingot and the tinier, encircling ingots looked like a sow and her calves. Due to its high carbon content, cast iron is strong but brittle, making it difficult to work with and shape. Once metallurgists learned that the brittleness of iron was mostly caused by its high carbon content, they experimented with novel ways to lower the carbon level and make iron more feasible. By the late 18th century, ironworkers had mastered the use of puddling furnaces to convert pig iron into wrought iron (developed by Henry Cort in 1784). Puddlers had to stir the molten iron with long, oar-shaped implements as the furnaces heated them, allowing oxygen to react with and gradually remove carbon. Iron's melting point rises as carbon content falls, causing masses of iron to clump together in the boiler. The puddler would take these masses out and shape them into sheets or rails using a forge hammer. Although Britain had over 3000 puddling furnaces by 1860, the process was still hindered by the need for a lot of manpower and fuel. Blister steel is one of the oldest types of steel. In this procedure, heated stone boxes contained wrought iron bars coated with charcoal powder. The iron would eventually absorb the carbon from the charcoal after about a week. Blister steel was produced after repeated heating because the carbon was distributed more uniformly. Because blister steel had a larger carbon content than pig iron, it was considerably easier to press or roll. English clockmaker Benjamin Huntsman learned

that high-quality steel could be produced for his clock springs by melting the metal in clay crucibles and then polishing it with a specific flux to eliminate cementation slag. The 1740s saw a development in blister steel production as a result of this discovery. The result was a steel crucible, or cast. However, blister or cast steel has only ever been employed in specific applications due to the high cost of production. As a result, cast iron produced in puddling furnaces continued to be used as the primary structural metal in industrializing Britain for the bulk of the 19th century [2].

2.1 The Bessemer process and modern steelmaking

The iron industry, which still suffered from ineffective manufacturing methods, was under tremendous pressure from the expansion of railroads during the 19th century in both Europe and America. Steel manufacture was slow and expensive, and it had not yet been demonstrated to be a reliable structural metal. That is, until Henry Bessemer discovered a more efficient way to add oxygen to molten iron in 1856, lowering the carbon level. Bessemer created a pear-shaped container, or "converter," in which iron could be heated and oxygen could be blown through the molten metal, leading to the development of what is now known as the Bessemer Process. The molten metal would react with the carbon when oxygen traveled through it, releasing carbon dioxide and creating a more pure iron. The method, which removed silicon and carbon from iron for a low cost and in a short amount of time, suffered from being too effective. In the finished product, too much oxygen predominated and too much carbon was eliminated. In the end, Bessemer had to pay back his investors while he looked for a way to raise the carbon content and remove the excess oxygen. A similar period saw the acquisition and testing of spiegeleisen, a mixture of iron, carbon, and manganese, by British metallurgist Robert Mushet. The carbon content in the spiegeleisen, if added in the correct amounts, would give the solution to Bessemer's issues because manganese was known to remove oxygen from molten iron. With tremendous success, Bessemer started using it into his conversion procedure. One issue persisted. Bessemer had been unable to eliminate phosphorus from his final product phosphorus, a harmful contaminant that renders steel brittle. Only phosphorus-free ore from Sweden and Wales could be applied as a result. Sidney Gilchrist Thomas, a Welshman, discovered the remedy in 1876 by incorporating limestone, a chemically basic flux, into the Bessemer process. The undesirable element was removed because the limestone pulled phosphorus from the pig iron into the slag. With this invention, steel could then be produced from iron ore from anywhere in the world. It should come as no surprise that steel production costs started to drop considerably. Because of the new methods for producing steel, the cost of steel rail decreased by more than 80% between 1867 and 1884, sparking the expansion of the global steel industry [2].

2.2 Birth of the steel industry

A number of businessmen at the time identified an investment opportunity in the revolution in steel production, which resulted in the manufacture of cheaper, higher-quality material. Investors in the steel industry in the late 19th century made millions of dollars—in Carnegie's case, billions—during that time, including Charles Schwab and Andrew Carnegie. US Steel Corporation, founded by Carnegie, was the 1st business to be valued at over $1 billion.

2.3 Electric arc furnace(EAF) steelmaking

Another event that would have a significant impact on the growth of steel production happened shortly after the turn of the century. Paul Heroult created the electric arc boiler to exothermically oxidize charged material at temperatures as high as 3272°F (1800°C), which is more than enough to heat steel manufacture. EAFs were firstly utilized for the production of specialty steels. Particularly in the case of carbon steels or long products, they were able to compete with the large American companies like US Steel Corp. and Bethlehem Steel because to the low investment costs associated with building up EAF mills. Less energy is required per unit of production for EAFs since steel can be made entirely from scrap or cold ferrous feed. Operations can be interrupted and started with low related expenses, in contrast to simple oxygen hearths. Because of these factors, the amount of steel produced using EAFs has been rising continuously for more than 50 years and today makes up roughly 33% of the world's total steel production [3].

2.4 Oxygen steelmaking

Currently, basic oxygen facilities create around 66% of the world's steel. Small oxygen furnaces can blow oxygen into vast quantities of liquid iron and waste steel, which makes them faster at charging than open-hearth operations. Large vessels with a capacity of up to 350 metric tons of iron may convert iron to steel in less than an hour. Open-hearth factories started to close after oxygen steelmaking was introduced in the 1960s because it was more affordable and made them less competitive. It shut down in 1992 both in the US and in China in 2001.

3. Future of steel

3.1 Future steel demand

According to the GDP and population growth forecasts made by Toktarova et al. [4], the world's steel output continues to rise at its current rate until 2030 (**Figure 1** up left), when it slows down and achieves a maximum of 2336 Mt. (**Figure 1** up right). Every 10 years, 10% of the vertical space between each point in **Figure 1**'s points and the curve is closed. When low-income nations develop as projected but slowly, global steel production rises progressively starting in 2060 (**Figure 1** below left), achieving steady-state steel production per person by 2100 and overall production of 2418 Mt. in 2100. (**Figure 1** below right) [3].

As shown in **Table 1**, the production of latest steel (primary steel) rises gradually till 2040, when it is anticipated to reach a level of around 1.5 GtCS, before dropping precipitously from 2040 to 2060 and stabilizing at about 0.3 Gt in 2100. The percentage of recycled steel overtakes the percentage of new steel starting in 2060 and stabilizes at 89.1% in 2100. Steel recycling, which now averages 80.6% globally, might climb to 88.1% if actions were taken internationally to promote global recycling across sectors without improvements in sectors with low recycling rates.

3.2 Future energy demand and carbon intensity for steel production

Figures 2 and **3** display the worldwide thermal and electrical energy requirements for the three scenarios' steel production. In all cases, recycling steel in an EAF boiler

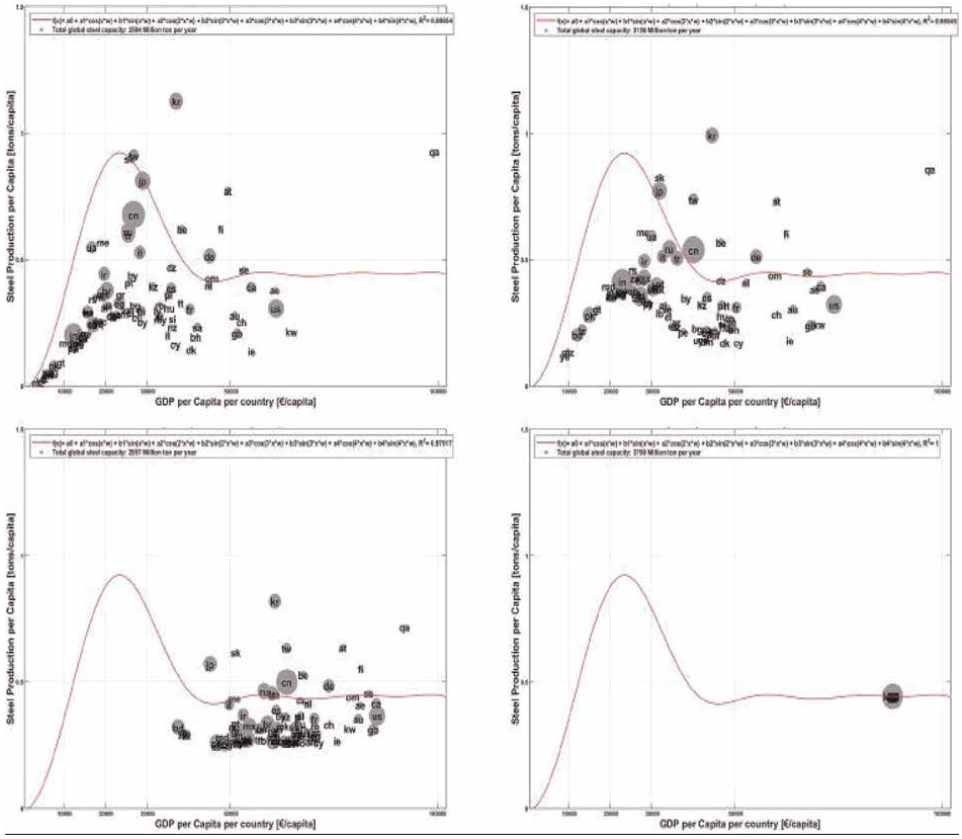

Figure 1.
Proportion of per-capita steel output over per-capita GDP in 2030-up left, 2040- up right, 2060-below left and 2100-below right.

Empty cell	2015	2020	2030	2040	2050	2060	2070	2080	2090	2100
Total steel (GtCS)	1.61	1.72	2.06	2.35	2.13	2.05	2.12	2.23	2.33	2.41
Primary steel (GtCS)	1.22	1.24	1.38	1.54	1.18	0.83	0.72	0.52	0.51	0.28
SecondarySteel (GtCS)	0.41	0.49	0.67	0.80	0.96	1.23	1.40	1.71	1.82	2.15
Primary steel	74.4	71.6	67.3	65.5	55.6	40.5	34.2	23.5	22.2	11.1
Recycled steel	25.4	28.4	32.7	34.5	44.6	59.3	65.8	76.5	77.8	89.1

Table 1.
Production estimates for primary and secondary steel in absolute terms and in relation to overall production through the year 2100.

has the biggest influence on the energy demand for steel globally. Due mostly to the electricity required for electrolysis, the High Dynamic Range (H-DR) scenario has the highest electrical energy consumption.

3.3 Geographical distribution

Although the scenario for steel production in **Table 1** depicts an increase in the necessity for steel globally, the development of the various steel-producing countries

may follow different paths. According to the findings of the analysis of 145 regions, the geographic distribution of production capacity is largely mirrored in the regional distribution (2018). Notwithstanding the chance that this structure might change, as described in Section 4, China is still the world's top producer of steel. The color bar scales logarithmically as a result of the huge differences in production levels between the zones. According to **Figure 4**, China will require the most electrical and thermal energy in 2050 (2201 and 1948 TWhel, and 1193 and 767 TWhth of hydrogen for the H-DR and EWIN scenarios, respectively), as well as the most fossil fuels [3] (**Figure 5**).

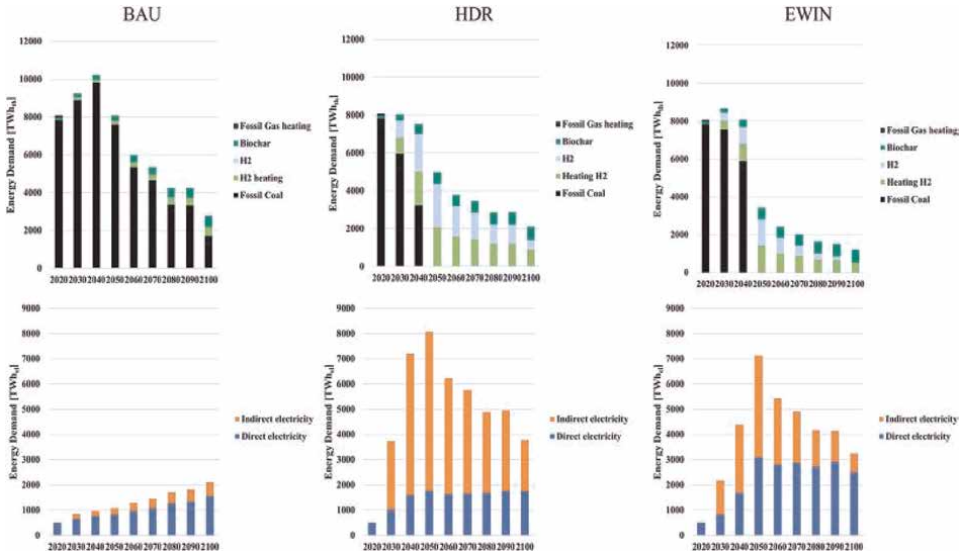

Figure 2.
Thermal energy requirements (up) and electrical energy requirements (below), by fuel and steel production method, for the Business as Usual (BAU) (left), H-DR (middle), and EWIN (right) scenarios, respectively.

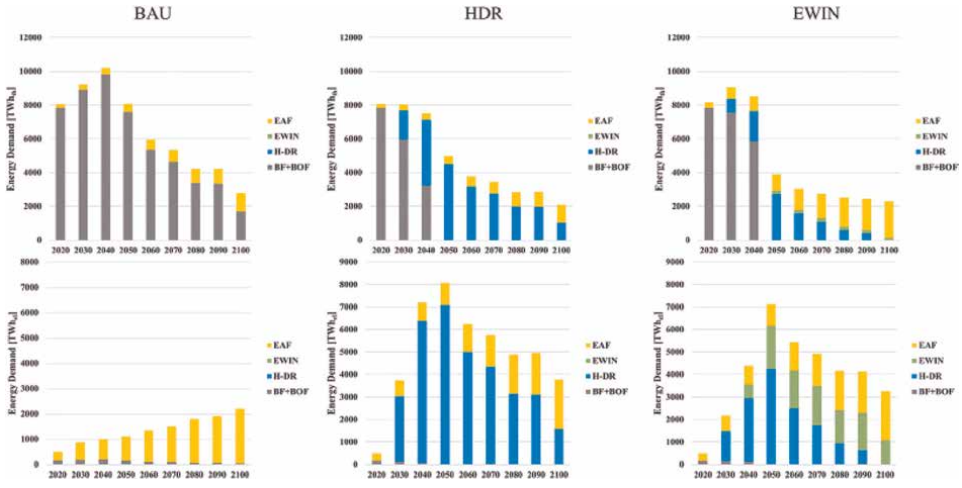

Figure 3.
Energy requirements for technology for the BAU (left), H-DR (middle), and EWIN (right) scenarios, shown on the top and bottom, respectively.

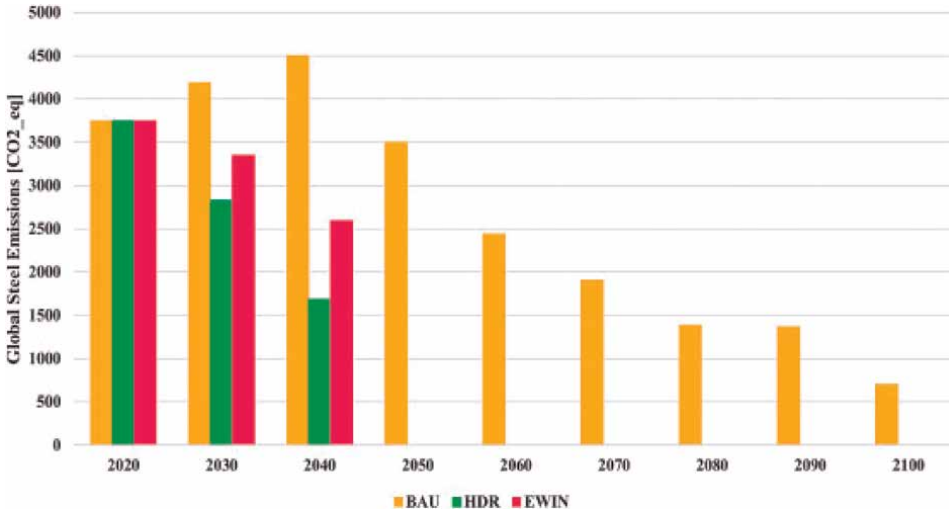

Figure 4.
Under scenarios ranging from 2020 to 2100, worldwide CO_2 emissions for the manufacture of steel are reported.

It is anticipated that global steel production will reach its first high around 2040, followed by a brief dip for the following 20 years, then climb gradually and slowly until it surpasses the 1st peak in the latter half of the 21st century. Due in large part to recycling, which significantly lowers the thermal energy demand, the world's thermal energy demand for the manufacturing of steel is seeing a different pattern.

3.4 Economics of future primary steel alternatives

Figures 6–8 depict, accordingly, the economic feasibility of each of the steel production pathways for a range of energy prices and Greenhouse Gases (GHG) emission costs for the years 2030, 2040, and 2050. Because of the technological maturity H-DR has, it will be the least priced technology in 2030, assuming less electricity costs and a suitably more carbon pricing mechanism. In 2040, here the trend will be maintained as H-DR replaces EWIN as the preferable technology in scenarios with extremely low electricity costs and more emissions costs, respectively. EWIN is highly expensive at lower power rates than the H-DR path due to its high capital costs, which, if reduced in the following decades, will prevent the technology from seriously affecting the steel manufacturing landscape. EWIN is high energy efficient than H-DR, but its high capital costs make it less feasible than H-DR. Because of its greater energy efficiency, Fischedick et al. [5] estimate of a large decline in EWIN capex shows that EWIN will become the preferred steelmaking process for low electricity prices even in the absence of carbon pricing [6].

4. Conclusion

To fulfill the objectives of the Paris Accord and the limitations set forth in the most recent IPCC assessments for a society with zero greenhouse gas emissions, the worldwide steel sector must adapt and change. This study gives the first forecasts of global steelmaking with specific transition paths for a complete and through the end of the

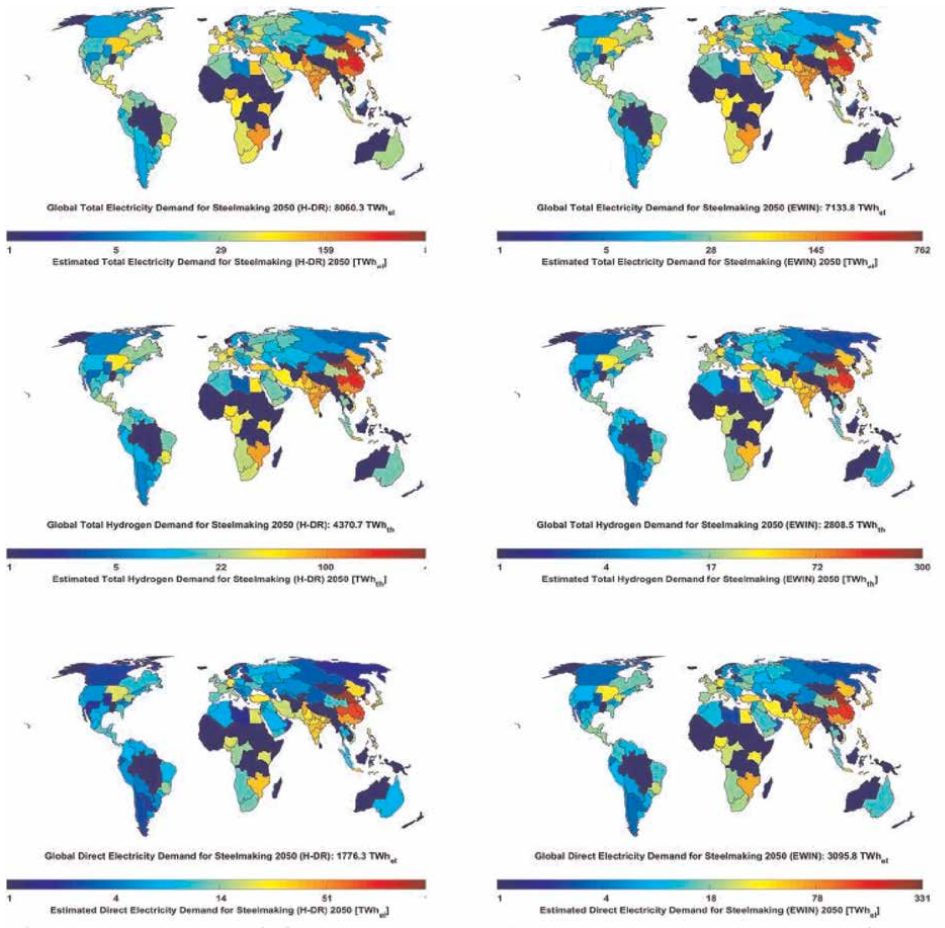

Figure 5.
Projection of the H-DR scenario's 2050 energy requirement for steel production by geographic region.

century with high worldwide-local resolution, the worldwide steel industry can be de-fossilized without the need of CCS or BECCS. For there to be viable routes for a full de-fossilization of the steel sector, the following prerequisites must be satisfied:

- Primary steel manufacturing must replace the use of fossil fuels: Good examples of electricity-based technologies for the production of steel from raw materials are H-DR and EWIN.

- To fully de-fossilize steelmaking, Carbon Capture, Storage and Utilization Technologies are insufficient and furthermore, it is hotly contested whether gaseous CO_2 sequestration even comes close to meeting sustainability requirements.

- A net-zero steel sector is used to decarbonize steel manufacturing. If H-DR takes over as the principal steel manufacturing method, the steel industry might have one of the highest hydrogen demand levels in 2050, with 2800–4400 TWhH2 [7–22].

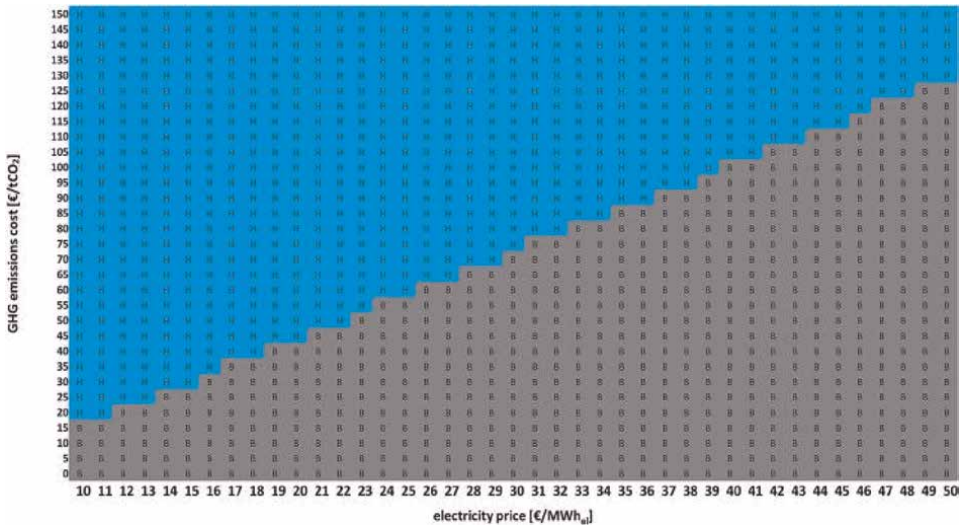

Figure 6.
The least expensive primary steel production method in 2030 for various power costs and GHG emission costs. Blue cells stand in for H-DR, and gray cells for blast furnace (BF) + basic- oxygen furnace (BOF).

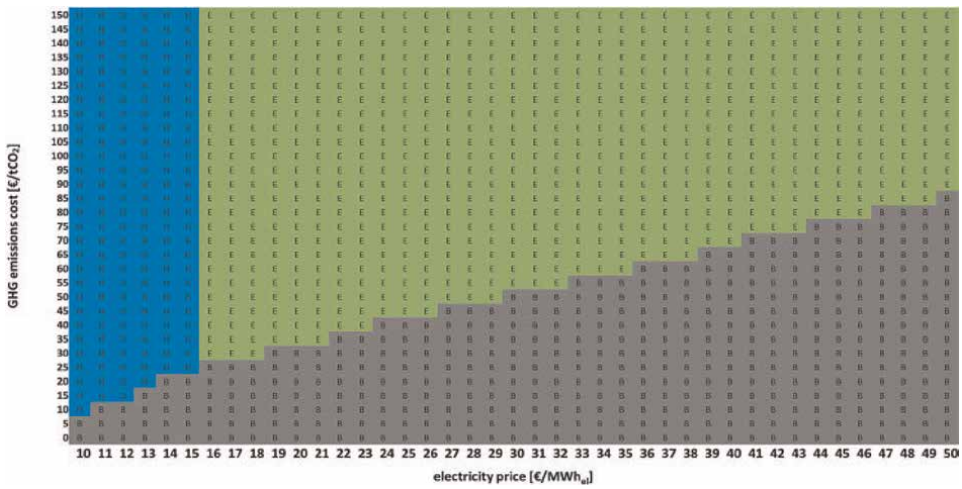

Figure 7.
Shows the least expensive primary steel production technique for 2040, given various power costs and the cost of GHG emissions. Blue cells stand in for H-DR, green cells for EWIN, and gray cells for BF+BOF.

- It is necessary to transition the world's energy system towards very high shares of renewable energy, particularly renewable electricity: The remaining emissions from steelmaking will be those associated with the power sector and how electricity is generated when the industry transitions to electricity-based technology. So long as steel production is entirely powered by electricity and green hydrogen, there would be no greenhouse gas emissions from the power sector, which would enable there to be no greenhouse gas emissions from the steel industry.

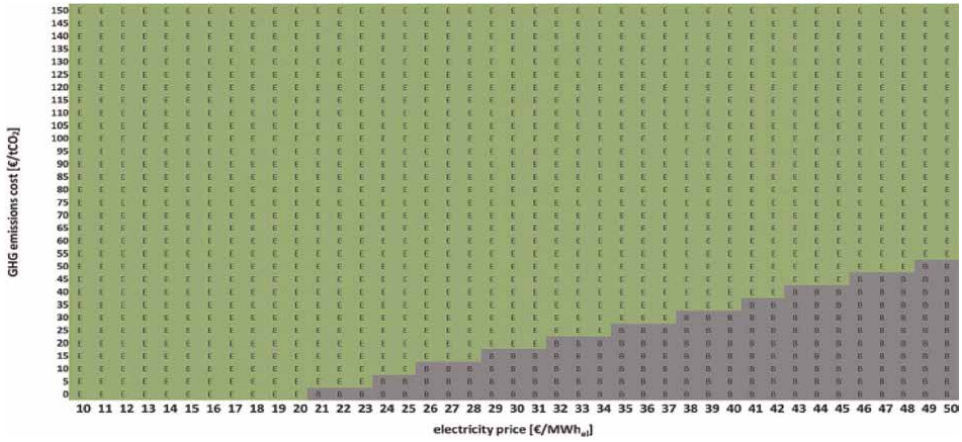

Figure 8.
In 2050, the least expensive primary steel production process will depend on the cost of GHG emissions and the price of power. Blue cells stand in for H-DR, green cells for EWIN, and gray cells for BF+BOF.

- Steel recycling rates must be high: Steel recycling will have a major impact on the energy demand and carbon intensity of steelmaking because steel is a material that may theoretically be recycled to extremely high percentages much exceeding 90% and is already being recycled at a rate of 80.6% at the moment. The primary use of steel nowadays is structural steel, which serves as storage for steel for decades. From 2050 onward, this impact will have very major shares of steel recycling in total steel production [23–43].

Author details

Nidhi Nischal and M. Vijay Kumar*
Department of Industrial Engineering and Management, JSS Academy of Technical Education, Bengaluru, Karnataka, India

*Address all correspondence to: mvkjss@gmail.com

References

[1] World Steel Association by Dr Edwin Basson Director Genera, 2018

[2] Fruehan RJ. Overview of steelmaking processes and their development. The Making, Shaping and Treating of Steel: Steelmaking and Refining Volume. 1998; **1**:2-3

[3] Kallanish. Brazil's steel production. Consumption Fall in June. 2022;**1**:1-22

[4] Toktarova A, Walter V, Göransson L, Johnsson F. Interaction between electrified steel production and the north European electricity system. Journal of Applied Energy. Elsevier. 2022;**310**:1-25

[5] Fischedick M, Marzinkowski J, Winzer P, Weigel M. Techno-economic evaluation of innovative steel production technologies. Journal of Cleaner Production. 2014;**84**:563-580. DOI: 10.1016/j.jclepro.2014.05.063

[6] Lopez G, Farfan J, Breyer C. Trends in the global steel industry: Evolutionary projections and defossilisation pathways through power-to-steel. Journal of Cleaner Production. 2022; **375**:134182

[7] Aboumahboub T, Brecha RJ, Shrestha HB, Fuentes U, et al. Decarbonization of Australia's energy system: Integrated modeling of the transformation of electricity, transportation, and industrial sectors. Energies. 2020;**13**:1-39. DOI: 10.3390/en13153805

[8] Aghahosseini A, Breyer C. Assessment of geological resource potentialfor compressed air energy storage in global electricity supply. Energy Conversion and Management. 2018;**169**:161-173. DOI: 10.1016/j.enconman.2018.05.058

[9] Arens M, Åhman M, Vogl V. Which countries are prepared to green their coal- based steel industry with electricity? - reviewing climate and energy policy as well as the implementation of renewable electricity. Renewable and Sustainable Energy Reviews. 2021;**143**:110938. DOI: 10.1016/j.rser.2021.110938

[10] Bailera M, Lisbona P, Pena B, Romeo LM. A review on CO_2 mitigation in the Iron and steel industry through power to X processes. Journal of CO_2 Utilisation. 2021;**46**:101456. DOI: 10.1016/j.jcou.2021.101456

[11] Bhaskar A, Assadi M, Nikpey Somehsaraei H. Decarbonization of the iron and steel industry with direct reduction of iron ore with green hydrogen. Energies. 2020;**13**:1-23. DOI: 10.3390/en13030758

[12] Bogdanov D, Farfan J, Adovskaia K, Aghahosseini A, Child M, Gulagi A, Oyewo AS, et al. Radical transformation pathway towards sustainable electricity via evolutionary steps. Nature Communications. 2019; **10**(1077):1-16

[13] Bogdanov D, Gulagi A, Fasihi M, Breyer C. Full energy sector transition towards 100% renewable energy supply: Integrating power, heat, transport and industry sectors including desalination. Applied Energy. 2021a;**283**: 116273. DOI: 10.1016/j.apenergy.2020.116273

[14] Meyers RA. Sustainability Science and Technology. New York: Springer New York. pp. 1-30. DOI: 10.1007/978-1-4939-2493-6_1071-1

[15] Brown TW, Bischof-Niemz T, Blok K, Breyer C, Lund H, Mathiesen BV.

Response to 'burden of proof: A comprehensive review of the feasibility of 100% renewable-electricity systems. Renewable and Sustainable Energy Reviews. 2018;**92**:834-847. DOI: 10.1016/j.rser.2018.04.113

[16] Child M, Koskinen O, Linnanen L, Breyer C. Sustainability guardrails for energy scenarios of the global energy transition. Renewable and Sustainable Energy Reviews. 2018;**91**:321-334. DOI: 10.1016/j.rser.2018.03.079

[17] Creutzig F, Ravindranath NH, Berndes G, Bolwig S, Bright R, Cherubini F, et al. Bioenergy and climate change mitigation: An assessment. GCB Bioenergy. 2015;**7**:916-944. DOI: 10.1111/gcbb.12205

[18] Devlin A, Yang A. Regional supply chains for decarbonising steel: Energy efficiency and green premium mitigation. Energy Conversion and Management. 2022;**254**:115268. DOI: 10.1016/j.enconman.2022.115268

[19] Energiewende, Agora, Guidehouse. Making Renewable Hydrogen Cost-Competitive: Policy Instruments for Supporting Green H_2.ETC, 018. Mission Possible: Reaching net-zero carbon emissions from harder-to-abate sectors [WWW Document]. 2021. Available from: https://www.energy-transitions.org/publications/mission-possible/, [Accessed: October 8, 2021]

[20] Gielen D, Saygin D, Taibi E, Birat J-P. Renewables-based decarbonization and relocation of iron and steel making: A case study. Journal of Industrial Ecology. 2020;**24**:1113-1125. DOI: 10.1111/jiec.12997

[21] ETOGAS, 2013. Power to Gas: Intelligente Konvertierung und Speicherung von Energie in der industriellen Umsetzung [WWW Document]. ETOGAS GmbH, Stuttgart. Available from: https://goo.gl/E1vzLb, [Accessed: September 28, 2021]

[22] Fasihi M, Weiss R, Savolainen J, Breyer C. Global potential of green ammoniabased on hybrid PV-wind power plants. Applied Energy. 2021;**294**: 116170. DOI: 10.1016/j.apenergy.2020.116170

[23] Galimova T, Ram M, Bogdanov D, Fasihi M, Khalili S, Gulagi A, et al. Global demand analysis for carbon dioxide as raw material from key industrial sources and direct air capture to produce renewable electricity-based fuels and chemicals. Vol. 1. pp 1-16. DOI: 10.1016/j.jclepro.2022.133920

[24] Goransson L, Lehtveer M, Nyholm E, Taljegard M, Walter V. The benefit of collaboration in the north European electricity system transition—System and sector perspectives. Energies. 2019;**12**: 4648. DOI: 10.3390/en12244648

[25] Grond, L., Schulze, P., Holstein, J., 2013. Systems Analyses Power to Gas [WWW Document]. KEMA NV, Groningen. URL: https://docplayer.net/7637393-Dnv-kema-energy-sustainability-final-report-systems-analyses-power-to-gas-deliverable-1-technology-review.html, [Accessed: September 28, 2021]

[26] Hansen K, Breyer C, Lund H. Status and perspectives on 100% renewable energy systems. Energy. 2019;**175**:471-480. DOI: 10.1016/j.energy.2019.03.092

[27] Hasanbeigi A, Price L, Chunxia Z, Aden N, Xiuping L, Fangqin S. Comparison of iron and steel production energy use and energy intensity in China and the U.S. Journal of Cleaner Production. 2014;**65**:108-119. DOI: 10.1016/j.jclepro.2013.09.047

[28] IEA. Iron and Steel [WWW Document]. 2020a. Available from: h ttps://www.iea.org/reports/iron-and-steel, [Accessed: October 8, 21]

[29] Iron and steel technology roadmap. International steel Agency. Vol. 1. 2020. pp. 1-186

[30] IEA. Energy Technology Perspectives 2020. Paris: International Energy Agency; 2020c

[31] IEA, 2020d. World Energy Model [WWW Document]. IEA, Paris. Available from: https://www.iea.org/reports/world-energy-model, [Accessed: September 24, 2021]

[32] IEA. An Energy Sector Roadmap to Carbon Neutrality in China [WWW Document]. 2021d. Available from: https://www.iea.org/reports/an-energy-sector-roadmap-to-carbon-neutrality-in-china

[33] Jaxa-Rozen M, Trutnevyte E. Sources of uncertainty in long-term global scenarios of solar photovoltaic technology. Nature Climate Change. 2021;**11**:266-273. DOI: 10.1038/s41558-021-00998-8

[34] Karakaya E, Nuur C, Assbring L. Potential transitions in the iron and steel industry in Sweden: Towards a hydrogen-based future? Journal of Cleaner Production. 2018;**195**:651-663. DOI: 10.1016/j.jclepro.2018.05.142

[35] Khalili S, Rantanen E, Bogdanov D, Breyer C. Global transportation demand development impacts on the energy demand and greenhouse gas emissions in a climate-constrained world. Energies. 2019;**12**:3870. DOI: 10.3390/en12203870

[36] Zhang K. Journal of Cleaner Production. Delft, Netherland: Delft University of Technology; Open Access. 2019;**240**:1-21. DOI: 10.1016/S0959-6526(19)33382-7

[37] Mandova H, Leduc S, Wang C, Wetterlund E, Patrizio P, Gale W, et al. For CO_2 emission reduction using biomass in European integrated steel plants. Biomass Bioenergy. 2018;**115**:231-243. DOI: 10.1016/j.biombioe.2018.04.021

[38] Mandova H, Patrizio P, Leduc S, Kjarstad J, Wang C, Wetterlund E, et al. Achieving carbon-neutral iron and steelmaking in Europe through the deployment of bioenergy carbon capture and storage. Journal of Cleaning Products;**218**:118-129. DOI: 10.1016/j.jclepro.2019.01.247

[39] Midrex. World Direct Reduction Statistics 2018 [WWW Document]. 2019. Available from: https://www.midrex.com/wp-content/uploads/Midrex-STATSbook2019Final.pdf, [Accessed: October 8, 2021]

[40] Morfeldt J, Nijs W, Silveira S. The impact of climate targets on future steel production – An analysis based on a global energy system model. Journal of Cleaner Production. 2015;**103**:469-482. DOI: 10.1016/j.jclepro.2014.04.045

[41] Neij L. Cost development of future technologies for power generation—A study based on experience curves and complementary bottom-up assessments. Energy Policy. 2008;**36**:2200-2211. DOI: 10.1016/j.enpol.2008.02.029

[42] Nuber D, Eichberger H, Rollinger B. Circored fine ore direct reduction – The future of modern electric steelmaking. Millennium Steel. 2006;**126**(47–51):2006

[43] Otto A, Robinius M, Grube T, Schiebahn S, Praktiknjo A, Stolten D. Power-to-Steel: reducing CO_2 through the integration of renewable energy and hydrogen into the German steel industry. Energies. 2017;**10**:1-21. DOI: 10.3390/en10040451

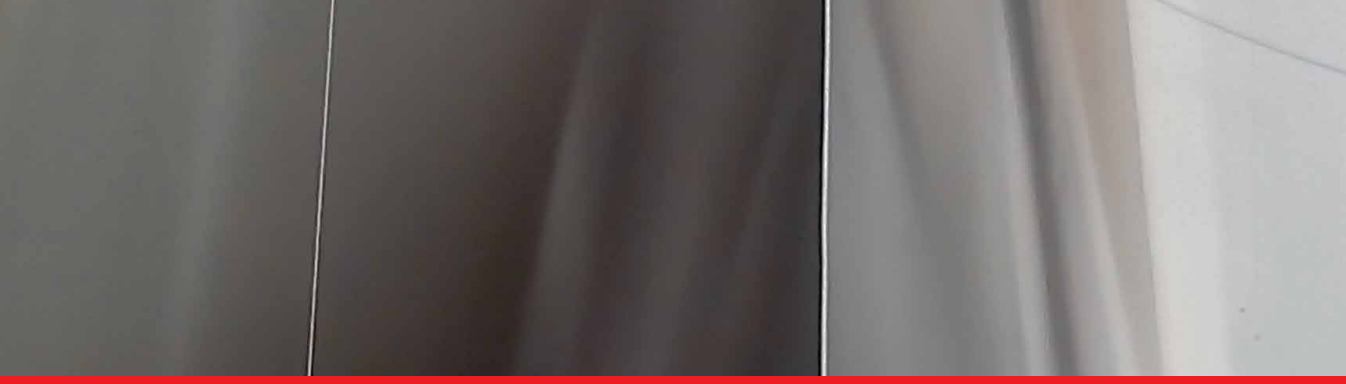

Edited by Adriana da Cunha Rocha

Steel engineering is a vast subject. It encompasses all the methodologies and procedures necessary to fabricate steel as well as includes all the special characteristics that steel must have to work properly in each specific job or demand. Designing steel can not be compared to a cooking recipe – one must understand the intrinsic relationships between each component (elements) of the steel and how those elements interact to provide specific mechanical properties, corrosion resistance, electrical conductivity, and so on. To achieve those properties, the elements must combine in a way during fusion or any similar fabrication process to create the main phases of the steel, which ultimately is the ordered crystal structure that will create the desired property on the material. Thermomechanical treatments are also employed on raw steel to achieve even better properties and to improve steel's resistance to different demands. This book presents the latest processes, techniques, and methodologies used to create new types of steels and to improve the different properties of those steels already known. It also discusses new fabrication processes, the inclusion of alloying elements, and new heat treatments or thermomechanical routes to demonstrate how steel properties can be optimally designed and engineered.

Published in London, UK

IntechOpen

ISBN 978-1-83769-833-2
9 781837 698332